Universität Hamburg
DER FORSCHUNG | DER LEHRE | DER BILDUNG

FAKULTÄT
FÜR MATHEMATIK, INFORMATIK
UND NATURWISSENSCHAFTEN

Experimental Investigation on Non-Local Entanglement in Electron-Exchange Collisions

Dissertation

zur Erlangung des Doktorgrades
an der Fakultät für Mathematik,
Informatik und Naturwisschenschaften
Fachbereich Physik
der Universität Hamburg

Vorgelegt von:

Mehrdad Kheyrollahi Kouhanestani

Matrikelnummer: 7519722

Hamburg

June 2025

Gutachter der Dissertation:	Prof. Dr. Markus Drescher Dr. Phillipp Wessel-Staarmann
Zusammensetzung der Prüfungskommision:	Prof. Dr. Markus Drescher Dr. Philipp Wessels-Staarmann Prof. Dr. Markus Ilchen Dr. Michael Martins Prof. Dr. Michael Potthoff
Vorsitzende der Prüfungskommision:	Prof. Dr. Michael Potthoff
Datum der Disputation:	24.09.2025
Vorsitzender des Fach-Promotionsausschusses PHYSIK:	Prof. Dr. Wolfgang J. Parak
Leiter des Fachbereichs PHYSIK:	Prof. Dr. Markus Drescher
Dekan der Fakultät MIN:	Prof. Dr.-Ing. Norbert Ritter

Abstract

The main goal of this experiment is to investigate quantum entanglement between massive particles with the potential for transferring spin polarization via non-local quantum effects. This approach employs electron-exchange scattering with spin-1/2 targets to generate entanglement. By eliminating photon-mediated interactions, this experimental configuration enables direct examination of non-local quantum state transfer between massive particles, whether temporally immediate or subluminal, while providing fundamental insights into entangled quantum systems comprising two massive particles.

The experiment consists of two primary phases. Initially, elastic electron-exchange scattering between free, unpolarized electrons and unpolarized fermionic atoms (sodium) is experimentally achieved to create a tunable entanglement resource. After the collision, the electrons will scatter and calculations show that the maximum degree of entanglement between sodium atoms and electrons occurs when the energy of incoming electrons is 10 eV and they are scattered at 60 degrees angle.

Subsequently, after a well-defined delay period that allows electrons to travel away from the collision center, a nanosecond-pulse laser with circularly polarized light (σ^+) is used to excite the sodium atoms. This, in part, transfers the light's polarization to the entangled atoms. Due to quantum entanglement, these entangled atoms are then predicted to transmit their polarization (or a part of it) to the previously unpolarized, though entangled, electronic ensemble. The key element here is the transfer of polarization from the sodium atoms to the entangled free electrons, even when they are separated by meters. Finally, the spin polarization of the electron ensemble is detected using a Mott polarimeter, where a non-zero measurement would indicate non-local quantum mechanical effects.

Preliminary experimental results align partially with theoretical predictions, suggesting the potential validity of the proposed approach. However, further investigations are needed to fully confirm these findings and establish conclusive evidence of the observed quantum mechanical effects.

Zusammenfassung

Das Hauptziel dieses Experiments ist die Untersuchung der Quantenverschränkung zwischen massiven Teilchen mit dem Potenzial zur Übertragung der Spinpolarisation über nicht-lokale Quanteneffekte. Dieser Ansatz verwendet Elektronenaustauschstreuung mit Spin-1/2-Targets zur Erzeugung von Verschränkung. Durch die Eliminierung photonenvermittelter Wechselwirkungen ermöglicht diese experimentelle Konfiguration die direkte Untersuchung der nicht-lokalen Quantenzustandsübertragung zwischen massereichen Teilchen, sei es zeitlich unmittelbar oder subluminal, während sie fundamentale Einblicke in verschränkte Quantensysteme aus zwei massereichen Teilchen liefert.

Das Experiment besteht aus zwei Hauptphasen. Zunächst wird die elastische Elektronenaustauschstreuung zwischen freien, unpolarisierten Elektronen und unpolarisierten fermionischen Atomen (Natrium) experimentell durchgeführt, um eine abstimmbare Verschränkungsressource zu erzeugen. Während der Kollision werden die Elektronen gestreut und Berechnungen zeigen, dass der maximale Grad der Verschränkung zwischen Natriumatomen und Elektronen auftritt, wenn die Energie der einlaufenden Elektronen 10 eV beträgt und sie unter einem Winkel von 60 Grad gestreut werden.

Anschließend wird nach einer genau definierten Verzögerungszeit, die es den Elektronen ermöglicht, sich vom Kollisionszentrum zu entfernen, ein Nanosekundenpulslaser mit zirkular polarisiertem Licht (σ^+) verwendet, um die Natriumatome anzuregen. Dies überträgt teilweise die Polarisation des Lichts auf die verschränkten Atome. Aufgrund der Quantenverschränkung wird vorhergesagt, dass diese verschränkten Atome ihre Polarisation (oder einen Teil davon) auf das zuvor unpolarisierte, jedoch verschränkte Elektronenensemble übertragen. Das Schlüsselelement hierbei ist die Übertragung der Polarisation von den Natriumatomen auf die verschränkten freien Elektronen, selbst wenn sie durch Meter voneinander getrennt sind. Schließlich wird die Spinpolarisation des Elektronenensembles mit einem Mott-Polarimeter erfasst, wobei eine von Null verschiedene Messung auf nicht-lokale quantenmechanische Effekte hinweisen würde.

Vorläufige experimentelle Ergebnisse stimmen teilweise mit den theoretischen Vorhersagen überein, was auf die potenzielle Gültigkeit des vorgeschlagenen Ansatzes

hindeutet. Allerdings sind weitere Untersuchungen und Verfeinerungen erforderlich, um diese Erkenntnisse vollständig zu bestätigen und schlüssige Beweise für die beobachteten quantenmechanischen Effekte zu erbringen.

Contents

List of Tables

List of Figures

1. Introduction

Quantum entanglement is a fascinating phenomenon in quantum mechanics, where two or more particles become correlated in such a way that even at great distances, the state of one particle cannot be described independently of the state of the other particles. So, observations of one of the particles can automatically provide information about the other entangled particles and any action to one of these particles will invariably impact the others in the entangled system.

At the beginning of the 20th century, physicists realized the limitations of classical mechanics in explaining the behavior of atoms and subatomic particles, so they developed the quantum theory. However, Einstein was never able to fully accept this new theory because of its probabilistic nature and the claim that certain details of an atom's behavior could not be precisely predicted. In 1935, Albert Einstein, Boris Podolsky, and Nathan Rosen published a paper to challenge the completeness of quantum mechanics [1]. They used a thought experiment to highlight what they saw as a puzzling aspect of quantum mechanics (known as the EPR paradox): the idea that particles could be "entangled" in such a way that measuring one particle's property could instantaneously influence the corresponding property of another one, even if they were far apart. They considered such behavior impossible, as it violated the local realism view of causality (Einstein referred to it as "spooky action at a distance"). As quantum mechanics could not meet their requirements for realism, locality, and completeness, they argued that the accepted formulation of quantum mechanics must be incomplete and the theory did not account for "hidden variables" that would determine outcomes.

In response to the EPR paradox, the physicist John Bell proposed a theory in the 1960s, which would later become known as Bell's theorem. Bell's work attempted to offer

a way to experimentally test the validity of quantum entanglement and the existence of hidden variables. Bell's theorem introduced the concept of Bell inequalities, mathematical expressions that, if violated, would imply that quantum entanglement could not be explained by local hidden variable theories. Essentially, these inequalities provided a way to experimentally assess whether the effects of quantum entanglement could be attributed to local hidden variables, as Einstein had proposed.

The first and most important concept to remember about Bell's inequality is that it is not a result of quantum mechanics and does not make any claims about quantum mechanics. Instead, this inequality is a result of applying argumentation based on fundamental assumptions of locality and realism. Locality means that events in spacelike-separated regions are not causally related and do not influence each other. It is also accepted that even if all random variables that characterize our physical system (independent of particle properties and measurement settings) were known, the outcome of an experiment is still random and uncertain.

The question Bell raises is whether, in a world with this property, what kinds of correlations are possible and what properties do they have? He shows that in such a world, correlations, no matter how strong or weak they may be, always have a constraint expressed by a simple inequality. When this inequality is violated in experiments, it implies that nature does not behave locally. Bell's theorem not only introduced a new perspective on quantum entanglement but also established the groundwork for experimental tests to challenge the classical concepts of realism and locality. It offered a clear method to determine whether the behavior of entangled particles truly defied classical intuitions.

Bell's investigation generated an ongoing discussion about the fundamentals of quantum mechanics. But it was Aspect et al. who first performed the most convincing early test of the violation of the Bell inequalities [2, 3]. After that, numerous experiments were conducted [4, 5], and ultimately, Alain Aspect, John F. Clauser, and Anton Zeilinger received the Nobel Prize in physics in recognition of their experiments

involving entangled photons. The experiments showed that entangled particle correlations violated Bell's inequalities, providing strong evidence for the non-classical nature of quantum entanglement. This challenged the concept of hidden variables and the classical explanation for entangled particle behavior.

While most studies utilized photons for testing local realism, in 2016 Blum and Lohmann [6] proposed a supplementary method to investigate the spin-spin correlations that are created in elastic collisions between initially unpolarized electrons and hydrogen-like atoms. The main aim of this thesis is to experimentally explore their proposal. In chapter 2, the theoretical background of the experiment is presented. In chapter 3, all the necessary simulations and designed parts for the experimental setup are provided, while in chapter 4 each part of the experimental setup is explained, and finally in chapter 5 all results are reported, and discussed.

2. Fundamental Concepts

2.1 Teleportation via Elastic Electron-Exchange Collisions

Quantum teleportation requires an entangled EPR pair, which we generate using the approach presented by Blum and Lohman [6, 7]. This entanglement is generated during an elastic electron-exchange collision. In this collision, unpolarized electrons and unpolarized atoms are elastically scattered and by choosing suitable scattering angles and energies their spins become entangled [6]. Also, by manipulating these scattering parameters, the full range of spin–spin correlations can be generated. Consequently, the resulting spin system serves as a tunable EPR resource [7]. Then a circularly polarized photon is used to excite the atom and according to theory its polarization state is non-locally teleported onto the first electron, which remains unpolarized after the first scattering [8]. In the next subsections the theoretical background to understand this approach is presented.

2.1.1 Entanglement in Electron-Exchange Collisions

An important part of this experiment is preparing an entangled state that is generated from the spin-spin correlations between unpolarized electrons and unpolarized atoms (sodium), through the elastic electron-exchange scattering. To describe this elastic scattering, we assume that all spin-dependent forces can be neglected and only electron exchange is considered.

Before the collision, the density matrix describing the initial unpolarized state of the

electrons and atoms is given by

$$\rho_{in} = \frac{1}{4} \sum_{m_1 m_2} |m_1 m_2\rangle \langle m_1 m_2|, \tag{2.1}$$

where m_1 and m_2 denote the spin components of the electrons and atoms, respectively. The density matrix of the final state after the scattering, is given by [7]

$$\rho = T \rho_{in} T^{\dagger}. \tag{2.2}$$

Here, T represents the transition operator. By denoting M_i and m_i as spin component in the final and initial states respectively, and by assuming that the scattering angle and energy remain constant, we can derive matrix elements as

$$\langle M_1' M_2'| \rho |M_1 M_2\rangle = \frac{1}{4} \sum_{m_1 m_2} \langle M_1' M_2'| T |m_1 m_2\rangle \times \langle m_1 m_2| T^{\dagger} |M_1 M_2\rangle . \tag{2.3}$$

By using Clebsch-Gordan coefficients, we can couple the total spin S and its component M_s in the T -matrix elements as

$$\langle M_1 M_2| T |m_1 m_2\rangle = \sum_{SM_s} (1/2M_1, 1/2M_2|SM_s) \times (1/2m_1, 1/2m_2|SM_s) \langle SM_s| T |SM_s\rangle . \tag{2.4}$$

By introducing $f^{(S)}$ as triplet ($S = 1$) and singlet ($S = 0$) scattering amplitudes respectively as

$$\langle SM_s| T |SM_s\rangle = f^{(S)}, \tag{2.5}$$

we can show that

$$\langle M_1' M_2'| \rho |M_1 M_2\rangle = \frac{1}{4} \sum_{SM_s} (1/2M_1', 1/2M_2'|SM_s)(1/2M_1, 1/2M_2|SM_s)|f^{(S)}|^2. \tag{2.6}$$

It's useful to represent the density matrix ρ in its matrix form, which by substituting

specific numerical values for the Clebsch-Gordan coefficients into Eq. (2.6), we can show [7]

$$\rho = \frac{1}{8\sigma}\begin{pmatrix} 2|f^{(1)}|^2 & 0 & 0 & 0 \\ 0 & |f^{(1)}|^2+|f^{(0)}|^2 & |f^{(1)}|^2-|f^{(0)}|^2 & 0 \\ 0 & |f^{(1)}|^2-|f^{(0)}|^2 & |f^{(1)}|^2+|f^{(0)}|^2 & 0 \\ 0 & 0 & 0 & 2|f^{(1)}|^2 \end{pmatrix}. \tag{2.7}$$

In this equation, ρ is normalized by the differential cross section σ

$$\sigma = \frac{1}{4}(3|f^{(1)}|^2+|f^{(0)}|^2), \tag{2.8}$$

and $tr\rho = 1$.

Alternatively, we can fully describe the spin density matrix in Eq. (2.7) in terms of the two individually measured spin polarization vectors $\mathbf{P}^{(1)}$ and $\mathbf{P}^{(2)}$ for particles 1 and 2 respectively [7], where

$$P_i^{(1)} = \mathrm{tr}\rho(\sigma_i \times \mathbb{I}) \qquad \text{and} \qquad P_i^{(2)} = \mathrm{tr}\rho(\mathbb{I} \times \sigma_i), \tag{2.9}$$

where σ_i denotes the Pauli matrices, $i = x, y, z$, $\mathbb{I}$ is the two-dimensional unit matrix, and the cross denotes the direct product. The nine direct product components $P_i^{(1)} \times P_j^{(2)}$ of the spin-spin correlation tensor defined by [9]

$$P_i^{(1)} \times P_j^{(2)} = tr\rho(\sigma_i \times \sigma_j). \tag{2.10}$$

By substituting Eq. (2.7) and Pauli matrices into Eq. (2.10), we can compute the parameters of the spin-spin correlation tensor, which shows that the only nonvanishing spin correlation parameters are

$$P = P_i^{(1)} \times P_i^{(2)} = \frac{|f^{(1)}|^2-|f^{(0)}|^2}{3|f^{(1)}|^2+|f^{(0)}|^2}, \qquad i = x, y, z. \tag{2.11}$$

Here, we introduced the spin correlation parameter $P = P(\Theta, E)$, which is a function of scattering angle and energy in the scattering process [7]. Therefore, by using Eqs. (2.8) and (2.11), we can express the density matrix as a function of this spin correlation parameter

$$\rho = \frac{1}{4}\begin{pmatrix} 1+P & 0 & 0 & 0 \\ 0 & 1-P & 2P & 0 \\ 0 & 2P & 1-P & 0 \\ 0 & 0 & 0 & 1+P \end{pmatrix}. \tag{2.12}$$

In general, P is restricted to the range of $[-1, 1]$, but Eq. (2.11) demonstrates that in our specific case, we have further restrictions, given by

$$-1 \leq P \leq \frac{1}{3}. \tag{2.13}$$

Since the density matrix ρ is just related to one parameter P, it is necessary to determine the conditions under which the mixed spin state would be separable, entangled, or a combination of both. Peres [10] and Horodecki et al. [11] derived a convenient criterion which, in the case of a 4×4 density matrix, provides a necessary and sufficient condition for separability. According to their criterion, a given density matrix ρ describes a separable state if all eigenvalues of its partial transpose density matrix ρ^{PT} are positive. Conversely, ρ describes an entangled system if at least one eigenvalue of ρ^{PT} is negative [7]. The partial transpose density matrix is defined as

$$\langle M'm'|\,\rho^{PT}\,|Mm\rangle = \langle Mm'|\,\rho\,|M'm\rangle\,. \tag{2.14}$$

By applying this to the density matrix Eq. (2.12) we obtain

$$\rho^{PT} = \frac{1}{4}\begin{pmatrix} 1+P & 0 & 0 & 2P \\ 0 & 1-P & 0 & 0 \\ 0 & 0 & 1-P & 0 \\ 2P & 0 & 0 & 1+P \end{pmatrix}. \tag{2.15}$$

The eigenvalues of the matrix ρ^{PT} are

$$\lambda_{1,2,3} = \frac{1}{4}(1-P) \qquad \text{and} \qquad \lambda_4 = \frac{1}{4}(1+3P). \tag{2.16}$$

Eq. (2.16) shows that for values of P within the range of $-\frac{1}{3} \leq P \leq \frac{1}{3}$, all eigenvalues are positive. So, the scattering matrix ρ is separable in this region. For the range $-1 \leq P < -\frac{1}{3}$, λ_4 is negative and the density matrix ρ describes an entangled system. The system is maximally entangled when $P = -1$.

B. Lohmann, K. Blum, and B. Langer [6] additionally demonstrated that within the range of $-\sqrt{\frac{1}{2}} \leq P < -\frac{1}{3}$, the Bell inequality remains unviolated since in this region the spin correlation is not sufficiently strong and quantum correlations can theoretically be simulated within local theories. However, the violation of the Bell inequality occurs for $-1 \leq P < -\sqrt{\frac{1}{2}}$. This implies that a value of $P < -\sqrt{\frac{1}{2}}$ is essential to exclude the possibility of entanglement created by classical means [7].

As mentioned earlier, P is a function of scattering angle and energy, and variation of scattering angle and/or energy changes the nature of the combined spin system from maximally entangled to completely mixed. Therefore, the degree of entanglement can be adjusted in advance by choosing an appropriate pair of E and Θ. Additionally, Eq. (2.11) demonstrates that when $P = -1$ the triplet scattering amplitude, $f^{(1)}$, is zero and the Pauli-principle requires that an atom and an electron must be found in the maximally

entangled singlet state, given by

$$|00\rangle = \frac{1}{\sqrt{2}}(|\uparrow\rangle_A |\downarrow\rangle_e - |\downarrow\rangle_A |\uparrow\rangle_e), \tag{2.17}$$

where $|\uparrow\rangle$ and $|\downarrow\rangle$ represent spin up and down, respectively, relative to the laboratory z_e-axis, with indices A and e indicating the atom and the electron, respectively.

For a better understanding of the relationship between collision dynamics and entanglement properties, it would be preferable to analyze published numerical and experimental data for P. However, performing a spin-selective coincidence experiment is difficult to perform. Therefore, it is better to obtain the correlation parameter P from the results of a different type of experiment, where there is already a large amount of experimental and numerical data available. For instance, consider the case where electrons and atoms are initially polarized. Then, the spin asymmetry A_{ex} can be measured, which in terms of the scattering amplitudes $f^{(0)}$ and $f^{(1)}$, is defined as [12]

$$A_{ex} = \frac{|f^{(0)}|^2 - |f^{(1)}|^2}{3|f^{(1)}|^2 + |f^{(0)}|^2}. \tag{2.18}$$

By comparing Eq. (2.11) and Eq. (2.18), we find

$$P(\Theta, E) = -A_{ex}(\Theta, E). \tag{2.19}$$

Thus, by using published spin asymmetry data for A_{ex} from these types of experiments and considering Eq. (2.19), we can estimate the spin correlation parameter P for our experimental setup with initially unpolarized particles.

Several research groups investigated spin-dependent elastic $e-H$ scattering in different energy regions ([13, 14, 15, 16, 17]) and the data indicate that entanglement is primarily observed at low energies, such as E = 0.14, 0.54, and 1.22 eV, while the Bell correlated region is almost inaccessible [7].

The NIST group performed measurements on spin-dependent elastic $e-Na$ scattering, and they showed that the correlation parameter P can vary over the entire range from $P=1/3$ (full separability) to $P=-1$ (full entanglement). This indicates that any degree of entanglement or even Bell-violating correlations can be achieved in elastic $e-Na$ scattering experiments ([12, 18, 19, 20]). For instance, at $E=4.1$ eV, entanglement was detected between approximately 80° and 105°, with $P\approx-0.87$, indicating a Bell correlated region. At $E=10$ eV, P rapidly decreased around $\Theta=60°$, approaching $P=-1$, which shows that we can achieve formation of the maximally entangled singlet state. Similar behavior was observed at $E=12.1$ eV, with P revealing a sharp minimum near $\Theta=53°$ and both energy values exhibited excellent agreement with theoretical calculations. Additionally, NIST data indicated that for energies exceeding 20 eV practically no entanglement can be produced. Fig. 2.1 provides a visual representation of both experimental and theoretical data for correlation parameter P against the scattering angle, Θ, at different scattering energies for spin-dependent elastic $e-Na$ scattering. The agreement between theoretical predictions and experimental data is evident. Notably, at $E=10$ eV, the figure indicates a point at Θ, where the system achieves full entanglement.

Also there are some experimental and calculational data on elastic $e-Li$ scattering and they exhibit similar behavior to those observed in elastic $e-Na$ scattering experiments [25, 26]. For instance at $\Theta=107.5°$, the correlation parameter decreases rapidly to $P=-1$ for low energies $E\approx4$ eV.

Therefore, by taking into account both experimental and computational data for different types of material and considering the practical feasibility of performing the experiment, it has been decided to focus on sodium atoms with an energy of 10 eV and a scattering angle of 60°.

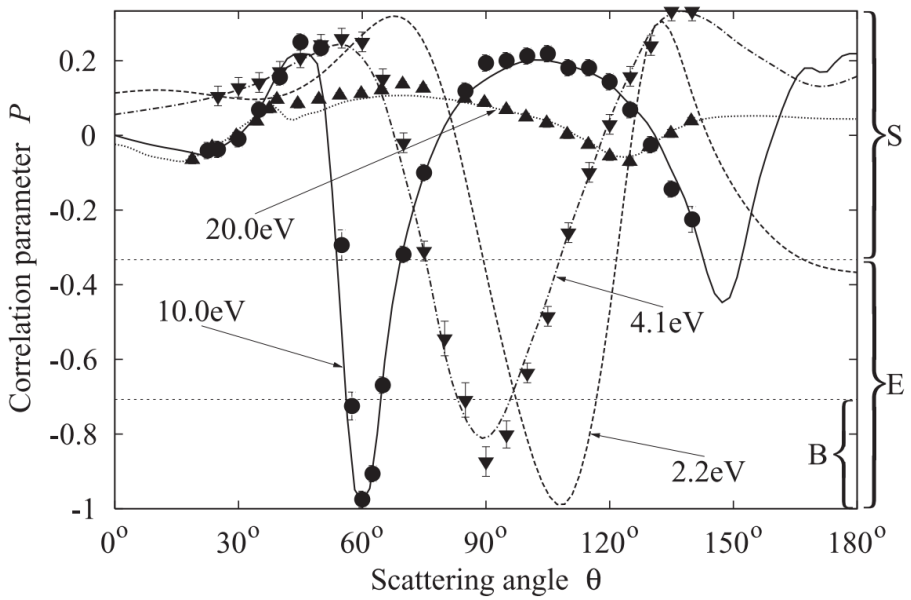

Figure 2.1: The correlation parameter, P, for sodium is plotted against the scattering angle, Θ, for various scattering energies. Experimental data provided by the NIST group are represented for energies of 4.1 eV (▼) from McClelland et al. [18, 20], 10 eV (●), and 20 eV (▲) from Kelley et al. [21]. Additionally, numerical data are included: 2.2 eV (CC) sourced from Moores and Norcross [22], and for energies of 4.1, 10, and 20 eV (CCC) obtained from Bray [23, 24]. Horizontal lines on the graph demarcate the separable (S), entangled (E), and Bell correlated (B) regions [7]. Taken from Lohmann et al. [6].

2.1.2 Polarization Transfer in Photon-Atom-Electron Systems

In order to introduce the method of polarization transfer in photon-atom-electron systems, we follow an idea that has been developed by Lohmann et al.[27]. As demonstrated in the previous section by selecting appropriate parameters for Θ and E, the atom and electron will be in the maximally entangled singlet state $|00\rangle$. Afterwards, they are distributed between two observers Alice and Bob, where Alice receives the atoms and Bob receives the electrons. Additionally, Alice has a source of photons with a definite polarization. For simplicity, we assume that Alice's photons are 100% right-handed (σ^+) circularly polarized with respect to the photon beam axis. We show below that by photo-excitation of Alice's atoms from the $Na(3s)^2S_{1/2}$ ground state to the $Na(3p)^2P_{1/2}$ fine structure state (in the case of sodium this corresponds to the Fraunhofer D_1-line at $\lambda = 589.6\,nm$)

by using a fine-tuned laser we are able to transfer Alice's photon state to Bob via non-local photon-to-electron signaling.

To demonstrate this mathematically, we introduce the photon helicity λ and choose the quantization axis in the helicity system. Since Alice's photons are right-handed circularly polarized, they are represented by the state $|\lambda = 1\rangle$. Furthermore, by considering this important property of the singlet state, that remains unchanged under any rotation of the coordinate system, its expression in the helicity basis of the photon state can immediately be given by

$$|00\rangle = \frac{1}{\sqrt{2}}(|\uparrow_\lambda\rangle_A |\downarrow_\lambda\rangle_e - |\downarrow_\lambda\rangle_A |\uparrow_\lambda\rangle_e). \tag{2.20}$$

Thus, before photo-excitation the initial three-particle state $|\psi_{in}\rangle$ is given by the direct photon-atom-electron product state

$$|\psi_{in}\rangle = |\lambda = 1\rangle \otimes |00\rangle = \frac{1}{\sqrt{2}}(|\lambda_{h\nu}\rangle |\uparrow_\lambda\rangle_A |\downarrow_\lambda\rangle_e - |\lambda_{h\nu}\rangle |\downarrow_\lambda\rangle_A |\uparrow_\lambda\rangle_e). \tag{2.21}$$

Now at time t_1 Alice excites her atom up to the $Na(3p)^2P_{1/2}$ state, where $t_1 > t_0$ (with t_0 denoting the time of the initial electron-atom scattering event). This process is temporally separated from the initial electron-atom scattering event. It is crucial to ensure that Bob cannot directly access the photo-excitation process or its results. Under these conditions, the photo-excitation process to the $Na(3p)^2P_{1/2}$ state is accurately described by the dipole approximation, denoted as D_{II}. By representing the excited Na fine structure states as $|Jm_J\rangle$, where J is the total angular momentum and m_J refers to the magnetic quantum number, the photo-excitation process can be described by the following transformation

$$|\lambda\rangle |m_{S_A}, m_{S_e}\rangle \xrightarrow{D_{II}} d^{(J)} |Jm_J\rangle |m_{S_e}\rangle , \tag{2.22}$$

where $m_{S_A} = \pm 1/2$ is the magnetic spin quantum number of the $Na(3s)^2S_{1/2}$ ground state,

$m_{S_e} = \pm 1/2$ refers to the electron spin of the scattered electron, and $d^{(J)}$ is the reduced dipole transition matrix element, which is independent of m_J. On the other hand, photo-excitation selection rules require the general restriction $\lambda + m_{S_A} = m_J$. In our case, Alice is using circularly polarized σ^+ light, which yields $\lambda = 1$. Consequently, photo-excitation can only occur from the magnetic $m_{S_A} = -1/2$ ground state up to the $m_J = 1/2$ excited state (Fig. 2.2 shows the photo-excitation process by considering the selection rule). So, by substituting Eq. (2.22) in Eq. (2.21) and considering the selection rule, we obtain the final state of the system after photo-excitation as

$$|\psi_{in}\rangle = |\lambda\rangle\,|00\rangle \xrightarrow{D_{II}} |\psi_{out}\rangle = \frac{1}{\sqrt{2}} d^{(J)} \left(|J, \underbrace{\lambda + 1/2}_{m_J = 3/2}\rangle\,|{\downarrow_\lambda}\rangle_e - |J, \underbrace{\lambda - 1/2}_{m_J = 1/2}\rangle\,|{\uparrow_\lambda}\rangle_e \right). \tag{2.23}$$

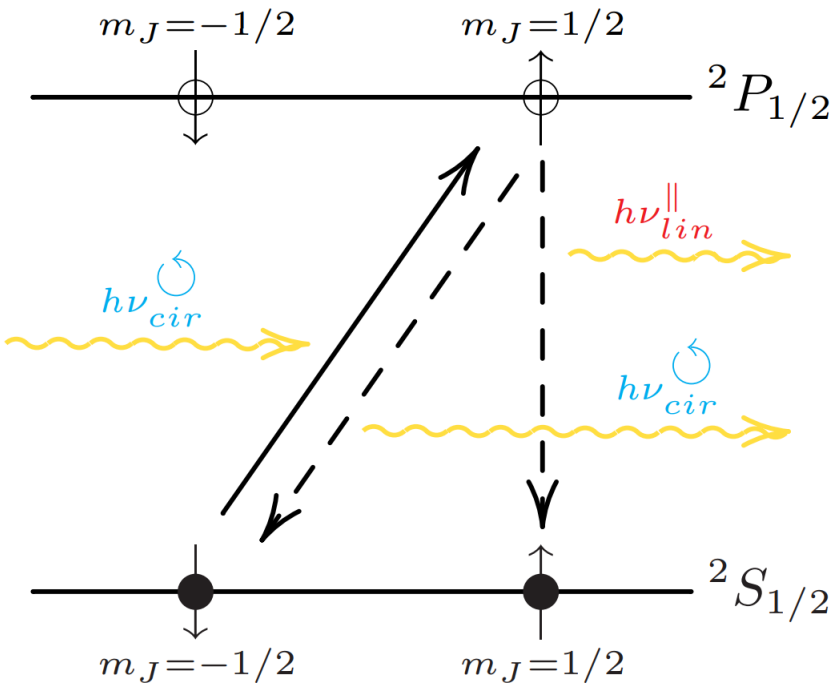

Figure 2.2: Sodium photo-excitation to the $Na(3s)^2P_{1/2}$ state by right circularly polarized light. Taken from Lohmann et al.[27].

On the other hand, since Alice's laser source is fine-tuned precisely to the Fraunhofer D_1-line, we can selectively excite the $J = \frac{1}{2}$ fine structure state. As a result, the first term

in Eq. (2.23) cancels due to the restriction $J \geq |m_J|$ and we can simplify this equation as

$$|\psi_{in}\rangle \xrightarrow{D_{II}} |\psi_{out}\rangle = -\frac{1}{\sqrt{2}} d^{(1/2)} \, |1/2, 1/2\rangle \otimes |\uparrow_\lambda\rangle_e \, . \tag{2.24}$$

Eq. (2.24) shows that after photo-excitation the electron spin is in the pure state $|\uparrow_\lambda\rangle \, e$. Thus, the electrons are longitudinally spin-polarized with respect to the photon beam axis $z_{h\nu}$, which is used as the quantization axis. After re-normalization, we obtain

$$|\psi_{out}\rangle = |1/2, 1/2\rangle \otimes |\uparrow_\lambda\rangle_e = |1/2, 1/2\rangle \otimes (\alpha \, |\uparrow\rangle_e + \beta \, |\downarrow\rangle_e), \tag{2.25}$$

where the last term in Eq. (2.25) has been rotated back and now refers to the laboratory z_e-axis (electron-analyzer/detector axis). Fig. 2.3 illustrates the geometry of the experiment and various angles that are indicated.

By parametrizing the amplitudes in Eq. (2.25) as $\alpha = \cos\vartheta/2$ and $\beta = \exp^{i\phi} \sin\vartheta/2$, where ϑ denotes the polar angle between the quantization axis $z_{h\nu}$ of the photon beam and the direction z_e of electron emission, it is always possible to choose polar angle ϑ and azimuthal angle ϕ accordingly in order to observe the maximal electron spin polarization into a certain direction. (Note that $\vartheta \neq \theta_1$). In our case, by choosing $\vartheta = \pi/2$ and $\phi = 0$, the electron will be in the pure spin state $|\psi\rangle_e = |\uparrow x_e\rangle = \frac{1}{\sqrt{2}}|(|\uparrow z_e\rangle + |\downarrow z_e\rangle)$ perpendicular to the spin analyzer/detector z_e-axis of the Mott polarimeter, which shows that the electron spin is oriented along the x_e-axis.

Thus, circular polarization ($\lambda = 1$) of the exciting photon is transferred to the magnetic $^2P_{1/2}$, $m_J = 1/2$ fine structure state and fully polarizing the initially unpolarized atomic state. Since the atom is entangled with the electron during the elastic scattering, which remains unpolarized after the initial scattering, this entanglement forces the electron into a definite spin state $|\psi\rangle_e = \alpha \, |\uparrow\rangle_e + \beta \, |\downarrow\rangle_e$. It is important to note that there is no direct interaction between Alice's photon and Bob's electron. The teleportation of circular polarization of Alice's photon onto Bob's electron takes place after the first scattering while

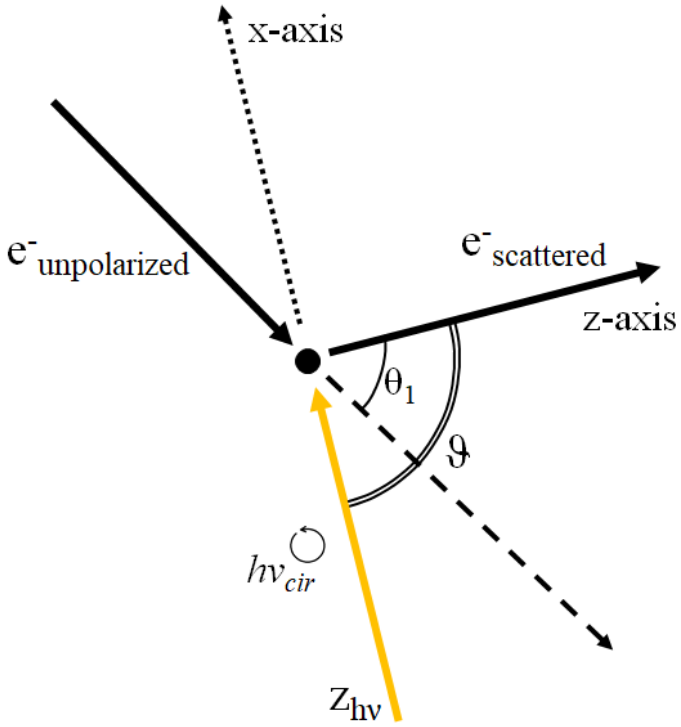

Figure 2.3: Geometry of the experiment. Electron-atom scattering occurs at an angle θ_1 relative to the direction of the scattered electron z_e, which serves as the quantization axis. For the sodium case, $\theta_1 = 60°$. The angle between z_e and the helicity system of the photon beam axis ($z_{h\nu}$) is denoted as ϑ. In the discussed geometry, we choose polar and azimuthal angles as $\vartheta = 90°$ and $\phi = 0°$, respectively. Using circularly polarized light results in the spin polarization of the scattered electron being perpendicular to z_e. Rotating the photon beam axis $z_{h\nu}$ around z_e by the azimuthal angle ϕ consequently rotates the electron's spin polarization. Adapted from Lohmann et al.[27].

the electron has already left the area of interaction. The circular polarization of the photon is instantaneously transferred to Bob's electron once photo-excitation to the $m_J = 1/2$ fine structure level of the $Na(3p)^2P_{1/2}$ state occurs. Eventually, the electron spin is detected using Mott polarimeter techniques at time $t_3 \geq t_2$, where t_2 marks the end of photo-excitation and corresponds to the end of the laser pulse. Note that t_3 can be, in principle, identical to t_2, which might be of advantage for a time dependent detection analysis in order to investigate the instantaneous signalling via non-local photon-to-electron signaling in more detail.

2.2 Mott Polarimeter

In order to assess the entanglement between electrons and sodium atoms, we need to measure the spin polarization of the electron beam. However, the utilization of traditional spin filters, such as the Stern-Gerlach magnet, is not possible for this free-electron beam because of the Lorentz force which does not apply to neutral atoms in the Stern-Gerlach magnet. This, combined with the uncertainty principle, prevents the separation of spin-up and spin-down electrons [28]. So, Nevill Mott [29] proposed a method for measuring the spin polarization of electrons by utilizing elastic scattering of electrons from heavy atomic nuclei. In this method, when fast electrons are scattered by a heavy nucleus, there is an asymmetry in the back-scattering, which depends on the spin polarization of the incoming electron beam. Fig. 2.4 shows the schematic of a Mott polarimeter, where, depending on the spin polarization, statistically more electrons are measured on one detector rather than the other.

The physical basis of the Mott scattering is based on the spin-orbit coupling of high energetic electrons in the Coulomb field of a heavy atomic nucleus. An electron moving with speed v in electric field E of a heavy nucleus sees a magnetic field B in its rest frame that is given by

$$\vec{\mathbf{B}} = -\frac{1}{c}\vec{\mathbf{v}} \times \vec{\mathbf{E}}. \tag{2.26}$$

By considering $\vec{\mathbf{r}}$ as the nucleus-electron separation, $\vec{\mathbf{E}} = (Ze/r^3)\vec{\mathbf{r}}$, and $\vec{\mathbf{B}}$ can written as

$$\vec{\mathbf{B}} = \frac{Ze}{cr^3}\vec{\mathbf{r}} \times \vec{\mathbf{E}} = \frac{Ze}{mcr^3}\vec{\mathbf{L}}. \tag{2.27}$$

When this magnetic field interacts with the electron's magnetic moment $\vec{\boldsymbol{\mu}}_s$, it introduces the term $V_{so} = -\vec{\boldsymbol{\mu}}_s \cdot \vec{\mathbf{B}}$ into the scattering potential. Since $\vec{\boldsymbol{\mu}}_s = -(ge/2mc)\vec{\mathbf{S}}$ and by using

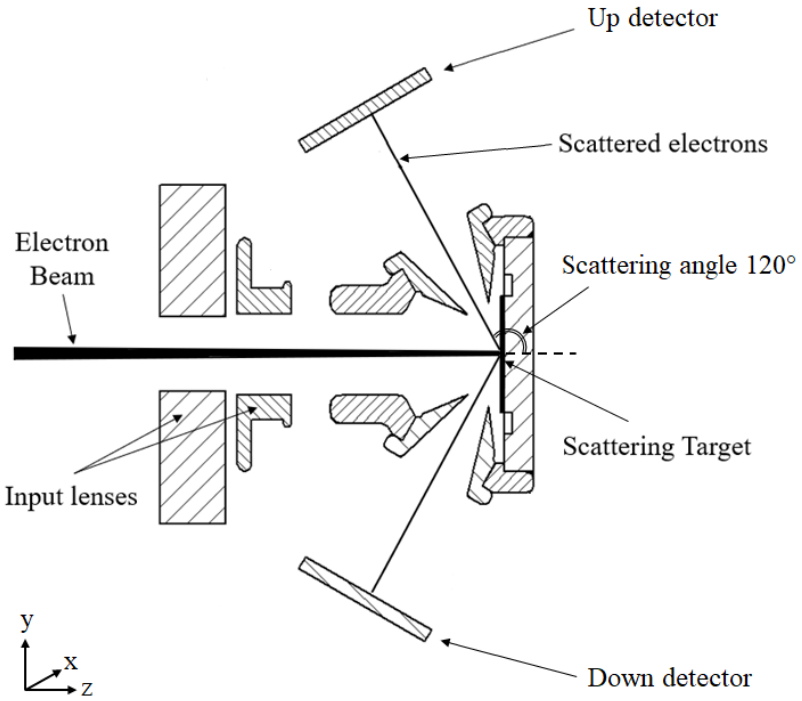

Figure 2.4: Schematic diagram of the Mott polarimeter. The accelerated electrons are elastically scattered at the gold target and detected by the double microchannelplates.

Eq. (2.27) we can show that the spin-orbit potential is

$$V_{so} = \frac{Ze^2}{2m^2c^2r^3}\vec{\mathbf{L}}\cdot\vec{\mathbf{S}}. \tag{2.28}$$

So, the total scattering potential is

$$V_{total} = \left(\frac{1}{4\pi\epsilon_0}\right)\frac{Ze^2}{r} + \frac{Ze^2}{2m^2c^2r^3}\vec{\mathbf{L}}\cdot\vec{\mathbf{S}}. \tag{2.29}$$

Since $\vec{\mathbf{L}}$ is always perpendicular to the scattering plane, based on whether the spin direction is up or down, the interaction term V_{so} either increases or decreases the overall interaction potential. This causes an asymmetry in up/down scattering angles during the scattering process. In other words, the spin-orbit term in the scattering potential introduces a spin

dependence in the scattering cross section as [30]

$$\frac{d\sigma}{d\Omega}(\theta,\phi) \equiv \sigma(\theta,\phi) = I(\theta)\left(1 + S(\theta)\vec{\mathbf{P}}\cdot\hat{\mathbf{n}}\right), \tag{2.30}$$

where $I(\theta)$ corresponds to the Rutherford scattering cross section. $\vec{\mathbf{P}}$ is the spin polarization of the incident electron beam. The unit vector $\hat{\mathbf{n}}$ is the normal vector to the scattering plane and is defined as: $\hat{\mathbf{n}} \equiv \frac{\vec{K}\times\vec{K}'}{|\vec{K}\times\vec{K}'|}$, where $\vec{K}$ and $\vec{K}'$ represent the wave vectors of incoming and deflected electrons, respectively. The parameter $S(\theta)$ is known as Sherman function which describes the degree of asymmetry in the scattering of a polarized beam and is usually determined experimentally. Realistic values for this type of detector range between 0.15 to 0.4.

Eq. (2.30) is the basic formula for measuring electron spin polarization using Mott scattering. It shows we can calculate the asymmetry by comparing the differences in counting rates on the up and down sides of the scattering plane for a certain solid angle. Since the scalar product remains invariant under coordinate transformations, this formula remains unaffected by the coordinate system selection. It is important to note that the scattering asymmetry is determined only by the component of the spin polarization vector perpendicular to the scattering plane and components parallel to the scattering plane have no effect. The asymmetry A is calculated as

$$A(\theta) = \frac{\frac{d\sigma}{d\Omega}(\phi=90) - \frac{d\sigma}{d\Omega}(\phi=270)}{\frac{d\sigma}{d\Omega}(\phi=90) + \frac{d\sigma}{d\Omega}(\phi=270)} = \frac{N_r - N_l}{N_r + N_l} = P(\theta)S(\theta), \tag{2.31}$$

where N_r and N_l are the number of electrons scattered to the up and down at an angle θ, respectively.

In reality, however, there are instrumental asymmetries in addition to the Mott asymmetries calculated in the theory. This is often caused by the different response probabilities of the detectors (such as MCP) and/or the incorrect positioning or alignment of the measuring apparatus, resulting in the electron ensemble not striking the target

perpendicularly. Unwanted magnetic or electric fields can also lead to the deflection of the electron ensemble or rotation of the spin vector. Factors such as inhomogeneity of the gold target and many others can also contribute to such asymmetries. According to [28], the instrumental asymmetry can be determined by inverting the spin polarization ($P \to -P$), i.e. by changing the spin polarization of the sodium atoms, which is related to the helicity of the photons during the measurement. In order to determine the device asymmetry, the counting rates of different spin polarizations are compared and evaluated as [28]

$$\rho = \sqrt{\frac{U_\uparrow U_\downarrow}{D_\uparrow D_\downarrow}}, \tag{2.32}$$

where $U_\uparrow$ and $D_\uparrow$ represent the count rates on the up and down detectors in case we use right circular light, and $U_\downarrow$ and $D_\downarrow$ represent the count rates for left circular light. Under ideal conditions, if there is no device asymmetry, we have $\rho = 1$. Any deviation from this is caused by the device asymmetry, which ideally should remain constant over time. If this changes between several measurements, this is an indication of an inaccurate measurement. So, by considering the instrumental asymmetry, the pure spin asymmetry can be determined as [31]

$$A = \frac{\sqrt{U_\uparrow D_\downarrow} - \sqrt{U_\downarrow D_\uparrow}}{\sqrt{U_\uparrow D_\downarrow} + \sqrt{U_\downarrow D_\uparrow}}. \tag{2.33}$$

Finally, the spin polarization of an incoming electron beam can be calculated by knowing the Sherman function of the device and measuring the asymmetry .

2.3 Collimated Atomic Beam

The process of generating an atomic beam occurs when a gas or vapor at higher pressure flows through a small opening into a region of lower pressure. Here, we focus on conditions where the kinetic theory of gases is applicable, specifically thermal beams, which exhibit a Maxwellian distribution of velocities among the atoms.

Early atomic beam experiments utilized a simple circular orifice with a diameter of a fraction of a millimeter. According to the kinetic theory of gases, the resulting beam from this orifice ideally exhibits a cosine distribution. This is because atoms traveling perpendicular to the orifice's plane are more likely to pass through than those approaching at near grazing incidence.

To continue the discussion, it is necessary to introduce the mean free path λ, which represents the average distance an atom travels between collisions, and it is given by [32]

$$\lambda = \frac{kT}{\sqrt{2}\pi p\sigma^2}, \tag{2.34}$$

where k is Boltzmann's constant, p the pressure [Pa], T the absolute temperature $[K]$, and σ the atomic diameter [m].

For an orifice, if the mean free path is equal to or greater than its diameter, the rate of atoms dN leaving the area element dA of the orifice, into a solid angle element $d\omega$ at an angle θ relative to the normal of A, with considering Maxwellian velocity distribution, can be given by

$$dN = I(\theta)d\omega = n_0\bar{v}dA\cos\theta\frac{d\omega}{4\pi}, \tag{2.35}$$

where $\bar{v}$ is the average velocity $\bar{v} = \sqrt{8kT/\pi m}$. So, the total number of atoms leaving the orifice per second is given by

$$N = n_0\bar{v}A/4. \tag{2.36}$$

From Eq. (2.35) and Eq. (2.36) the axial intensity when $\theta = 0$ is given by

$$I(0) = \frac{N}{\pi} \quad sr^{-1}s^{-1}. \tag{2.37}$$

Another important parameter in atomic beams is the number density of the beam at a

distance R from the orifice and is given by

$$\rho(R,\theta) = \frac{n_0 A \cos\theta}{4\pi R^2}, \tag{2.38}$$

which from Eq. (2.35) to Eq. (2.37) for $\theta = 0$ can be written as

$$\rho(R,0) = \frac{I(0)}{R^2 \bar{v}}. \tag{2.39}$$

Above equations demonstrate that the relationship between the axial beam intensity, detected by a sensor with a sensitive area of Δa at a distance R, and the total effusing intensity, is given by $\Delta a/\pi R^2$. This ratio is typically small, falling within the range of 10^{-6} to 10^{-8}. In cases, where reducing system contamination or preserving a rare material is essential, or when the pumping speed in the source chamber is restricted, employing a tube instead of an orifice results in a significant enhancement of this ratio. Also experimental findings indicated that a narrow tube generated a beam with a considerably narrower angular distribution than the cosine distribution observed with an orifice.

In order to calculate the number of atoms passing through the tube per second, it is crucial to determine the transmission probability W of the tube. This dimensionless factor depends only on the tube's geometry and its value is 1 for an ideal orifice. Through numerical calculations, its value is approximately given by [33]

$$W = 1 + \frac{2}{3}(1-2\alpha)(\beta - \sqrt{1+\beta^2}) + \frac{2}{3}(1+\alpha)\beta^{-2}(1-\sqrt{1+\beta^2}), \tag{2.40}$$

where

$$\alpha = \frac{1}{2} - \frac{1}{3\beta^2}\left(\frac{1-2\beta^3+(2\beta^2-1)(1+\beta^2)^{1/2}}{(1+\beta^2)^{1/2} - \beta^2 \sinh^{-1}\left(\frac{1}{\beta}\right)}\right) \qquad \text{and} \quad \beta = \frac{d}{l}, \tag{2.41}$$

where d is tube diameter and l is its length.

When the gas pressure is sufficiently low in a tube ($\lambda \gg l$), free molecular flow occurs

which is characterized only by wall collisions and flow properties are determined by the tube's geometry. In this case, some atoms pass straight through the tube without interacting with its walls, while others collide with different parts of the tube walls, potentially exiting the tube. Consequently, a near cusp-shaped atom beam distribution is achieved, which is a significant improvement in shape over that produced by an orifice. However, the axial intensity of the beam in these conditions is much lower than that formed by an orifice, and the tube needs to operate at a higher pressure. As the gas pressure increases, intermolecular collisions become comparable to molecule-wall collisions, leading to changes in the angular distribution and axial intensity. Various authors have extended the theory of flow through a tube to include collisions, and numerical evaluations confirm that as gas pressure increases from a point, where the mean free path equals the tube length, axial intensity initially rises linearly with pressure, while the beam halfwidth hardly increases. Consequently, atom collisions within the tube contribute to enhancing beam quality rather than degrading it. In the subsequent discussion, some of their results for axial intensity, throughput N, and halfwidth are presented.

It should be mentioned that the provided equations are suitable for tubes, where $\Gamma = l/d \geq 10$ or $\beta \leq 0.1$ and for input gas pressures $\lambda \geq d$. Also, to facilitate the practical use of these equations, tube diameters, d, are presented in micrometers, and tube lengths, l, in millimeters. Atomic diameters, σ, are expressed in picometers. Pressures, p are denoted in Pascals, and temperatures, T, in Kelvin. Halfwidths are measured in degrees, representing the full width at half the peak height.

In these specified conditions, the throughput N at all pressures and temperatures can be accurately expressed to three significant figures as [32]

$$N = \frac{2.76 \times 10^9 d^3 p}{l M^{1/2} T^{1/2}} \quad \text{atoms s}^{-1}, \tag{2.42}$$

where M is the atomic weight. Also, axial intensity $I(0)$ is given by

$$I(0) = \frac{4.60 \times 10^{13} d^2 p^{1/2} \mathrm{erf}\left(4.60 \times 10^{-2} \sigma l^{1/2} p^{1/2} / T^{1/2}\right)}{M^{1/2} l^{1/2} \sigma} \quad \text{atoms sr}^{-1}\text{s}^{-1}, \tag{2.43}$$

where

$$\mathrm{erf}(x) = \frac{2}{\pi^{1/2}} \int_0^x \exp(-x^2)\, dx. \tag{2.44}$$

And finally, the beam halfwidth H (degrees) is given by

$$H = \frac{9.62 \times 10^{-2} d/l}{\mathrm{erf}\left(\frac{76.4 T^{1/2}}{\sigma l^{1/2} p^{1/2}}\right)}. \tag{2.45}$$

Eq. (2.42), to Eq. (2.45) facilitate the comprehensive determination of the theoretical beam-forming properties for any tube, substance, and temperature through straightforward substitution and use of the error function.

2.4 Sodium Atom

Sodium plays a crucial role in our experiment due to its unique atomic properties. Sodium is an alkali metal that has 11 electrons and only one of them is in its outermost shell. Its only stable isotope is ^{23}Na. Some of its physical properties are given in Table 2.1.

Atomic Number	Z	11
Total Nucleons	$Z+N$	23
Relative Natural Abundance	$\eta(^{23}\mathrm{Na})$	100%
Atomic Mass	m	$22.9897692807(28)u$ $0.38175410023(12) \times 10^{-25}$ kg
Melting Point	T_m	97.80°C
Boiling Point	T_B	800°C
Nuclear Spin	I	3/2
Ionization Limit	E_I	5.13907696(25) eV

Table 2.1: Physical properties of sodium [34].

The vapor-pressure of sodium is given by [34]

$$\begin{aligned} \log_{10} P_V &= 2.881 + 5.298 - \frac{5603}{T} \qquad \text{(solid phase)} \\ \log_{10} P_V &= 2.881 + 4.704 - \frac{5377}{T} \qquad \text{(liquid phase)}, \end{aligned} \tag{2.46}$$

where T is the temperature in [K], and P_V is the vapor pressure in [torr], and its accuracy is better than $\pm 5\%$ from $298 - 700$K.

Also some optical properties of the sodium D_1 line that we need later in our experiment are given in Table 2.2.

Frequency	ω_0	2π . 508.333 195 8(13) THz
Transition Energy	$\hbar\omega_0$	2.102 297 176 5(54) eV
Wavelength (Vacuum)	λ	589.755 814 7(15) nm
Wave Number (Vacuum)	$k_L/2\pi$	16 956.170 250(43) cm^{-1}
Lifetime	τ	16.299(21) ns
Decay Rate/ Natural Line Width (FWHM)	Γ	$61.353(79) \times 10^6\ s^{-1}$ 2π . 9.765(13) MHz
Absorption oscillator strength	f	0.319 92(41)
Effective Far-Detuned Dipole Moment, Saturation Intensity, and Resonant Cross Section (π-polarized light)	$d_{\text{det,eff,}}$	1.438 91(93) ea_0 $1.219\ 96(79) \times 10^{-29}\ C.m$
	$I_{\text{sat(det,eff,)}}$	$1.219\ 96(79) \times 10^{-29}\ C.m$
	$\sigma_{0\text{(det,eff,)}}$	$5.535\ 598\ 649(28) \times 10^{-10}$

Table 2.2: Sodium D_1 ($3^2S_{1/2} \rightarrow 3^2P_{1/2}$) transition optical properties [34].

Finally, Fig. 2.5 depicts the hyperfine structure of the sodium atom for the D_1 transition. The energy difference between $F = 1$ and $F = 2$ states in the ground level is 1.77 GHz, while for the excited state $3^2P_{1/2}$, the energy difference is approximately 189 MHz. Given that our laser bandwidth is around 2 GHz, it is unlikely that we can resolve these hyperfine components during the photo-excitation process.

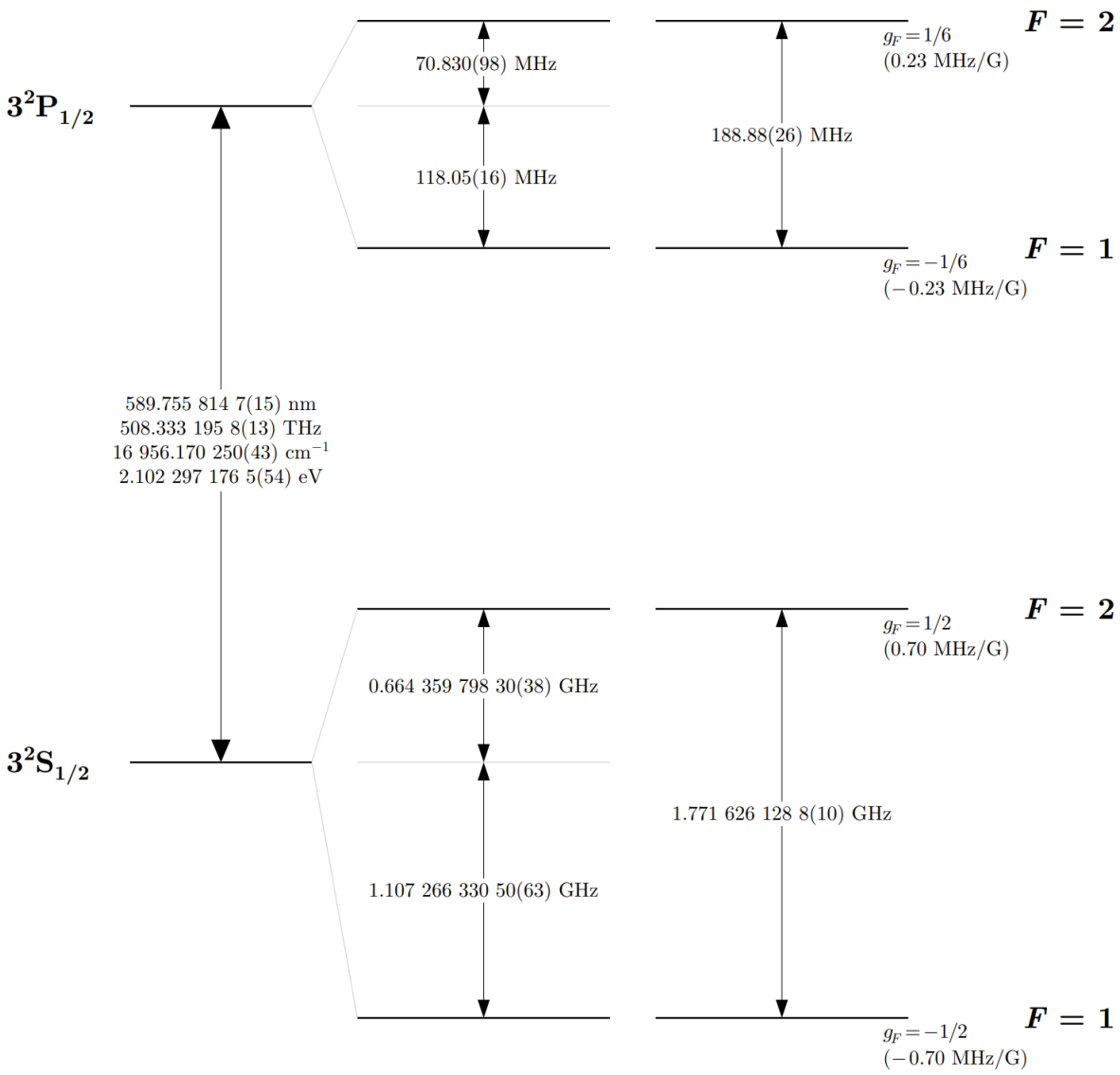

Figure 2.5: Hyperfine structure of the sodium D_1 transition, displaying frequency splittings among hyperfine energy levels [34].

3. Design and Simulations

3.1 Setup Overview

The experimental setup can be divided into several sections, each essential for the successful execution of the experiment. The schematic of the whole experiment is shown in Fig. 3.1.

In the initial phase, we employ a green pulsed laser (which is essential for precise timing and synchronization of the measurements). The laser has an energy per pulse of 1 mJ, a repetition rate of 10 kHz, a pulse duration of 50 ns, and linear polarization. The laser beam is split by using a beam splitter into two branches. The first branch with 20% of the laser's power is employed for the generation of ultraviolet (UV) light with a wavelength of 266 nm (equivalent to 4.66 eV per photon). Subsequently, this UV pulse is directed towards the electron gun, effectively back-illuminating a thin, silver (Ag) film. This interaction leads to the generation of electron pulses through the photoelectric effect.

The generated electrons are guided to the interaction region by electrostatic lenses inside the electron gun, providing them with a kinetic energy of precisely 10 eV. This specific energy value is crucial, as calculations by Lohmann et al. [27] demonstrate that deviating from 10 eV (either higher or lower) reduces the entanglement efficiency between electrons and sodium atoms. Simultaneously, an oven creates a beam of sodium atoms, establishing conditions for elastic scattering between the electrons and sodium atoms. According to the theoretical framework (Section 2.1.1), electrons scattered at 60° exhibit the highest degree of entanglement with the sodium atoms.

Subsequent to the scattering event, the scattered electrons pass through an electrostatic lens system and reach the Mott detector. The time it takes for electrons to travel from

the cathode of the electron gun to the Mott detector is approximately 300 ns.

Meanwhile, the remaining 80% of the green laser power is employed for pumping a dye laser generating light with a wavelength of 589.7 nm, corresponding to the D_1 line of the sodium atoms. The dye solution made from a mixture of Rhodamine 6G and Sulforhodamine B in ethanol and to extend the dye solution's lifetime, we added DABCO as a stabilizing agent. The emission spectrum of this dye mixture ranges from approximately 560 to 670 nm. To achieve a narrower spectral linewidth, the laser cavity is equipped with a pair of diffraction gratings and two prisms, by rotating one of the gratings, the wavelength of the output beam can be precisely adjusted and the resulting laser linewidth is around 2 GHz. With a pump power of 5.9 W, the system generates 230 mW of yellow light with repetition rate of 10 kHz, pulse duration of 20 ns, and linear polarization. Then, these laser pulses are delayed by around 300 ns using an optical fiber to ensure that the electrons are in proximity to the Mott detector when the yellow laser pulses hit the sodium beam. The interaction of circularly polarized light with the sodium atoms changes their spin polarization state and because of the entanglement, this also shall polarize the beforehand unpolarized electron beam. Finally, the spin polarization of electron beam is measured using a Mott detector.

In the following sections, comprehensive explanations of design and computational simulations for each part are provided.

3.2 Electron Gun

3.2.1 Material and Thickness Considerations

As previously discussed, we require an electron gun that generates 10 eV electrons in pulsed mode. For this purpose, a laser-driven source based on the photoelectric effect has been implemented. It is important to note that the energy of the incoming photons must be equal to or greater than the binding energy that holds the electrons in place or the

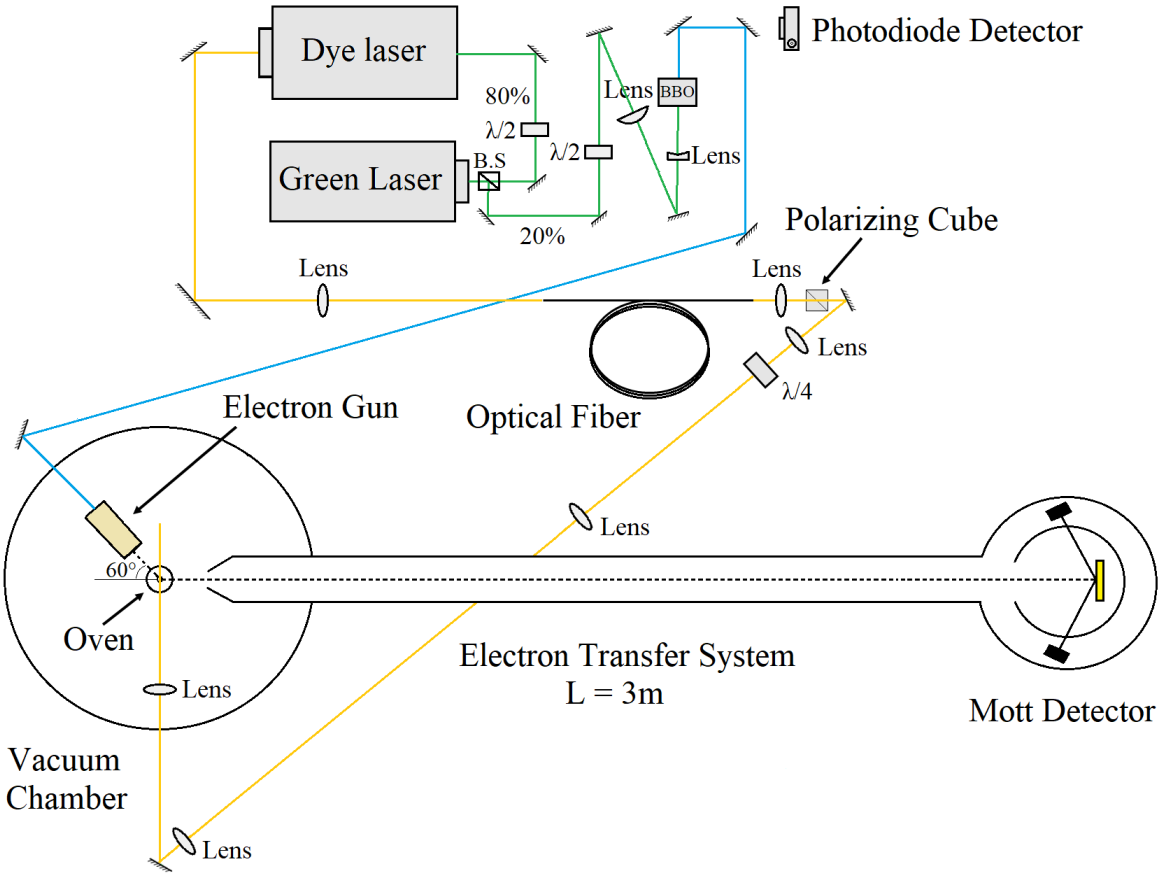

Figure 3.1: Sketch of the full experimental setup.

work function, W, of the material.

Another critical aspect to consider when aiming to maximize electron production through the photoelectric effect is the material's quantum efficiency QE. Quantum efficiency is a measure of how efficiently incoming photons are converted into emitted electrons and it is defined as the number of electrons emitted per incident photon [35].

Consequently, for an experiment aiming to maximize electron production through the photoelectric effect, careful consideration of the work function and the material's quantum efficiency is essential. In this context, Table 3.1 provides work function and quantum efficiency values of some materials.

Since we use UV light with energy of 4.66 eV per photon, to generate electrons it is imperative to select materials with work functions below 4.66 eV and close to this value.

Material	**Work function (eV)**	**Quantum efficiency (10^{-4})**
Palladium	5.00	0.12
Nickel	4.40	0.25
Zirconium	4.30	0.10
Gold	4.30	0.47
Copper	4.65	1.00
Silver	4.30	0.20
Tantalum	4.25	0.10
Zinc	3.70	0.14
Magnesium	3.66	6.20
Terbium	3.00	2.35
Yttrium	2.90	5.00
Samarium	2.70	7.25

Table 3.1: Work functions and quantum efficiencies of some materials at wavelength 266 nm [35].

This selection is essential to ensure that emitted electrons from the material have minimal energy, because the initial energy of these electrons significantly impacts their ultimate energy that should ideally reach 10 eV.

Furthermore, the choice of materials is not solely influenced by the work function considerations. Factors such as material oxidation and magnetic characteristics must also be taken into account. Notably, materials like copper, due to their propensity for oxidation, may exhibit changes to the work function and to the quantum efficiency, potentially affecting the reliability of experimental outcomes. Additionally, materials like nickel, characterized by magnetic properties, may introduce undesirable effects in the experiment. Taking all these factors into account, the optimal choice for our experiment, which aligns with the specified energy criteria and minimizes potential interference, is **silver**. Also, an optimal substrate for our purposes is sapphire due to its characteristics, including high UV light transmissivity, higher thermal conductivity compared to materials such as quartz or magnesium fluoride, and compatibility with vacuum conditions.

In the context of photoemission under back-illumination, the photocurrent is influenced by two opposing factors. For films thinner than the UV light's absorption length, α, the

photon absorption within the silver film increases as the film thickness increases, resulting in a higher photoelectron yield. Conversely, in thicker films exceeding the electron's inelastic mean free path, λ_e, electron emission mainly occurs from a surface layer with a thickness determined by λ_e. As thickness increases, the emission reaches to its maximum value and then decreases with the UV light's absorption length, α^{-1}. This behavior aligns with the Lambert-Beer law for UV light intensity attenuation and an exponential reduction in the number of excited electrons due to inelastic scattering. A corresponding expression for photocurrent as a function of film thickness can be derived [36] as

$$I_e(d) = I_0 \frac{\alpha\lambda_e}{1-\alpha\lambda_e}\left(\exp(-\alpha d) - \exp\left(-\frac{d}{\lambda_e}\right)\right), \tag{3.1}$$

where d denotes the film thickness, λ_e stands for the electron inelastic mean free path, α represents the absorption coefficient for UV light, and I_0 is a constant value.

In our specific case, we use a silver layer where the absorption length of the UV light α^{-1} is 16 nm, and λ_e is 5.1 nm. By substituting these values into Eq. (3.1), we can determine the optimal thickness of the silver layer. As shown in Fig. 3.2, this optimal thickness is around 9 nm, which is the thickness we need to coat on the surface of the substrate.

3.2.2 Electron Optic Design

The design of the electron optics system plays an important role in the construction of an electron gun. Within our research group, prior attempts at electron gun design and testing have been conducted [37, 38] and these designs have faced some challenges and did not work properly. Therefore, the following parameters are critical for ensuring the optimal performance of the designed electron gun:

1. The electron beam profile should remain consistent despite variations in the initial kinetic energy of emitted electrons. Alternatively, it should be adjustable by varying the voltage settings of the electron lens system. This flexibility is essential

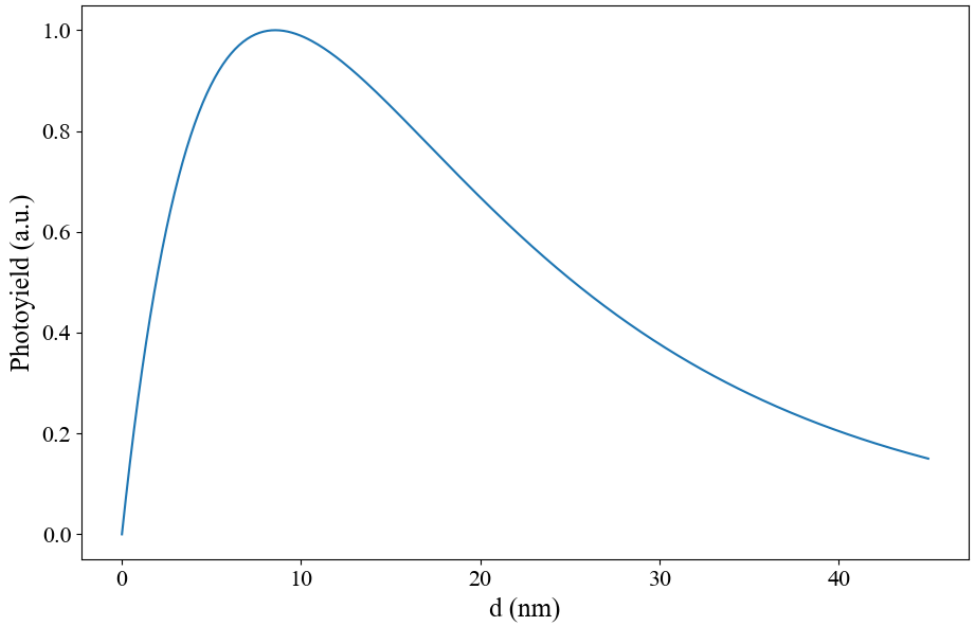

Figure 3.2: The photoelectron yield as a function of the Ag film thickness is calculated based on a simplified model that exclusively considers the processes of light absorption and inelastic scattering of the excited electrons.

because variations in material composition and coating techniques may lead to slight differences in the work function of thin films, which should not impact the electron beam profile.

2. In order to assess the scattering process effectively, it is necessary to have the capability to change the focal point of emitted electrons. Additionally, for having more flexibility in the experiment, it is important to generate a collimated electron beam.

3. Since the electron gun is back illuminated, it is imperative to establish mechanisms that either prevent or significantly reduce the intensity of transmitted UV light from the cathode within the electron gun. This is not only required for the characterization of the electron gun properties but also for preventing any interaction of UV photons with the Sodium beam in front of the electron gun, which could potentially change the experimental results.

4. The simulations show that entanglement is expected to be maximized at 10eV electron energy. Consequently, the electron gun must deliver this energy with minimal spread to ensure optimal entanglement generation.

Based on the mentioned considerations, an alternative design for a laser-driven electron gun is introduced. This design incorporates a half sphere sapphire substrate, which is coated with a layer of silver. Ultraviolet (UV) light is directed towards the back side of this half sphere, where the photoelectrons are generated. Subsequently, these photoelectrons are transported to the target atoms via 8 electron lenses of the electron gun. Fig. 3.3 shows the first prototype of the designed electron gun.

The performance of the new electron gun design was evaluated using SIMION simulations. In particular, the capability to adjust the focal point and the size of the electron beam was investigated. Furthermore, the insensitivity to variations in electron kinetic energy has been tested. A simulation result for the electron trajectories with initial energies of 0.1 and 0.3 eV is shown in Fig. 3.3. The results demonstrate minimal difference in the trajectories for these different initial energies, confirming the design's robustness to work function variations.

In this particular design, the half-sphere serves a dual purpose. Initially, it functions as a substrate for the silver layer deposition. Additionally, its curvature allows it to act as a lens for UV light. In this case, the transmitted UV light effectively converges at a focal point located 3.5 mm behind the lens. Thereafter UV beam begins to diverge, resulting in a significantly enlarged beam size and consequently the intensity of the UV beam at the interaction region is very low and expected not to affect the sodium atoms.

Taking all these considerations and experimental boundary conditions into account, the final electron gun has been designed and manufactured. The CAD view of the electron gun is depicted in Fig. 3.4.

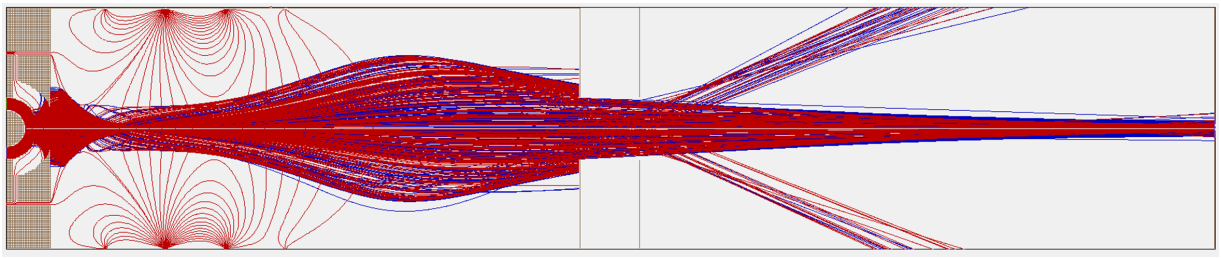

Figure 3.3: The proposed electron gun with half sphere sapphire. The initial kinetic energy of the red electrons after photo-excitation is 0.1 eV, while for the blue electrons, it is 0.3 eV.

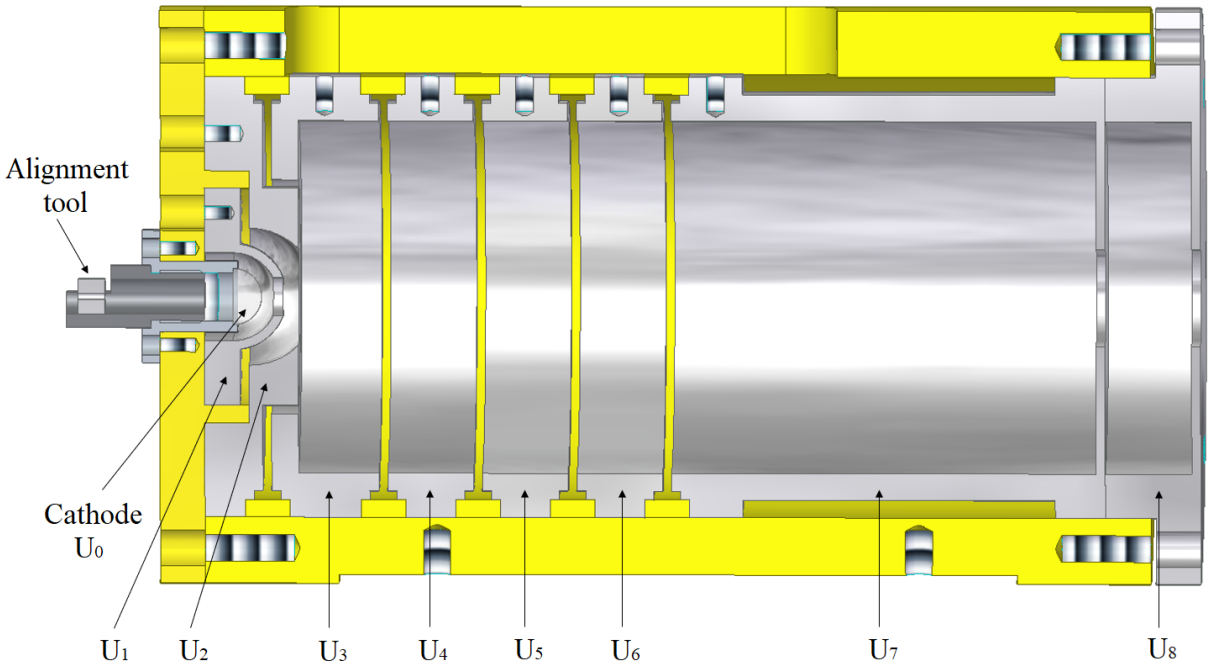

Figure 3.4: CAD view of the designed electron gun. The yellow parts are insulator parts (made of Delrin) for holding electrodes together and the gray parts are electrodes made of aluminum.

3.2.3 Impact of UV Light Size on Electron Gun Performance

The initial simulations, as depicted in Fig. 3.3, indicate that when the entire surface of the silver layer is exposed to UV light, the trajectories of the resulting electrons can vary significantly depending on their initial positions on the silver layer. As can be seen, a significant fraction of the generated electrons are not escaping the lens system but are hitting one of the electrodes. This potentially leads to the generation of secondary electrons

that may escape from the electron gun and affect the energy distribution of the output beam.

Furthermore, some electrons escape from the electron gun with divergent trajectories, and it is impossible to control their paths precisely. Our ability to control electron trajectories is limited to those generated from the central region of the silver-coated sapphire sphere. Therefore, precise control of both the size and position of the UV beam on the silver layer is critically important.

Fig. 3.5 illustrates the impact of the UV beam size on the electron gun's output. The simulations clearly show that using a small UV light beam is important for the optimal performance of the electron gun. However, two factors constrain the UV spot size on the photocathode, namely coating damage and high charge density, the latter resulting in space charge effects that can negatively impact beam trajectory and energy. Taking all these factors into account, it is important to use a UV beam with a diameter ranging from 0.3 to 0.5 mm to get a better beam profile.

The voltage settings for the electron gun electrodes used for the simulations shown in Fig. 3.5 are provided in Table 3.2. Essentially, the focal point position can be adjusted by changing the voltages applied to $U5$ and $U6$.

U_0	U_1	U_2	U_3	U_4	U_5	U_6	U_7	U_8
-10	150	-10	-45	1	350	80	0	0

Table 3.2: Operating voltage set for the optimal performance of the electron gun.

3.2.4 Output Energy and TOF of Electrons

In the experiment, it is important to generate an electron beam with an energy of 10 eV and a narrow energy distribution. To assess the energy distribution of the electrons emitted by the electron gun, we need to consider the kinetic energy of electrons generated through the photoelectric effect, which is calculated as $E_{kin} = E_{photon} - W$. In our specific case,

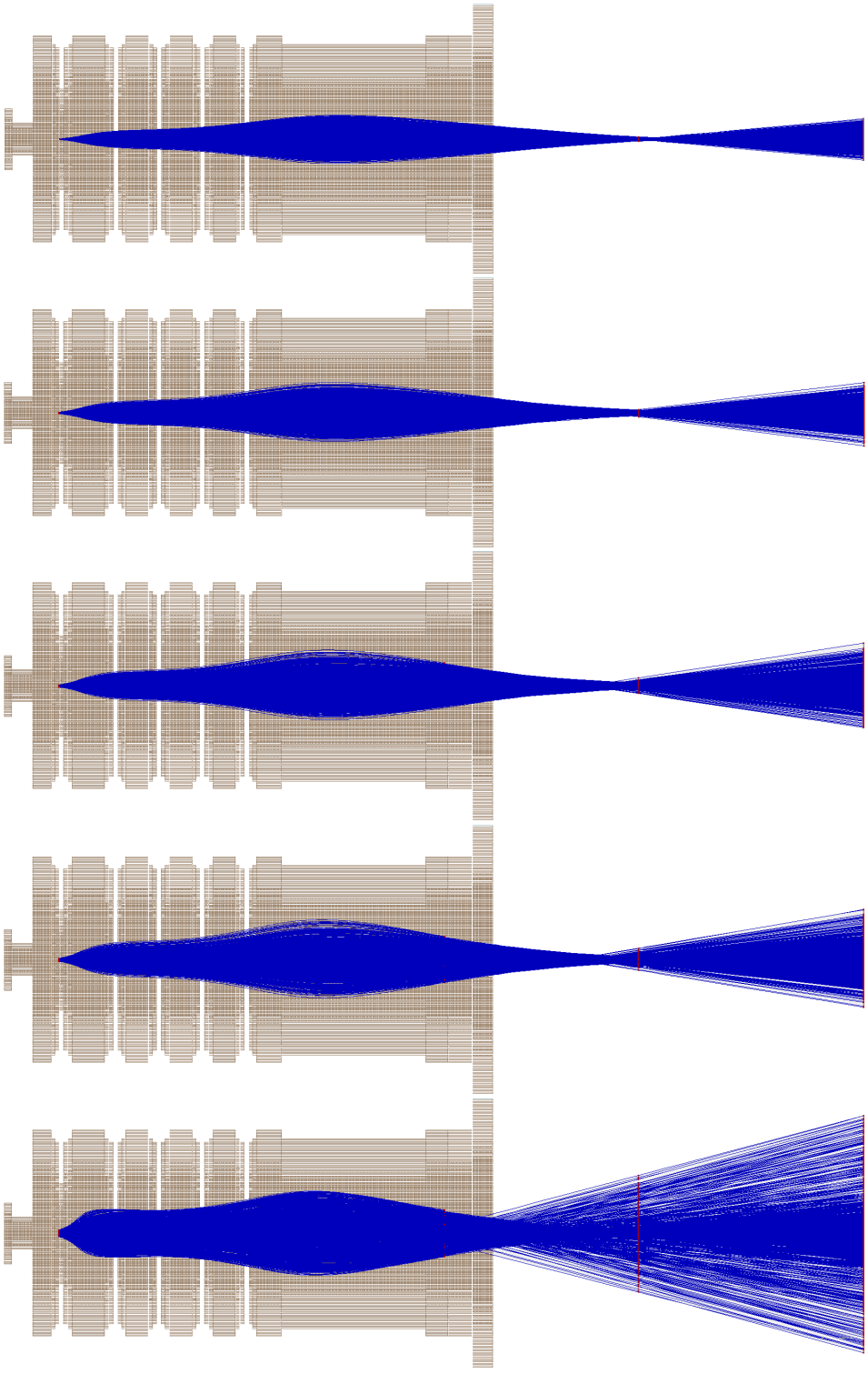

Figure 3.5: Effect of UV beam size on the output of the electron gun. The beam diameter is 0.1, 0.3, 0.5, 0.7, and 1.5 mm from top to bottom respectively. The effect of space charge is not considered in these simulations.

with $E_{photon} = 4.66\,\text{eV}$ and assuming a typical work function of 4.3 eV for silver, the initial kinetic energy of the emitted electrons is approximately 0.36 eV.

Regarding the spectral bandwidth of the UV light utilized in the experiment, it is crucial to consider that the bandwidth can affect the energy distribution of the emitted electrons. But, in our experimental setup, the UV light has a bandwidth of less than 1 nm. This results in a minor variation in photon energy. However, the overall impact on the initial kinetic energy distribution of the electrons is negligible.

It is also important to consider that the work function of a material, such as silver, can exhibit variability due to factors like surface conditions, impurities, or crystallographic orientation. This variation introduces a distribution in the work function value. While the distribution of work function values for a specific material might not precisely have a Gaussian distribution, it is often approximated as such, particularly when variations arise from random factors or uncertainties. Fig. 3.6a illustrates the simulation results using SIMION software and demonstrates the impact of work function variations on the energy distribution of electrons beam from electron gun. It shows that the FWHM of the energy distribution may vary between 0.4 to 0.8 eV. Due to the hardly controllable nature of the coating process, this variation can lead to different resulting energy distributions for each cathode coating process, which may cause slight discrepancies in the measurement.

Moreover, the simulations show that the size of the UV beam on the cathode has an effect on the energy distribution and by reducing the size of the UV beam we can have a narrower energy distribution. However, as mentioned earlier, reducing the beam size leads to a higher electron density within a confined space, resulting in electron repulsion, which, in turn, contributes to an increased energy distribution of the generated electrons. Fig. 3.6b shows the effect of UV beam size on the energy distribution of the electron beam generated by the electron gun.

Another critical parameter in our experiment is the Time of Flight, TOF, of the electrons throughout the entire setup. Therefore, it is important to know the TOF of

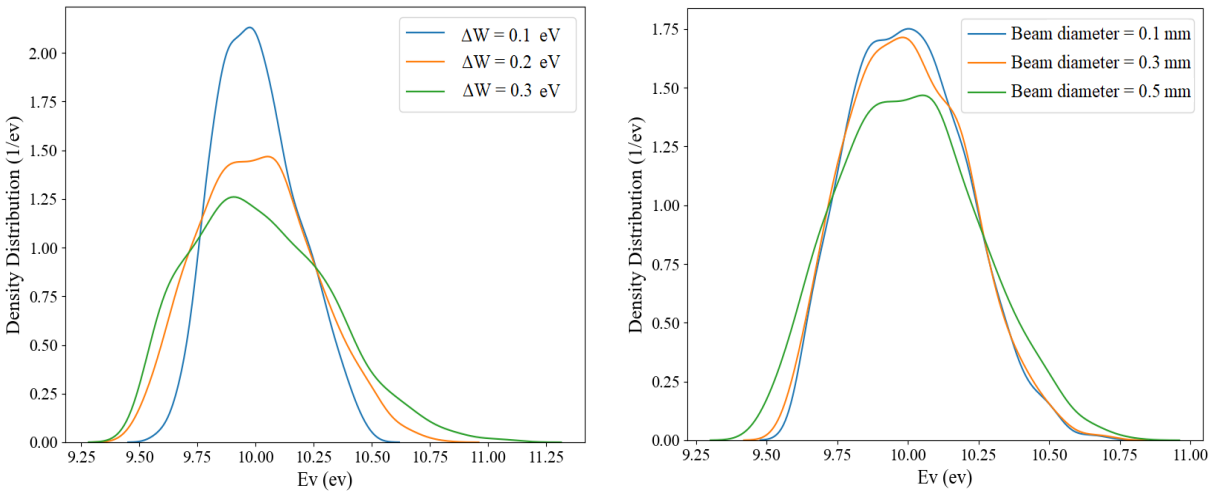

(a) (b)

Figure 3.6: (a) Energy distribution of the electron beam for different values of the work function broadening, with a UV beam size of 0.5 mm. (b) Energy distribution of the electron beam for different UV bean sizes, assuming $\Delta W = 0.2$ eV. In these simulations the effect of space charge is not considered.

the created electrons from the cathode to the interaction region. Ideally, if all electrons were created simultaneously, their TOF to the interaction region would be approximately 53 ns, with a broadening of less than 1 ns. However, due to the laser pulse width, electrons are not generated simultaneously, leading to a broader distribution.

Since the measured pulse duration for UV light is 20 ns, we take this value into account for the electron generation timing, the broadening of the resulting electron distribution increases to about 30 ns. Fig. 3.7 presents the simulation results for the TOF of the generated electrons from cathode to the interaction region, which is located 3.5 cm from the exit of the electron gun. The simulations show that the TOF of electrons is not significantly influenced by variations in the work function distribution or the UV beam size.

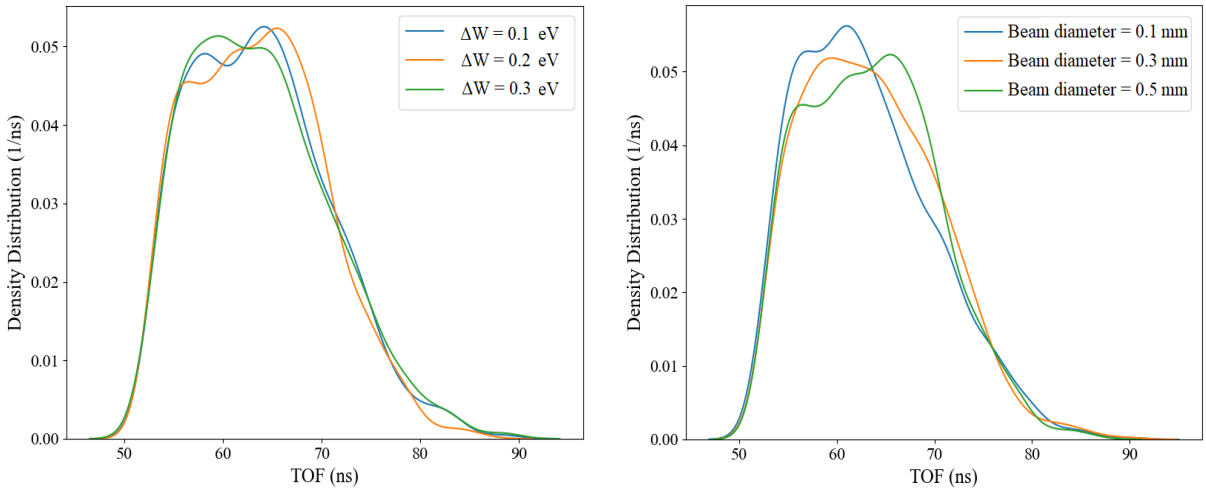

(a) (b)

Figure 3.7: (a) The energy distribution of the electron beam for different values of work function broadening, with a UV beam size of 0.5 mm. (b))The TOF distribution of generated electrons from cathode to the interaction region by considering $\Delta W = 0.2$ eV.

3.3 Oven

An essential aspect of this experiment is the precise and controlled generation of a sodium atomic beam. Since the elastic differential cross section of sodium atoms for electrons with 10 eV energy at 60° is very low ($1.85\, a_0^2\, sr^{-1}$), we require a well-collimated atomic beam over long distances with maximum intensity at the interaction region. In the following some important factors that should be considered in the design of the oven for our experiment are elaborated.

- Due to the high reactivity of alkali metal vapors — sodium in our experiment— they can quickly contaminant the vacuum chamber and all of the optical elements inside it. As discussed in Section 2.3, to minimize the amount of sodium introduced into the vacuum chamber we cannot use a simple oven with an orifice but need to utilize an oven with a tube to generate a well-collimated atomic beam.

- The next factor for consideration is the potential for clogging or blockage of the tube due to condensation of atomic vapor. Therefore, it is essential to heat the main part

of the oven and its tube separately and keep a tube temperature of 10 to 20°C higher than the temperature of the main oven. This temperature differential ensures that sodium vapor remains above its condensation point throughout the beam path.

- Another critical factor to consider in our experiment is the sensitivity of the scattering process to magnetic fields. Thus, it is important that the employed heating mechanism does not generate any magnetic field. Also, the material used for the oven must be non-magnetic to avoid generating any undesired magnetic fields in the interaction region.

- The final factor is that the material used to construct the oven not only should not melt, but also it should not react with sodium. This is essential to prevent any undesirable chemical reactions between the oven material and the sodium atoms.

By taking into account all of aforementioned considerations, we have designed an oven, as illustrated in Fig. 3.8. The oven is constructed from 316-grade stainless steel. It is resistant to corrosion and also it is a non-magnetic material, which does not introduce any unwanted magnetic fields that could affect the scattering process.

For heating the oven, two heaters are employed: a simple Nickel-Chromium wire for heating the main part and a ceramic heater for the tube part of the oven. This dual heater allows independent temperature control of the main and tube parts by applying different currents to each one and then maintain the different temperature that we need. Also, to monitor the oven's temperature during experiments, a temperature sensor is included in the design.

The oven is equipped with an external shield for two purposes. Firstly, it prevents heat dissipation from the oven for efficient heating. Secondly, it prevents charging up of the insulators around the heaters. This is crucial as the oven is positioned near the electron gun, and any accumulation of charges on the surface could generate unwanted electric fields, potentially affecting the scattering process.

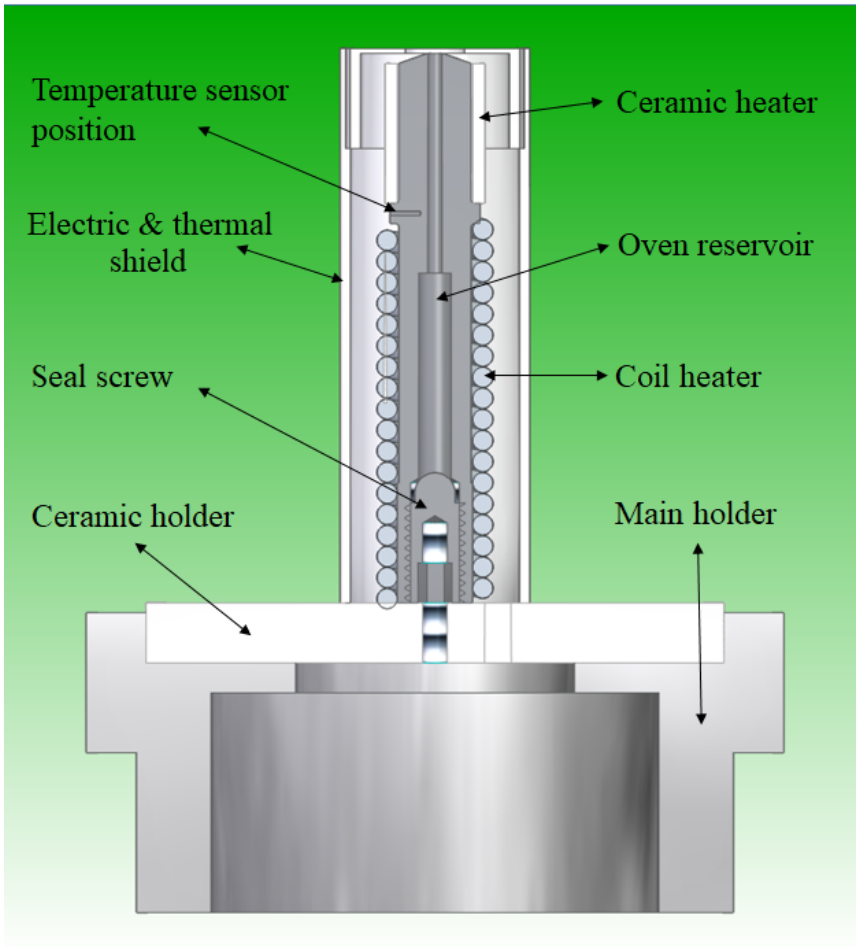

Figure 3.8: The designed oven for generating an atomic sodium beam.

In this design the length of the tube is 22 mm and its diameter is 1.5 mm, which in this case yields $\Gamma = l/d = 14.7$. Also, the oven reservoir has a diameter of 3.3 mm and a length of 22 mm, giving it a volume of around 188 mm^3. Given the density of sodium, which is 0.97 mg/mm^3, , the oven can accomodate approximately 190 mg of sodium.

To evaluate the output parameters of the oven, the mean free path of the atoms within the oven must be examined. Fig. 3.9b illustrates this parameter as a function of temperature. The plot is generated by applying the vapor pressure of sodium atoms from Eq. (2.46), which is shown in Fig. 3.9a, into Eq. (2.34). As can be seen, for temperatures above 340°C, the mean free path is less than 1.5 mm ($d = 1.5$ mm). Therefore, to safely be allowed to use the equations from Section 2.3, the temperature should be kept below

this threshold.

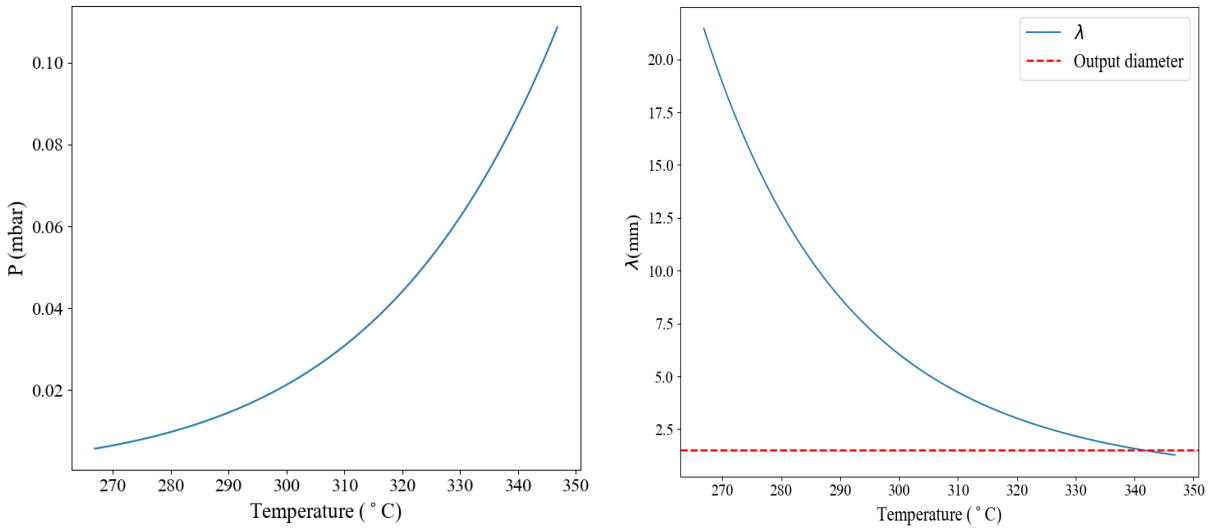

(a) (b)

Figure 3.9: (a)Vapor pressure of the sodium atoms inside of the oven. (b) The mean free path of sodium atoms.

By considering the above conditions, the throughput N and the axial intensity $I(0)$ of the designed oven are plotted as a function of temperature in Fig. 3.10, and in addition, a comparison is made between an oven with an orifice and a tube. This figure indicates that the throughput of the oven with an orifice is ten times higher than the designed oven. However, in the temperature range from $300°C$ to 320°C, where the experiment will be conducted, the axial intensity of the designed oven is nearly half of the oven with orifice. As a result, using a tube instead of an oven causes a ten fold reduction in load on the vacuum system.

The most important parameter for the oven in our experiment is the number density of sodium atoms in the interaction region. Fig. 3.11 depicts the variation of this parameter as a function of temperature 8 mm above the output of the oven. The depicted values indicate that a sufficiently high number density of sodium atoms in the interaction region can be achieved.

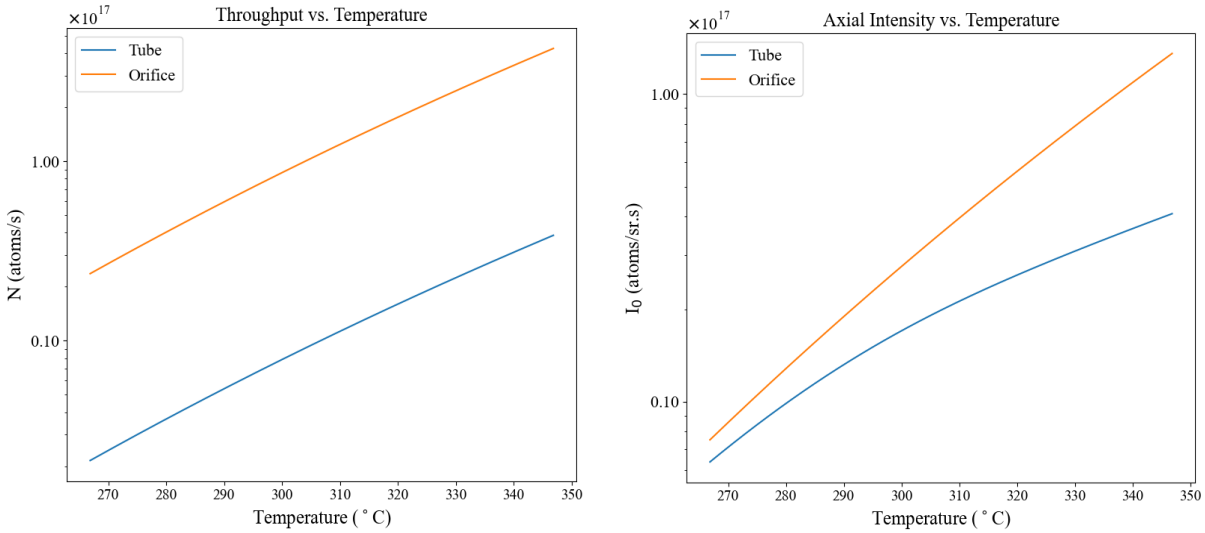

Figure 3.10: The logarithmic plot for (a) throughput and (b) axial intensity as a function of temperature, comparing a design with a tube against an orifice.

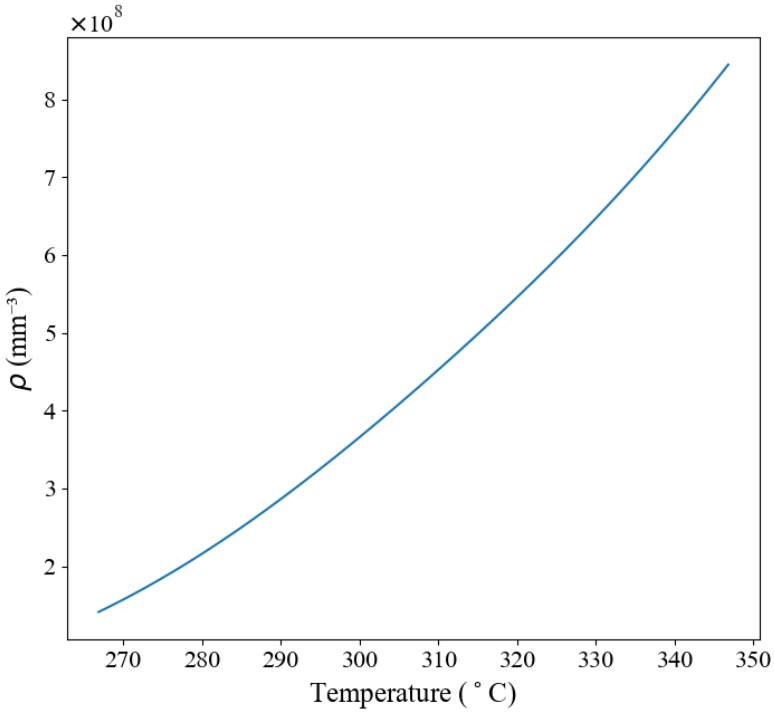

Figure 3.11: The number density of sodium atoms 8 mm above the output of the oven.

3.4 Rate Equations in Photo-Excitation Process

In section 2.1 it is mentioned that we need to change the spin polarization of the sodium atoms by photo-excitation from the ground state $^2S_{1/2}$ to the fine structure state $^2P_{1/2}$ using a precisely tuned laser with photons that are purely right-handed (σ^+) circularly polarized (or positive helicity). According to the selection rules, σ^+ photons can induce transitions that result in a change in the magnetic quantum number $\Delta m_j = +1$. This means that an electron in the $m_j = -1/2$ sublevel of the $^2S_{1/2}$ state can be excited to the $m_j = +1/2$ sublevel of the $^2P_{1/2}$ state. Conversely, photons with negative helicity (σ^-) would induce $\Delta m_j = -1$ transitions. By selectively using σ^+ polarized light, we can control the population of specific magnetic sublevels, thereby polarizing the sodium atoms in a desired spin state.

Photo-excitation usually is not a one-way process. After stimulated absorption, the excited $^2P_{1/2}$ state de-excites back to the $^2S_{1/2}$ ground state, depending on its natural lifetime. This decay can occur via either stimulated or spontaneous emission. While both stimulated absorption and emission are proportional to and dependent on the energy of the laser, spontaneous emission is not. Another process that could happen is spin-relaxation between $m_j = +1/2$ and $m_j = -1/2$ sublevels of the ground state. However, since the spin-relaxation rate is typically around 500 s^{-1} for alkali metals [39] and we are interested in nanosecond timescales, we can safely ignore this effect. Fig. 3.12 depicts the all processes that can occur during the optical pumping of a sodium atom using right-handed circularly polarized light.

To obtain detailed insights into the time scale of photo-excitation, we need to solve the rate equations for the relevant energy levels. Let N_i and N_k represent the occupation numbers of $m_j = +1/2$ and $m_j = -1/2$ magnetic sub-levels of the $^2S_{1/2}$ atomic ground state, respectively, and let N_j denote the occupation number of the excited $m_j = +1/2$ magnetic sub-level of the $^2P_{1/2}$ state. This leads to a set of three coupled first-order

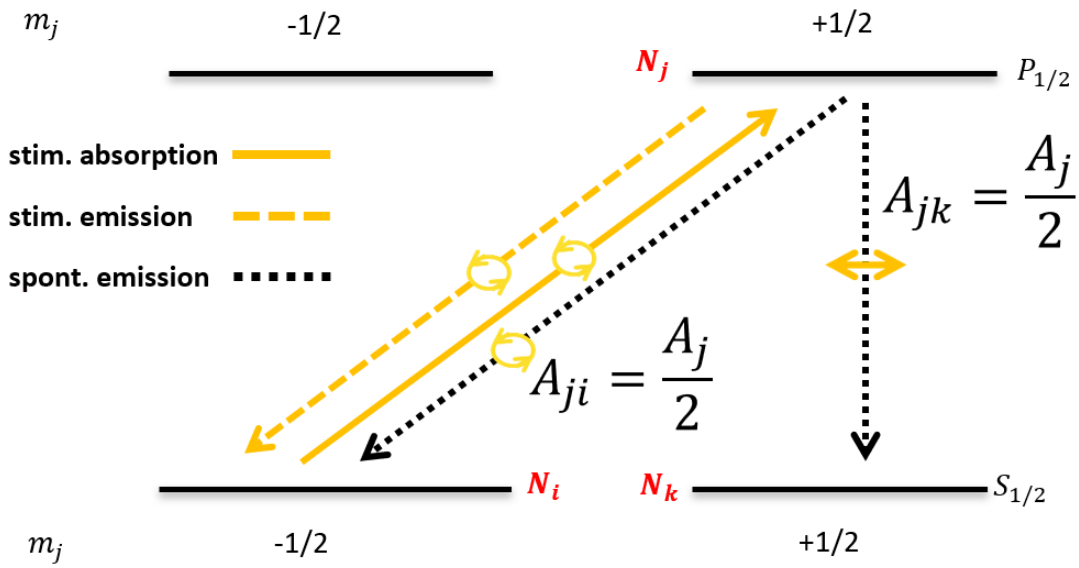

Figure 3.12: Optical pumping scheme for Na atoms with circularly polarized σ^+ light for the D_1-line at $\lambda = 589.756\,\text{nm}$. Taken from Lohmann et al.[27].

differential equations:

$$\begin{aligned}
\frac{d}{dt}N_i &= -B_{ij}U_\omega N_i + (B_{ji}U_\omega + A_{ji})N_j \\
\frac{d}{dt}N_j &= B_{ij}U_\omega N_i - (B_{ji}U_\omega + A_{ji} + A_{jk})N_j \\
\frac{d}{dt}N_k &= A_{ji}N_j,
\end{aligned} \tag{3.2}$$

where Aij and B_{ij} are the Einstein coefficients and U_ω is the energy density per unit angular frequency interval of the laser. Initially, we will consider U_ω as a constant value to derive an analytical solution. However, a numerical solution with a time-dependent profile will be provided later in the equations.

The Einstein coefficients are related to each other via $g_i B_{ij} = g_j B_{ji}$, where g_i and g_j are the degeneracy factors of the two populated states. In our case, the sub-states are non-degenerate and hence, $g_i = g_i = 1$ and thereby, $B_{ij} = B_{ji}$. Additionally, for the Einstein coefficients of spontaneous emission, we have

$$\sum_l A_{jl} = A_{ji} + A_{jk} = \frac{1}{\tau}, \tag{3.3}$$

where $\tau = 16.3\,\text{ns}$ is the natural lifetime of the excited $^2P_{1/2}$ state of the sodium atom [40]. Since we have $A_{jl} = A_j/2$ for $l = j, k$ we can simplify Eq. (3.2) as

$$\begin{aligned}
\frac{d}{dt}N_i &= -B_{ij}U_\omega N_i + \left(B_{ij}U_\omega + \frac{A_j}{2}\right)N_j \\
\frac{d}{dt}N_j &= B_{ij}U_\omega N_i - (B_{ij}U_\omega + A_j)N_j \\
\frac{d}{dt}N_k &= \frac{A_j}{2}N_j.
\end{aligned} \tag{3.4}$$

In this case, by employing the matrix exponential method, we can solve these first-order linear differential equations, which yields the following solutions

$$N_i(t) = \frac{N_0}{4\kappa}\left[(\kappa + A_j)e^{\frac{1}{2}(\kappa-\delta)t} + (\kappa - A_j)e^{-\frac{1}{2}(\delta+\kappa)t}\right], \tag{3.5}$$

$$N_j(t) = \frac{N_0 B_{ij}U_\omega}{2\kappa}\left[e^{\frac{1}{2}(\kappa-\delta)t} - e^{-\frac{1}{2}(\delta+\kappa)t}\right], \tag{3.6}$$

$$N_k(t) = \frac{N_0}{2}\left\{1 + \frac{B_{ij}U_\omega A_j}{\kappa}\left(\frac{e^{\frac{1}{2}(\kappa-\delta)t} - 1}{\kappa - \delta} + \frac{e^{-\frac{1}{2}(\delta+\kappa)t} - 1}{\delta + \kappa}\right)\right\}, \tag{3.7}$$

where N_0 is the total occupation number of all participating levels i, j, k, such that $N_0 = N_i(t) + N_j(t) + N_k(t)$. We implicitly assume that before photo-excitation, the excited j-level is empty and both magnetic sub-levels i and k of the ground state are equally populated. Fig. 3.13a shows the occupation numbers of sub-levels over time. Additionally, for these equations, we used the following abbreviations

$$\kappa = \sqrt{4(B_{ij}U_\omega)^2 + 2B_{ij}U_\omega A_j + A_j^2} \qquad \text{and} \qquad \delta = 2B_{ij}U_\omega + A_j. \tag{3.8}$$

From these occupation numbers, the degree of spin polarization, P, of sodium atoms can be obtained as a function of time, where the spin polarization is defined as

$$P = \frac{N_k + N_j - N_i}{N_k + N_j + N_i}. \tag{3.9}$$

Fig. 3.13b illustrates the spin polarization of the sodium atoms over time. To understand the effect of laser energy on the spin polarization of sodium atoms, we first define the characteristic laser energy $U_{\omega,char}$ such that $B_{ij}U_{\omega,char} = A_j$, and considering the relation [41]

$$B_{ij} = \left(2\pi^3 c^3/h\omega_{ij}^3\right) A_j, \tag{3.10}$$

where we can determine that its value for D_1 line of sodium is $U_{\omega,char} = 1.29 \times 10^{-14}\ \frac{\mathrm{J}}{\mathrm{m^3 \cdot Hz}}$.

As shown in Fig. 3.13b, higher laser energy results in faster spin polarization of the sodium atoms. For instance, when the laser energy is equal to $U_{\omega,char}$ the spin polarization $P = 50\%$ is reached after $t = 50$ ns. Conversely, when the energy is $100\,U_{\omega,char}$ the spin polarization $P = 50\%$ is reached after $t = 300$ ps. Furthermore, these simulations reveal that achieving higher levels of spin polarization requires more time. For instance, to reach a spin polarization greater than 70%, we need to wait more than 55 ns. Furthermore, even with increased laser energy, we cannot achieve significantly better spin polarization within a shorter time frame.

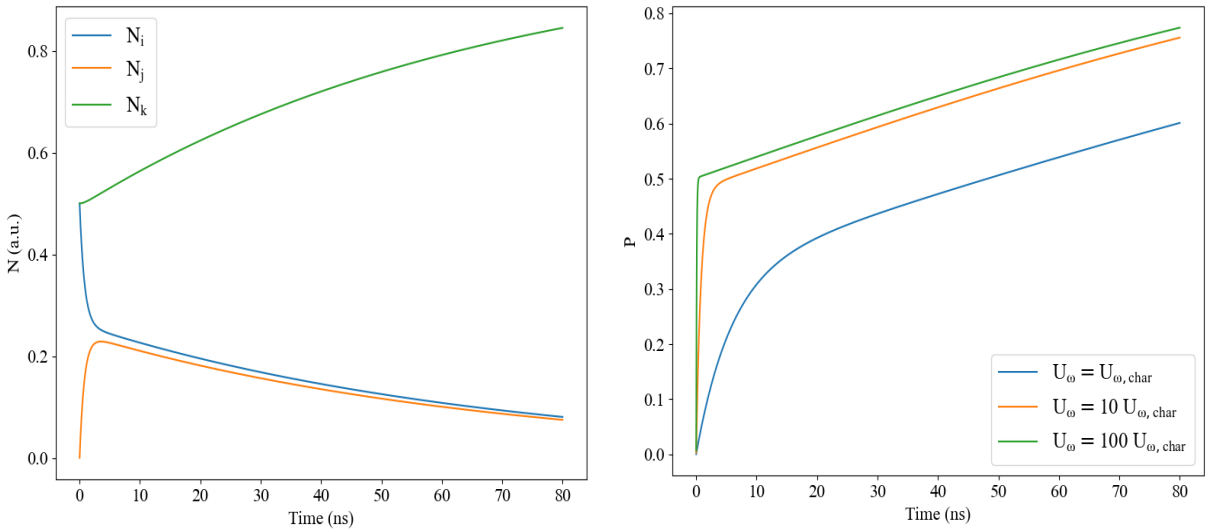

(a) (b)

Figure 3.13: (a) Occupation numbers of different sublevels over time for $U_\omega = 10\,U_{\omega,char}$. (b) Spin polarization of sodium after photo-excitation over time for different values of U_ω.

In the above solutions, we assumed that U_ω is constant. However, in the experiment,

we utilize a pulsed laser with a Gaussian distribution of 20 ns FWHM. This makes finding an analytical solution challenging and we need a numerical approach to determine the evolution of the spin polarization of sodium atoms over time. We can express U_ω as $U_\omega = U_{laser} \exp^{-\frac{1}{2}(\frac{t}{\sigma})^2}$, where σ is the standard deviation related to the FWHM of the laser by $FWHM = 2\sqrt{2}\ln\sigma$ and U_{laser} is the amplitude of the energy density per unit angular frequency interval of the laser. Using a laser peak power of 225 W at 589.76 nm, 10 kHz repetition rate, 2 GHz bandwidth, and 5 mm beam diameter at the interaction region as typical values for the used laser system, this yields $U_{laser} = 1.53 \times 10^{-11}\ \frac{\mathrm{J}}{\mathrm{m^3 \cdot Hz}}$.

We can numerically solve the rate equations to determine the time evolution of sodium atom spin polarization. Fig. 3.14 shows the result of simulations. The polarization very quickly reaches approximately 50% and then rises to 65% within the next 30 ns. Afterwards a slight decrease can be observed. This shows that in the best case a degree of spin polarization of 65% can be measured by the Mott detector if the timing is set accordingly.

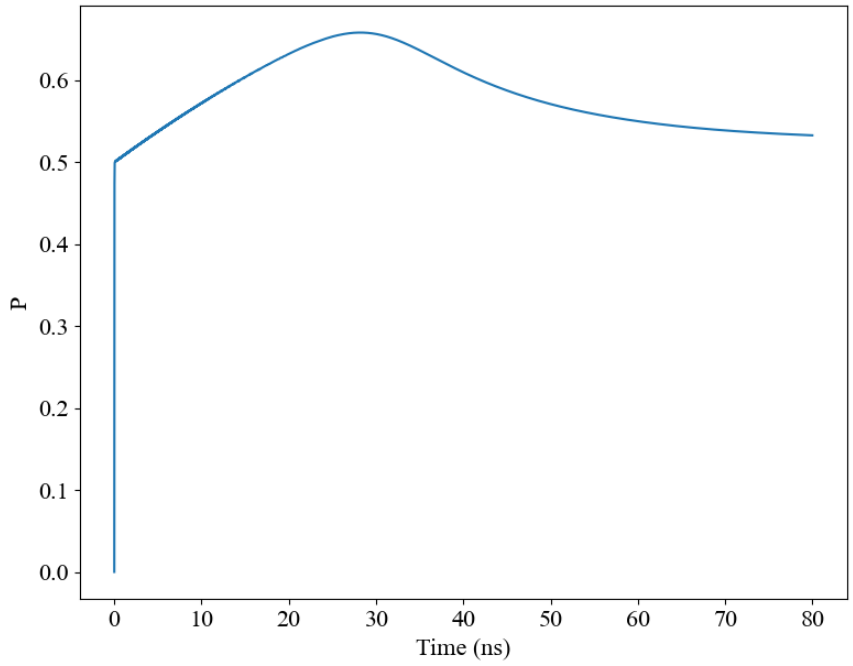

Figure 3.14: Spin polarization of the sodium atoms against time by considering the parameters of the laser.

3.5 Earth's Magnetic Field Compensations

First tests show that due to the low energy of generated electrons by the electron gun, these electrons are highly sensitive to the external magnetic fields, such as the Earth's magnetic field. Consequently, these electrons can be easily deflected by magnetic forces. As they travel from the electron gun to the interaction region, the electrons may experience deflections or alterations in their trajectories, potentially deviating from their intended path and missing the desired interaction point with the sodium atoms. Furthermore, the Earth's magnetic field can significantly affect the scattering process of the electrons as they interact with the sodium atoms.

To ensure the accuracy and reliability of our experimental outcomes, it became important to implement a magnetic field compensation system for neutralizing the Earth's magnetic field effects, that allows us to maintain precise control over the electron trajectories and their interactions with the sodium atoms in the experiment.

Magnetic field compensation can be achieved through two primary methods: active or passive compensation. Active compensation involves the generation of a magnetic field in the opposite direction of the Earth's geomagnetic field. This opposing magnetic field is carefully controlled to counteract the ambient magnetic field components, allowing for the creation of the desired magnetic field distribution within the experimental volume. The result is a magnetic field environment, where external magnetic influences are effectively neutralized, ensuring the absence of interference with the experiment.

Passive compensation, on the other hand, relies on the use of specially designed materials that are capable of redirecting, concentrating, or neutralizing the external magnetic fields. One common material used in passive systems is μ-metal, which has high magnetic permeability. μ-metal shields are designed to redirect and absorb magnetic field lines, reducing their impact within the shielded region. By strategically placing μ-metal shields around the experimental setup, we can effectively create a region, where

the Earth's magnetic field is significantly reduced or canceled out. This passive approach ensures that electrons can maintain their intended trajectories.

In our experiment, we employ a combination of both methods for compensating the Earth's magnetic field. For the main chamber, where the electron gun operates and the scattering process takes place, we implement active compensation methods, utilizing an array of Tri-axial Square Helmholtz (TSH) coils, consisting of an array of three square Helmholtz coils pairs. On the other hand, for the electron transfer system, we strategically wrap μ-metal shielding around it as part of our passive compensation approach. This dual approach allows us to effectively manage and neutralize the impact of the Earth's magnetic field across different components of our experimental setup.

In the design process of the Helmholtz coils, we begin by analyzing the vector potential for a rectangular wire loop positioned within the $x-y$ plane. Subsequently, we compute the vector components of the magnetic flux density by applying the following relationships [42]

$$B_x = -\frac{\partial A_y}{\partial z}, \qquad B_y = \frac{\partial A_x}{\partial z}, \qquad B_z = \frac{\partial A_y}{\partial x} - \frac{\partial A_x}{\partial y}. \tag{3.11}$$

The vector potential components for a single rectangular loop of wire with negligible wire cross section and side dimensions of 2a by 2b, as depicted in Fig. 3.15a, are [42]

$$A_x = \frac{\mu_0 I}{4\pi} \ln\left(\frac{(r_1+a+x)(r_3-a+x)}{(r_2-a+x)(r_4+a+x)}\right), \tag{3.12}$$

and

$$A_y = \frac{\mu_0 I}{4\pi} \ln\left(\frac{(r_2+b+y)(r_4-b+x)}{(r_3-b+y)(r_1+b+y)}\right), \tag{3.13}$$

where μ_0 refers to the magnetic permeability of a vacuum, while I denotes the current in the loop. The variables r_1, r_2, r_3, and r_4 represent the distances from the loop's corners to the specific point $P(x, y, z)$, where the magnetic flux density is under assessment.

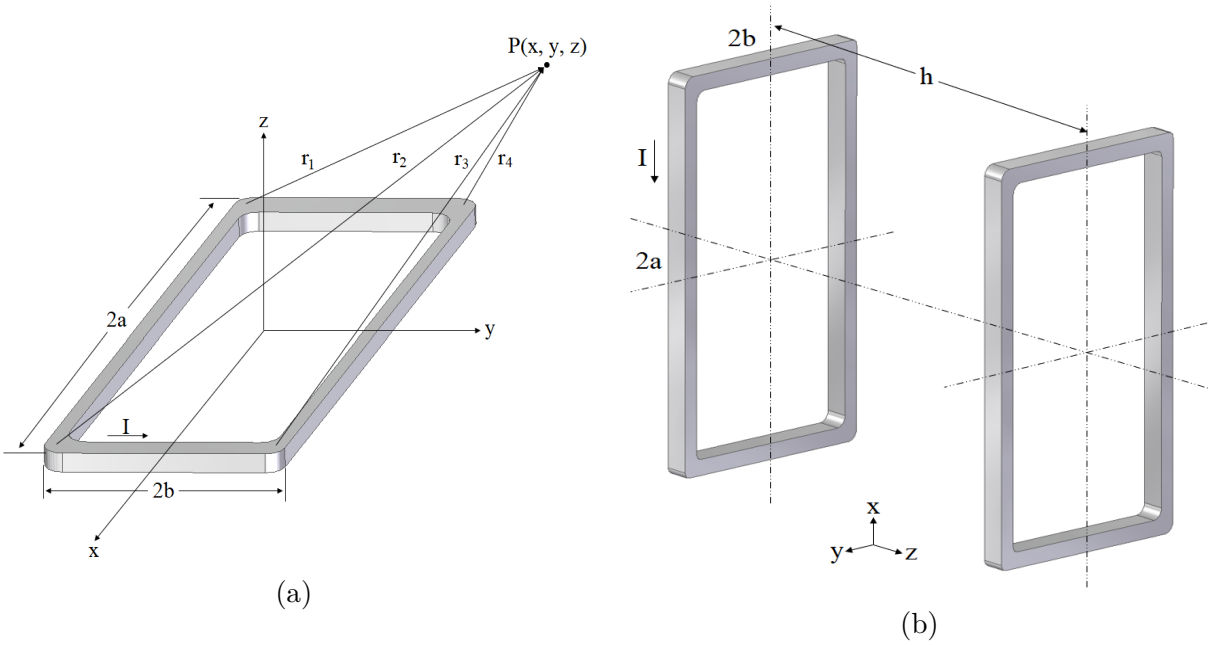

Figure 3.15: (a)Geometry of a single rectangular loop in the x-y plane. The magnetic flux density is assessed at point P(x, z), (b) rectangular Helmholtz coils configuration.

By substituting Eq. (3.12) and Eq. (3.13) into Eq. (3.11), the components of the magnetic flux density at point P(x, y, z) is written as

$$B_z = \frac{\mu_0 I}{4\pi} \sum_{\alpha=1}^{4} \left[\frac{(-1)^{\alpha} d_{\alpha}}{r_{\alpha}[r_{\alpha} + (-1)^{\alpha+1} C_{\alpha}]} - \frac{C_{\alpha}}{r_{\alpha}[r_{\alpha} + d_{\alpha}]} \right], \tag{3.14}$$

$$B_x = \frac{\mu_0 I}{4\pi} \sum_{\alpha=1}^{4} \frac{(-1)^{\alpha+1} z}{r_{\alpha}[r_{\alpha} + d_{\alpha}]}, \tag{3.15}$$

$$B_y = \frac{\mu_0 I}{4\pi} \sum_{\alpha=1}^{4} \frac{(-1)^{\alpha+1} z}{r_{\alpha}[r_{\alpha} + (-1)^{\alpha+1} C_{\alpha}]}, \tag{3.16}$$

where

$$C_1 = -C_4 = a + x \qquad d_1 = d_2 = y + b$$
$$C_2 = -C_3 = a - x \qquad d_3 = d_4 = y - b$$
$$r_1 = \sqrt{(a+x)^2 + (y+b)^2 + z^2}$$
$$r_2 = \sqrt{(a-x)^2 + (y+b)^2 + z^2}$$
$$r_3 = \sqrt{(a-x)^2 + (y-b)^2 + z^2}$$
$$r_4 = \sqrt{(a+x)^2 + (y-b)^2 + z^2}.$$

By employing these equations, we can easily determine the magnetic field produced by a set of Helmholtz coils at any specified location. Fig. 3.15b illustrates a pair of Helmholtz coils positioned in parallel along a shared axis (in this instance, the z-axis) on opposite sides of the test area, with a separation of h.

Simulations indicate that for a pair of square coils with a side length of a, the optimal separation distance between the coils is achieved when h is set to $0.55a$. In this configuration, the maximum region with a uniform magnetic field is obtained. Fig. 3.16 illustrates the simulation results for two coils with $a = 80$ cm, and each coil wound with 20 turns of wire. For example, in Fig. 3.16a, the distance between the coils is varied, showing the best separation distance for achieving the maximum region with a uniform magnetic field. In our case, we can get a uniform magnetic field in a region with length of around 20 cm.

The simulations show that in order to achieve a large volume with a uniform magnetic field, it is necessary to use coils with bigger dimensions. However, a significant limitation arises due to spatial constraints within the laboratory and the main chamber. These space limitations prevent us from scaling up the size of the coils. Consequently, the coils were optimized to attain the maximum achievable volume while maintaining a uniform magnetic field. Fig. 3.17 shows the 3D representation of the designed coils, along with

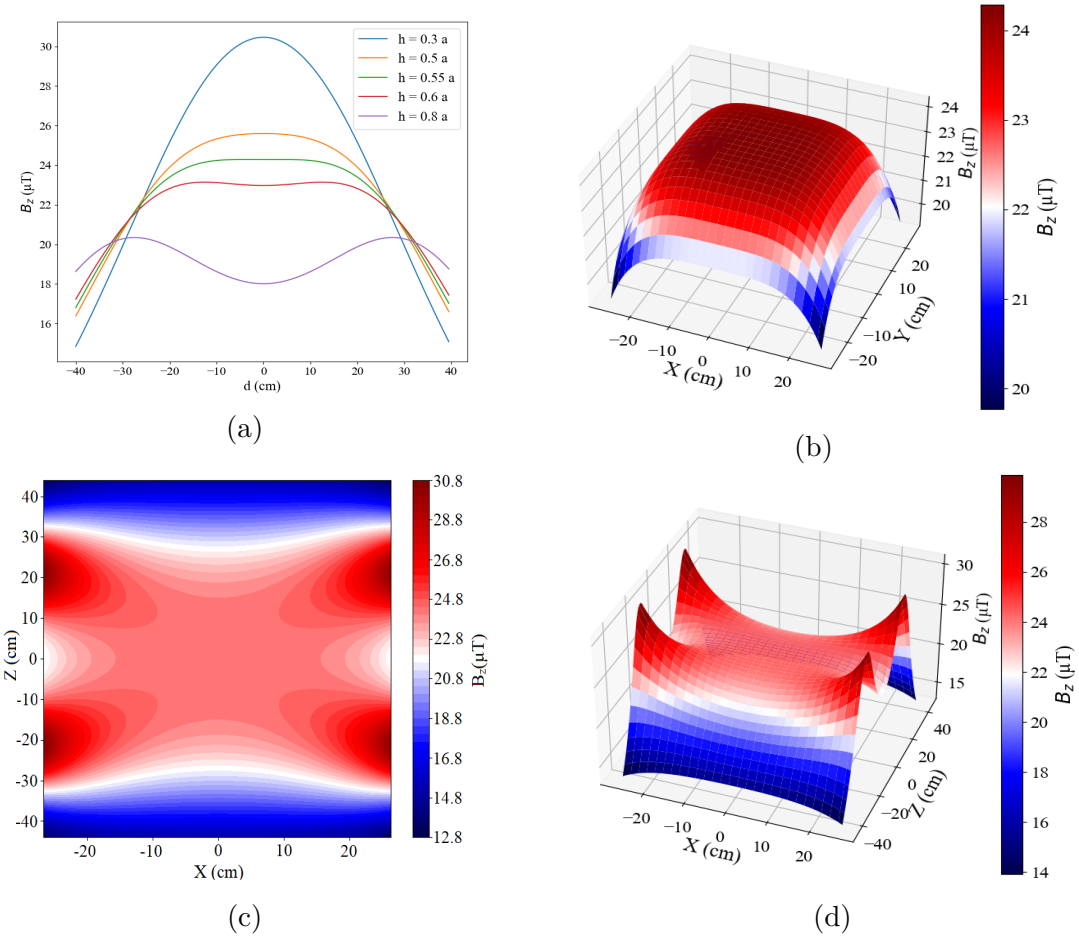

Figure 3.16: B_z for a pair of square Helmholtz coils with $I = 0.6$ A, $N = 20$, and $a = 80$ cm, (a) along the z axis, (b) as a 3D-surface in $x-y$ plane, (c) as a contour plot in $x-z$ plane, and (d)as a 3D-surface in $x-z$ plane.

their specific dimensions and the optimal distances between each coil pair.

3.6 Spin Dynamics in a Magnetic Field

In addition to the electron trajectory and the scattering process, the Earth's residual magnetic field can also influence the spin dynamics of the electrons during their propagation to the detector, which could reduce the measured asymmetry in the Mott detector and obscure the interpretation of the results. Therefore, careful consideration of residual magnetic fields is essential to ensure the integrity of spin-dependent measurements and to avoid misinterpretation of the observed asymmetry.

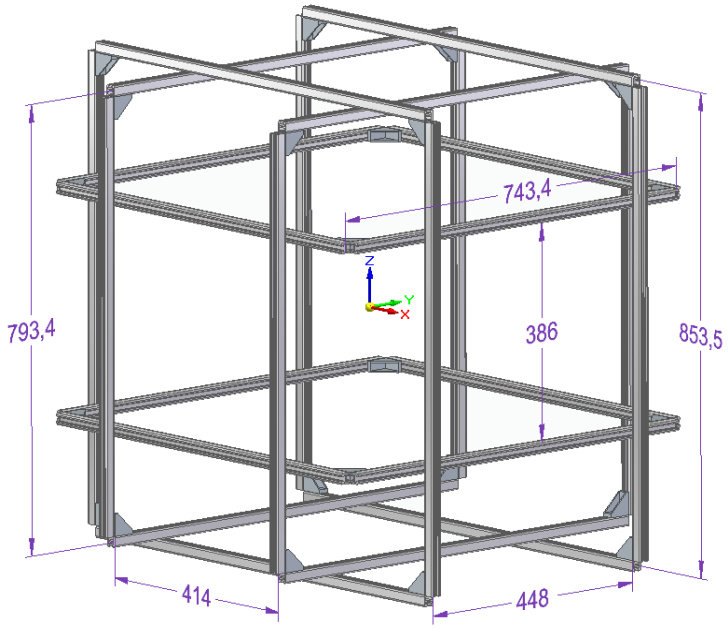

Figure 3.17: CAD view of the designed Helmholtz coils. All measurements are in millimeters, and the number of wire turns is 20 for each coil.

When an electron is in a magnetic field B, there is a direct interaction between the spin and the magnetic field. This interaction causes the electron's spin to precess around the direction of the magnetic field. The frequency of this precession, known as the Larmor frequency, is given by [28]

$$\omega_L = \frac{ge}{2m}B, \tag{3.17}$$

where $g \approx 2.0023$ is the electron g-factor, e is the elementary charge, B is the magnetic field strength, and m is the electron mass. In our case, the Earth's magnetic field is compensated, but in some positions, there is still a residual magnetic field less than $5\,\mu T$. Based on these calculations, the maximum Larmor frequency would be $\omega_L = 8.78 \times 10^5$ Hz. This corresponds to a full precession period of approximately $1.14\,\mu s$. Therefore, the time required for the spin to flip (rotate by 180°) would be approximately 570 ns. This timescale is on the same order as our experiment, which lasts approximately 350 ns, leading to the concern that the electron spin could undergo significant precession during the measurement. However, it is important to note that the electrons remain unpolarized

until they approach the Mott detector and spin polarization occurs within the final 5 to 10 ns before detection. Therefore, the residual magnetic field does not have sufficient time to induce a significant spin precession, and thus, it does not change the detected spin polarization.

3.7 Electron Transfer System

As it is mentioned, after the scattering process, The electrons are guided to the Mott detector by using an electron lens system. Based on our simulations, we have designed the lens system as illustrated in Fig. 3.18.

The lens system consists of three different groups. Lens Group 1 (LG1) collimates the electron beam and has a total length of 645 mm, Lens Group 2 (LG2) serves as a drift zone and has a total length of 2060 mm, and Lens Group 3 (LG3) focuses the beam onto the Mott detector, assisted by two additional lenses incorporated within the Mott detector and the total length of this group is 330 mm. Fig. 3.19 shows the results of simulations for a passing electron beam through the lens system using SIMION software.

The labeling convention follows [38, 43], with LG1, LG2, and LG3 denoting the lens groups and En representing the nth electrode in the system. The lenses in the Mott detector are referred to as ME1 and ME2. Two deflectors, LG1E3 and LG3E3, are included in the setup. Each deflector is segmented into four sectors with independently adjustable voltages. This design permits fine-tuning of the beam position in the electron transfer system.

For accurate timing measurements in the experiment, it is important to determine the Time of Flight of electrons in the electron transfer system. Simulations using SIMION software indicate that by assuming the scattered electron has a Gaussian energy distribution with a Full Width at Half Maximum (FWHM) of 1 eV and a central energy of 10 eV, and that its temporal distribution is also Gaussian with an FWHM of 30 ns, the

TOF of electrons through the electron transfer system is approximately 290 ns. Therefore the total TOF of electrons from the cathode to the Mott detector is around 340 ns.

More detailed information about the performance of the electron lens system can be found in two master theses [38, 43]. However, some modifications have been implemented in this work to enhance its functionality, as will be discussed in detail in Chapter 4.

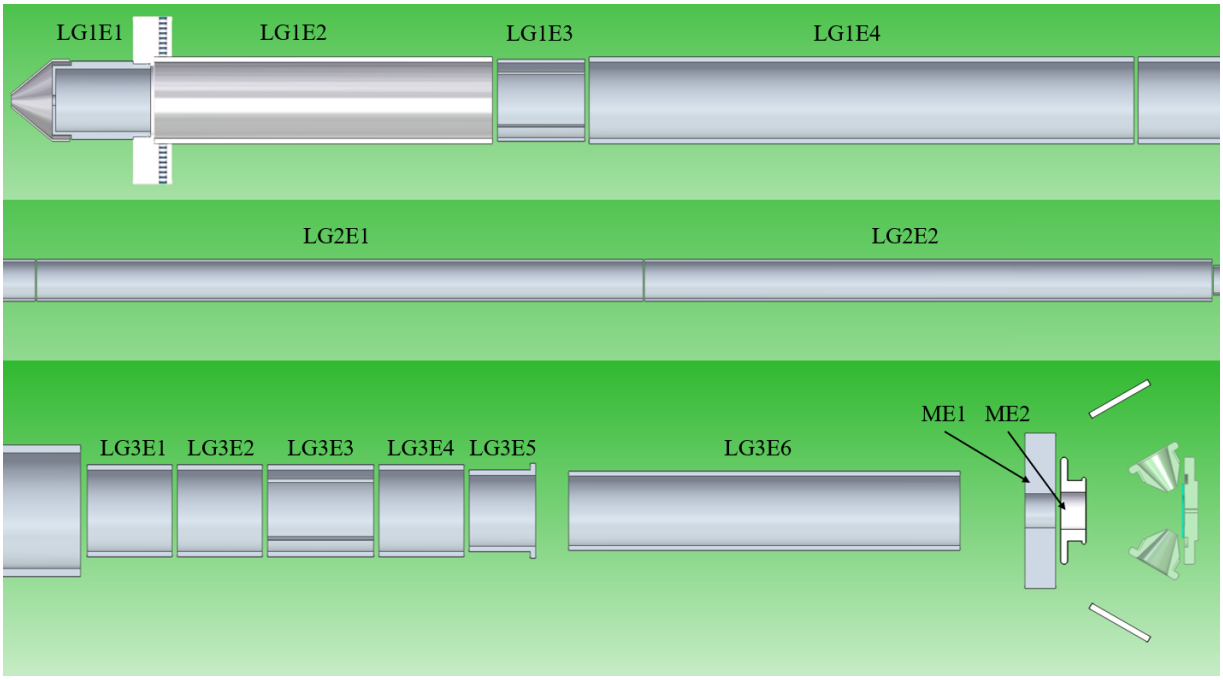

Figure 3.18: The CAD view of the designed electron transfer system and the Mott detector. It includes three lens groups and 2 lenses belongs to the Mott detector. The scales for each group are different due to variations in their sizes.

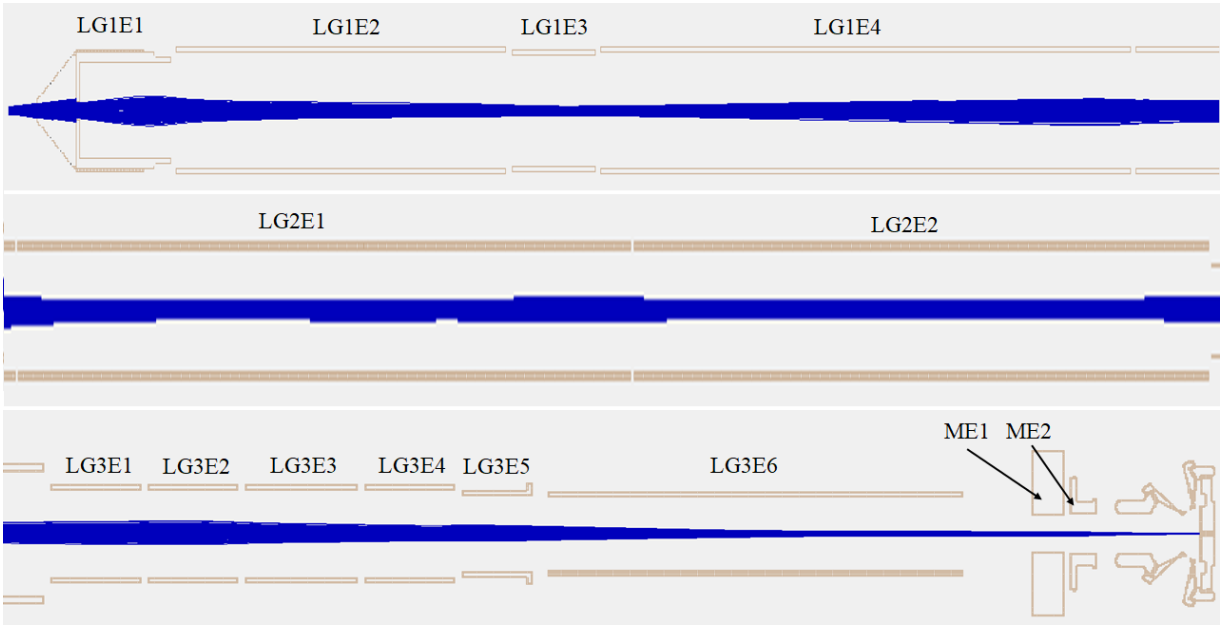

Figure 3.19: The simulation result for the trajectory of the electron beam through the electron transfer system.

4. Experimental Setup

4.1 Electron Gun Characterization

One of the most crucial components in the experiment is the electron gun. To ensure its performance, a comprehensive investigation must be undertaken, particularly concerning its output in terms of energy and the size of the electron beam in the interaction region, where the electrons interact with the sodium atoms. In the following sections, we will discuss how these assessments were conducted, as well as the results of every test.

4.1.1 UV Light Generation

As depicted in Fig. 3.1, the initial step in electron generation is the generation of UV light to illuminate the cathode of the electron gun in order to generate photoelectrons. This was achieved by utilizing 20% of the output of a ns-pulsed green laser in conjunction with a frequency doubling in BBO crystal.

The experimental setup is shown in Fig. 4.1. Following the beam splitter, the beam passes through a half-wave plate, which allows us to rotate the polarization of the light. This adjustment ensures the linear polarization is properly aligned with the optical axis of the BBO crystal, optimizing the phase matching condition, which is necessary for efficient UV light generation. The beam is then directed through two lenses that form a Galilean beam expander, which focuses the beam to reduce the green laser spot size. After this, the beam is incident on a BBO crystal and generates UV light. To separate the generated UV light from the remaining green light, two harmonic separator mirrors are employed. Finally, a photodiode is positioned behind the second separator to serve as a time reference origin for the entire experiment.

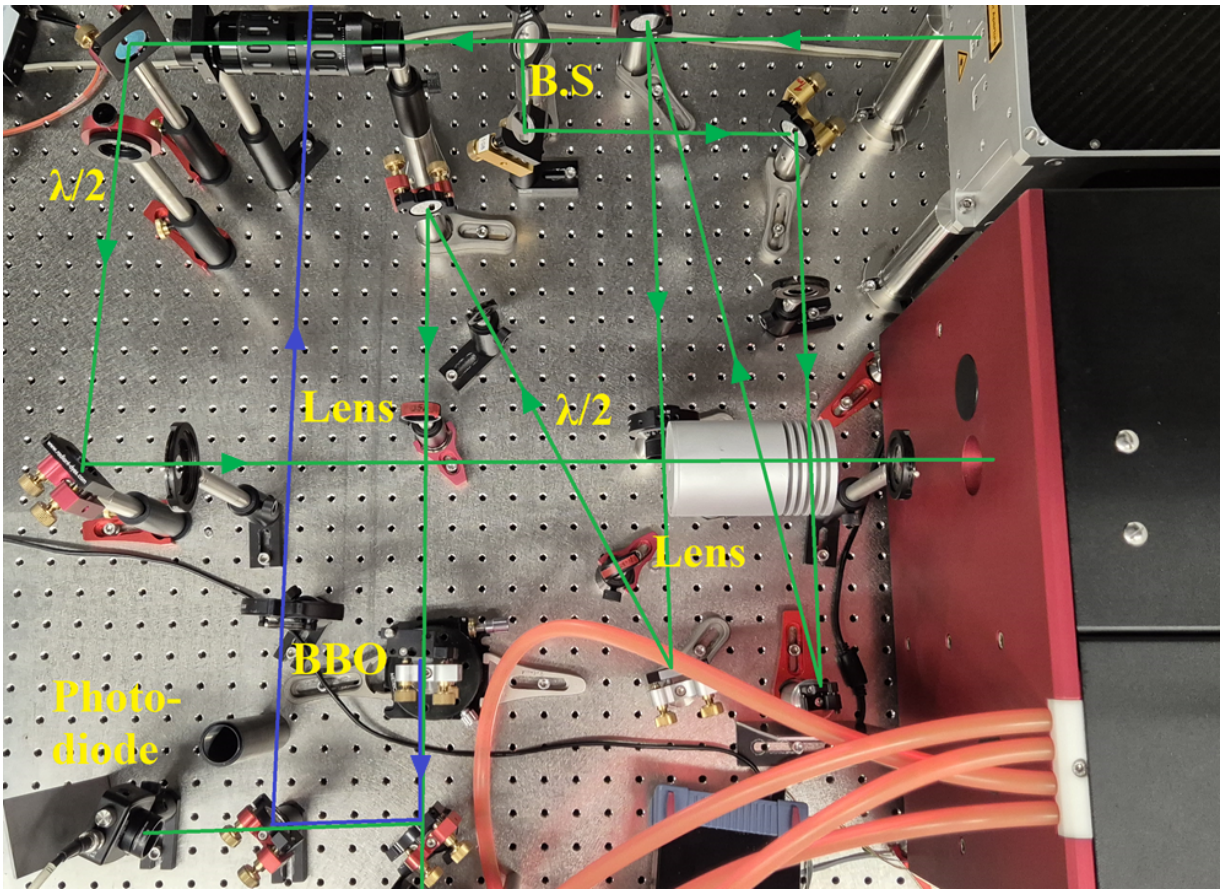

Figure 4.1: Experimental setup for generating UV light and pumping the dye laser. The beam splitter reflects 20% of the incoming green light for UV generation, while the transmitted light is used for pumping the dye laser.

After that, the output power of the generated UV light was measured. With an input green laser having an average power of 2 W, the generated UV power was 25 mW, indicating an efficiency of approximately 1.25%. This efficiency is very low, primarily because the spot size of the green laser was kept large, around 0.8 mm, to prevent damage to the BBO crystal. Nevertheless, the generated power is more than sufficient for electron generation at the cathode. Increasing UV power leads to higher electron generation, which can create significant space charge effects. As will be shown later, this space charge significantly impacts the energy distribution and trajectory of the electron beam. Additionally, the pulse duration of the UV light was measured and was approximately 25 ns, while the pulse duration of the green laser was around 45 ns.

4.1.2 Silver Thickness Optimization

In the process of assembling the electron gun, a half-sphere sapphire is fixed to its holder by using conductive silver-filled epoxy. Subsequently, we attempted to coat a silver layer on its surface. However, due to the spherical shape of the sapphire, achieving a uniform coating over the entire surface was challenging, particularly on the lower part, which may end up with a thinner coating or even no coating at all. This uneven coating can result in poor electrical conductivity between the silver coated layer on top of the sapphire and its holder, which is connected to the power supply that maintains the cathode at $-10\,\mathrm{V}$. To solve this problem, the entire surface was initially coated with a thicker layer of silver, approximately 50 nm, to ensure complete coverage of the half-sphere. Following this, the silver layer on the top part of the sapphire was removed. Subsequently, the surface recoated with the required thin layer of silver. This method ensures reliable electrical connections, which are crucial for the operation of the electron gun. Fig. 4.2 shows the coated cathode with its holder.

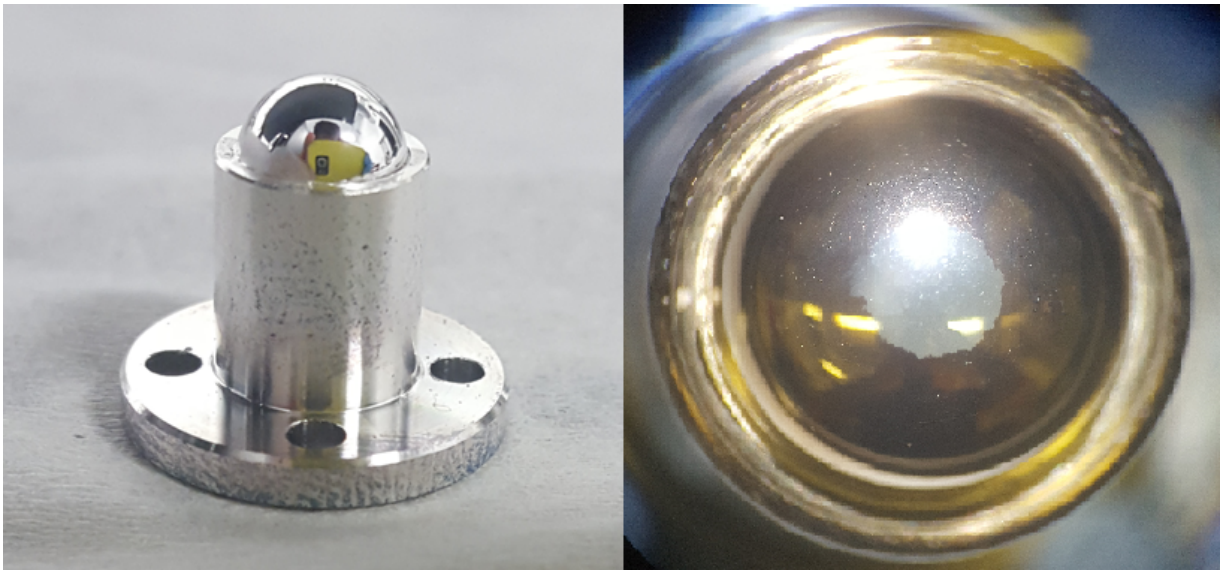

Figure 4.2: Left: The cathode with its holder, coated with 50 nm of silver. Right: The top part of the cathode, coated with 10 nm silver.

To optimize the thickness of the silver layer and compare it with the simulations in

Section 3.2.1, we needed to measure the generated current of the cathode for different thicknesses. However, due to the spherical shape of the substrate, we discovered that the actual thickness of the silver layer differs from the value indicated by the sputter coating machine. Therefore, accurate measurement of the silver thickness is essential for a reliable comparison with the simulations.

To achieve this, we used green light and measured its transmission through the substrate and coated layer, and compared the results with the simulation outcomes obtained using COMSOL software. The difference between the measured thickness and the values reported by the sputter coating machine is shown in Table 4.1. The results indicate significant discrepancies between the measured and reported values. However, by repeating the process, we found the measurements to be consistent. This allows us to calibrate the coating process, ensuring that the desired thickness is achieved accurately.

In the next step, we measured the current of generated photoelectron. To ensure that none of the generated photoelectrons collided with the walls of the electron gun lenses, we used only the first and second lenses of the electron gun and measured the current for different silver thicknesses. Table 4.1 presents the measurement results for different thicknesses, indicating that the optimal thickness of the silver layer for generating maximum photoelectrons is around 15 nm. This is slightly different from the simulation results in Section 3.2.1, which suggested an optimal thickness of around 9 nm.

One reason for this discrepancy might be that the simulation only considered the absorption and inelastic mean free path of the electrons, without accounting for the effect of the pulsed beam. Additionally, the silver distribution could also impact the results, which was not considered in the simulation. Nevertheless, through these measurements, we determined that the optimal thickness of the silver layer for generating maximum photoelectrons is approximately 15 nm.

Figure 4.3 shows the CAD view of the measuring system and the simulation results of the electron trajectories using SIMION software. The voltages set for each lens are also

indicated in this figure. To measure the current, we used a metallic plate set at +6 V to collect all the electrons. Additionally, a grounded copper mesh was placed between this metallic plate and the electron gun to prevent any electric field penetration and avoid altering the trajectory of the electron beam.

Reported thickness by sputter coating machine (nm)	**Measured transmission of green light (%)**	**Thickness based on transmission (nm)**	**Measured electron current (nA)**
20.23	≈ 2.4	≈ 50	15
16.02	≈ 6	≈ 40	40
11.99	≈ 12.5	≈ 30	52
7.95	≈ 27	≈ 20	79
6.20	≈ 44	≈ 15	87
4.45	≈ 44	≈ 15	91
3.18	≈ 51	≈ 12	57

Table 4.1: Comparison of different thicknesses and generated electron current by the silver layer. Additionally, the difference between measured thickness and thickness reported by the sputter coating machine are presented.

4.1.3 Output Current of the Electron Gun and the Effect of the Earth's Magnetic Field

After optimizing the thickness of the silver layer, the entire electron gun was assembled, as shown in Fig. 4.4. All electrical connections were made, and each lens was supplied with the desired voltage. The detector was then placed directly in front of the electron gun, and the output current of the electron gun was measured. Additionally, the beam profile of the electron beam was examined at different distances from the electron gun. However, the measured current and beam profiles differed from the simulated ones.

To investigate this discrepancy, we measured the Earth's magnetic field near the electron gun, finding it to be around $60\,\mu$T. Since, the energy of the generated electrons

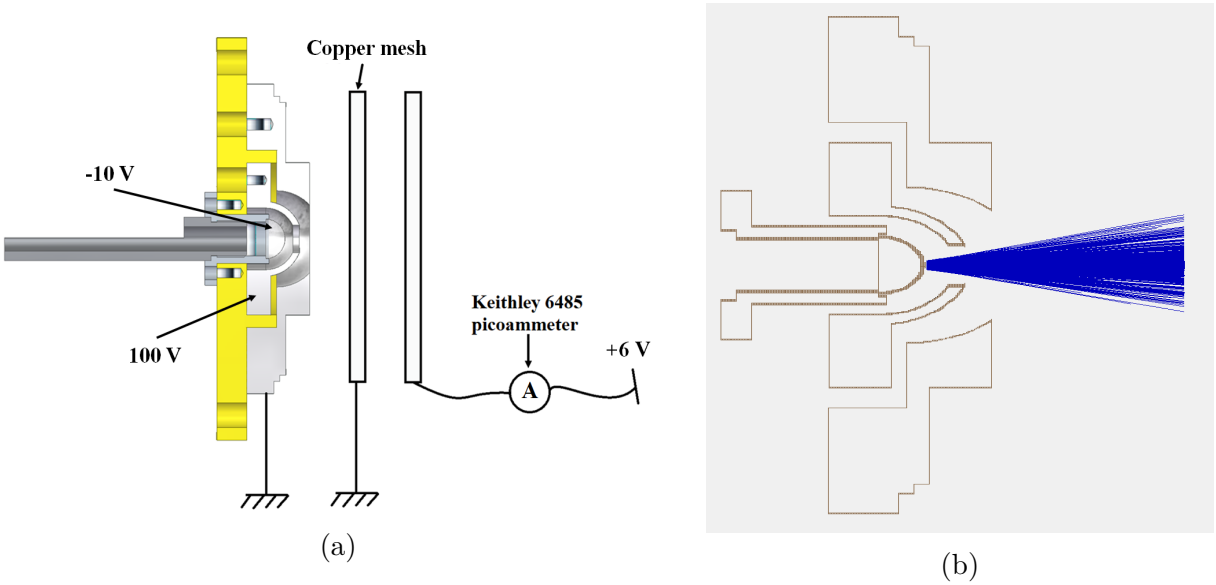

(a) (b)

Figure 4.3: (a)The CAD view of measurement setup. The cathode is at −10 V and the first and second lenses are at 100 V and 0 V respectively. To verify the absence of offset current caused by UV light, the electrode voltages were turned off and the measured current was confirmed to be zero. (b) The trajectories of the generated electrons, which are displayed as blue lines.

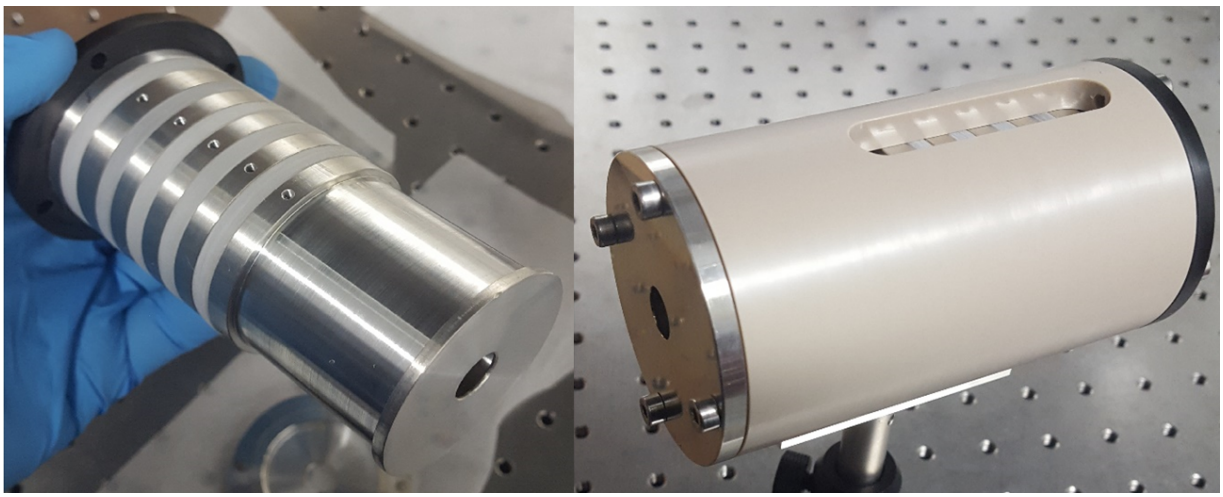

Figure 4.4: Left: Lenses within the electron gun, Right: The complete assembly.

is very low, they can be affected by this magnetic field. To avoid this, we first covered the entire vacuum chamber with μ-metal, to reduce the Earth's magnetic field inside the chamber and it reached to approximately 15 μT. Subsequently, the output current of the electron gun was measured, and we observed an increase in the current.

However, achieving zero magnetic field only by using μ-metal is not feasible, and having

zero magnetic field in the interaction region is crucial for the scattering process. Then, as described in Section 3.5, an array of three square Helmholtz coil pairs was placed around the vacuum chamber, and the output current of the electron gun was remeasured with the Earth's magnetic field compensation system. Table 4.2 shows the effect of the Earth's magnetic field compensation on the output current of electron gun. In these measurements, the Z and X axes are perpendicular to the path of the electron beam, while the Y axis aligns with the direction of the electron beam path.

By applying current to each pair of Helmholtz coils, we were able to compensate for the Earth's magnetic field. For the Z-axis, we achieved a region of uniform magnetic field over a length of 12 cm, where $B_z \approx 0 \pm 1\,\mu$T. For the X and Y axes, the uniform magnetic field regions were 15 cm and 5 cm, respectively. The reason for the shorter region with uniform magnetic field along the Y-axis is due to the non-uniform magnetic field in the laboratory along this axis, which limited our ability to achieve better compensation. This limitation is not problematic because the magnetic field component along the electron beam path (Y-axis) does not significantly affect the electron beam's trajectory, as confirmed by our measurements.

4.1.4 Energy Distribution of the Output Electron Beam

After the optimization of the output current of the electron gun, the next step was measuring the energy distribution of the electron beam. As discussed in Section 2.1.1, the entanglement between electrons and sodium atoms during scattering highly depends on the energy of the incoming electrons. Therefore, achieving an electron energy of precisely 10 eV is critical and performing this measurement accurately is a key aspect of the experiment.

To perform this measurement, a detector was constructed that is capable of determining the energy distribution of the electron beam. The detector, depicted in Fig 4.5 and consists of two copper meshes and an aluminum plate arranged sequentially. This arrangement is known as a retarding-field analyzer.

Z-component of magnetic field compensation	**X-component of magnetic field compensation**	**Y-component of magnetic field compensation**	**Current (nA)**
On	On	On	11.9
On	On	Off	11.9
On	Off	On	10.9
On	Off	Off	10.6
Off	On	On	2.7
Off	On	Off	2.7
Off	Off	On	2.1
Off	Off	Off	1.4

Table 4.2: Effect of each component of earth's magnetic field compensation system on the output current of electron gun.

The first copper mesh is set at ground potential, ensuring that the electric field created by the voltages on the aluminum plate and the second copper mesh does not affect the incoming electrons from the electron gun. This configuration ensures that the measurement process does not influence the electron beam's trajectory or energy. The second copper mesh is placed behind the first one and is connected to a variable negative power supply. This mesh creates a retarding field for the electrons.

The aluminum plate, located behind the second mesh, is maintained at a positive voltage and is connected in series with an ammeter. The positive voltage on the plate ensures that all electrons passing through both meshes are absorbed and their current is measured.

To measure the electron energy, the detector is aligned with the electron beam. For instance, if we are measuring electrons with an energy of 10 eV, we vary the voltage on the second mesh from -5 V to -15 V. Electrons with energy less than the applied voltage (e.g., -10 V) are repelled by the second mesh and cannot reach the aluminum plate and only electrons with energy higher than the retarding voltage can pass through and be

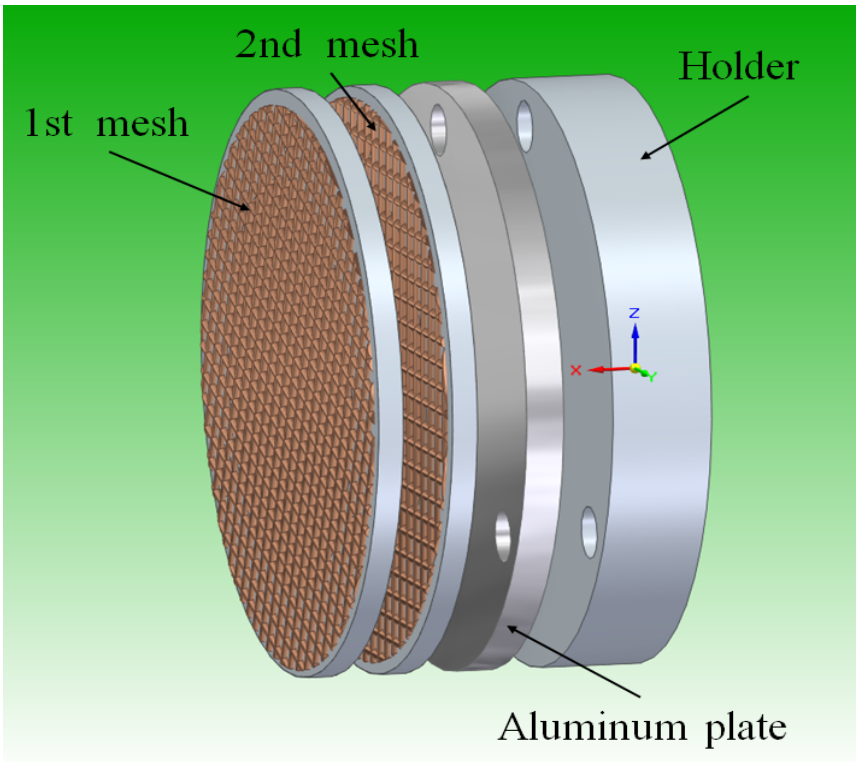

Figure 4.5: The CAD view of the home-made energy detector.

collected by the aluminum plate.

By measuring the current at the aluminum plate for different voltages applied to the second mesh, we obtain a current-voltage (I-V) curve. The X-axis of this curve represents the applied voltage, while the Y-axis represents the measured current. By differentiating this I-V curve, we can determine the energy distribution of the electron beam and the peak in the derivative corresponds to the central energy of the electrons.

Fig. 4.6 shows the measured energy distribution of the electron beam from the electron gun for different UV light powers. As it is expected, the experimental results demonstrate that generating an excessive number of electrons negatively impacts the energy distribution of the outgoing beam. When the average laser power of the UV light is around 1 mW, the FWHM of the energy distribution is approximately 1 eV. However, as the power increases, the energy distribution broadens, which is not desired for the final experiment.

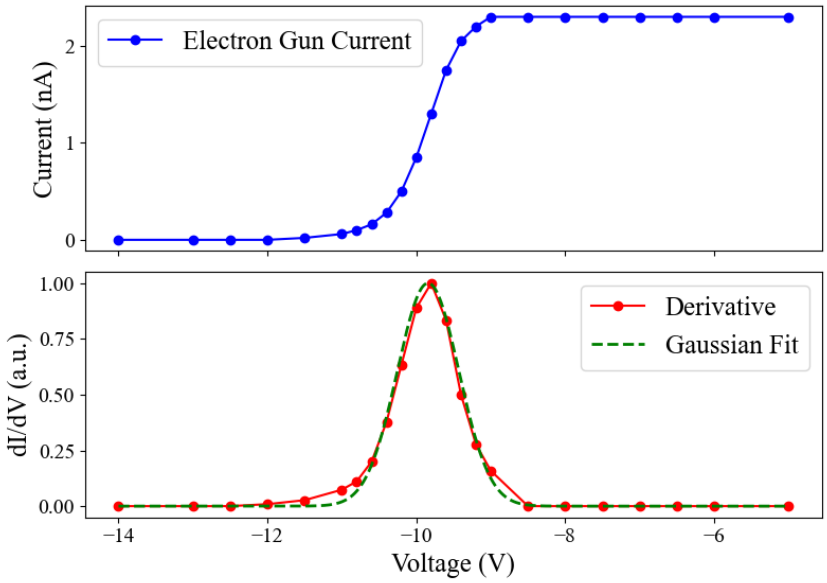

(a)

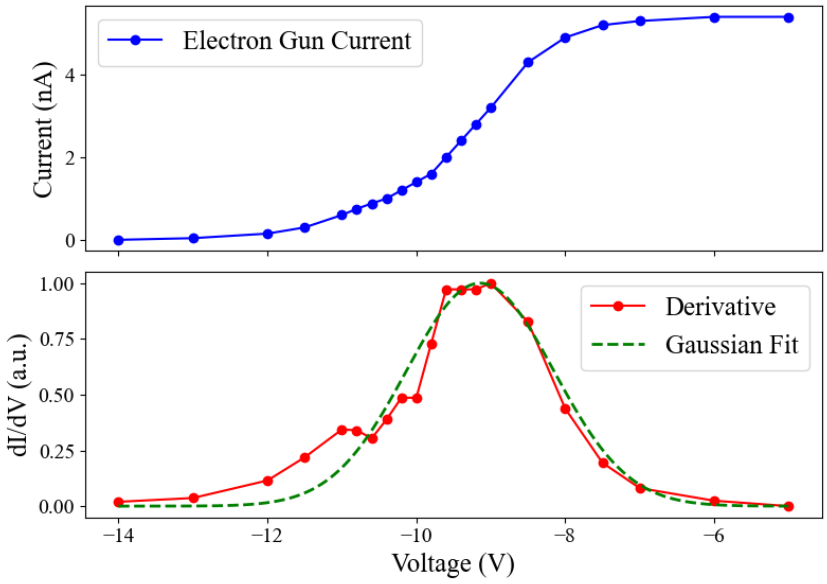

(b)

Figure 4.6: Effect of UV beam power on the energy distribution of the electron beam. For a) the laser power is 1 mW and the FWHM is around 1 eV, and for b) the laser power is 18 mW and the FWHM is around 2.4 eV.

4.1.5 Beam Profile of Electron Beam

Since the electron beam generated by the electron gun will interact with sodium atoms, and the overlap between these electrons and the sodium atoms is crucial for the scattering process, determining the electron beam size at the interaction region is essential for maximizing the number of scattered electrons.

A common method for visualizing the profile of an electron beam, especially when dealing with low electron currents in the nanoampere range, involves using a combination of a Microchannel Plate (MCP) and a phosphor screen. However, in our case, the transmitted UV light from the cathode passes through and exits the system. When these UV photons strike the MCP, they can generate photoelectrons, which then undergo the same electron multiplication process as the electrons from the beam. This leads to background noise and distorts the detected beam profile.

Therefore, we needed an alternative method to accurately monitor the beam profile. To achieve this, we designed a detector, as shown in Fig. 4.7. This detector operates similarly to the one we previously built for measuring the energy distribution of the electron beam, but with a key modification. In this setup, we used only one metal plate with a small aperture positioned in front of the detection plate.

The aperture allows only a specific portion of the electron beam to pass through to the detection plate, where the current is measured. By scanning the aperture across the beam in the X and Z directions, we can map out the beam profile. This method lets us to obtain a detailed spatial profile of the electron beam by measuring the current at different positions.

The resolution of the beam profile in this detection method is determined by the size of the aperture. Considering the limitations of our ammeter in detecting current, we have selected an aperture size of 1×1 mm, which yields a beam profile resolution of 1×1 mm and is sufficient for our experiment.

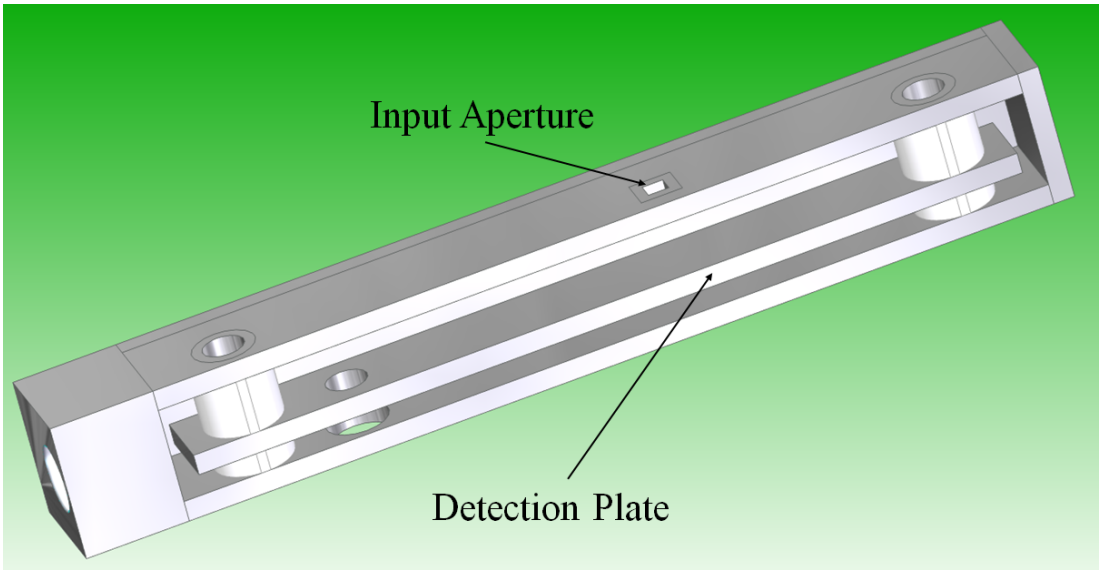

Figure 4.7: The CAD view of the built detector for measuring the electron beam profile.

After constructing the detector, it was integrated into the experimental setup to measure the electron beam profile under various voltage configurations of the electrostatic lenses within the electron gun. The measurements revealed a slight discrepancy between the observed beam profile size and the simulated results at the focus point and the position of the focus. However, by adjusting the voltage of the electrode U_5, we were able to shift the position of the focus. Fig. 4.8 shows the measured electron beam profile at a distance of 3.5 cm from the output of the electron gun, which corresponds to the interaction region for the scattering process. The data indicate that the beam diameter at this position is around 2 mm.

One potential reason for the observed discrepancy between the experimental results and the simulations could be a mismatch in the initial beam size. As shown in Fig. 3.5, the position of the focus of the electron beam is sensitive to the UV beam size, which may explain the deviation. Another contributing factor could be the fact that space charge effects were not considered in the simulations. In reality, space charge effects can influence the beam size and the focus position. These effects were ignored in the simulations, but in practice, they could cause the beam to expand and shift the focal point.

Additionally, the measurements indicate that if the UV light beam does not strike precisely in the center of the cathode, the resulting electron beam does not emerge centrally from the gun. This misalignment is evident in Fig. 4.8, where the beam is off-center and shows the importance of accurate UV light alignment. So, proper alignment of UV light is crucial for optimizing the overlap between the electron beam and the sodium atoms in the scattering process.

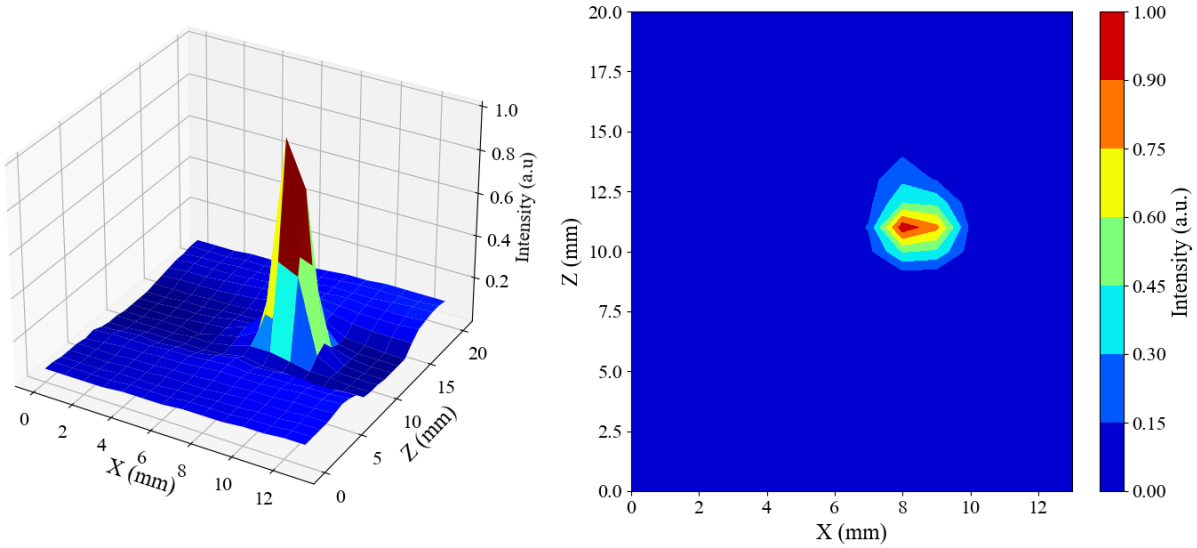

Figure 4.8: 3D and contour plots of the electron beam profile at 3.5 cm from the electron gun output. The electrostatic lens voltages are set according to the values in Table 3.2, with U_5 adjusted to 380 V.

4.2 Oven

After optimizing and testing the output of the electron gun, the next critical step in our experimental setup is the construction of an oven that generates a well-collimated beam of sodium atoms for the scattering process. The oven was built according to the specifications outlined in Section 3.3 and it is shown in Fig. 4.9.

In this prototype, two locations were designated for temperature sensors to assess the feasibility of achieving a controlled temperature gradient within the oven. By

independently adjusting the current supplied to each heater, the measurements confirmed that the desired temperature differential could be reliably established using this dual-heating method. For instance, to achieve a temperature of 300 °C at the lower part of the oven and 330 °C at the top, a current of 1.4 A was applied to the coil heater and 1.2 A to the ceramic heater. Repeated measurements with identical current settings for the heaters demonstrated consistent results, indicating stable and reproducible control over the temperature distribution. This approach is crucial as the top sensor will be removed in the final experimental setup because of the proximity of this sensor to the interaction region and the sensor might be charge up with the electrons and creates unwanted electric fields that could affect the scattering process.

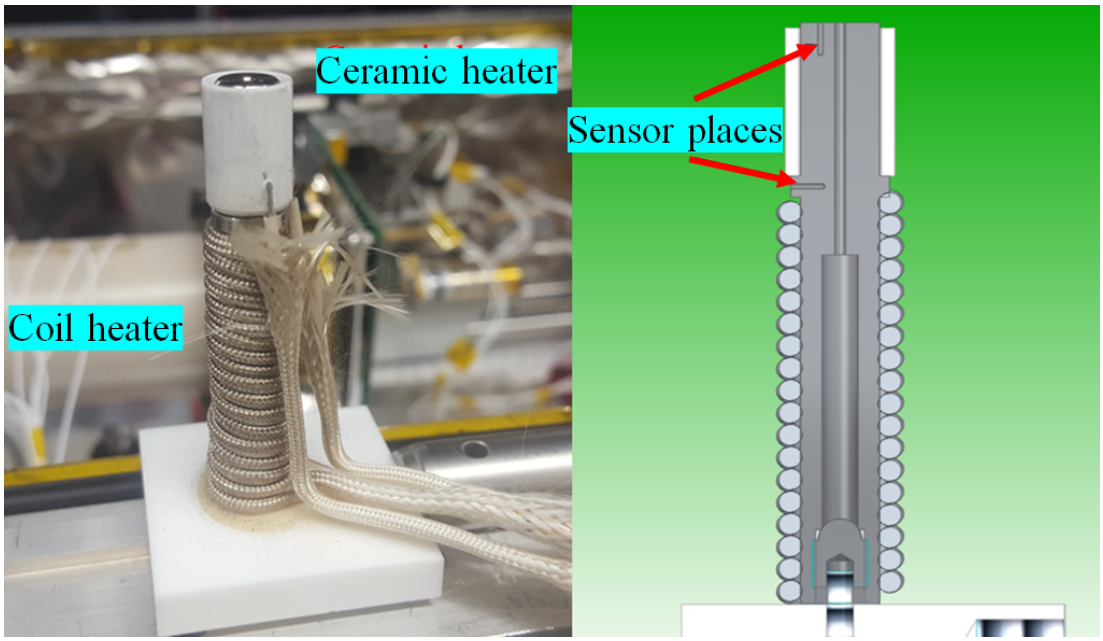

Figure 4.9: First prototype of the oven without its heating shield.

To fill the oven with sodium, it is essential to perform the process in an environment with minimal humidity, as sodium reacts rapidly with water vapor to form sodium hydroxide (NaOH). The presence of sodium hydroxide changes the chemical properties of the sodium and could significantly affect the results of the experiment by introducing unwanted contaminants or altering the scattering dynamics. To prevent such reactions,

the oven was filled with sodium in a glove box purged with dry nitrogen gas to maintain an inert atmosphere.

After filling the oven with sodium, additional precautions were taken to prevent any reaction with atmospheric moisture during transportation and final alignment of the experimental setup. The top section of the oven was filled with benzine (petroleum ether) to create a protective barrier against air exposure. Benzine was selected because it does not react with sodium and has a low boiling point of approximately 130 °C, ensuring that it would evaporate completely when the oven reaches its operational temperature of around 310 °C. This rapid evaporation prevents any interference with the sodium vapor, preserving the purity of the sodium beam for the experiment.

To measure the output of the oven and compare the actual values with the design specifications, we first tried to determine the amount of sodium emitted by the oven and its spatial distribution above the oven's output. For this purpose, a glass plate was placed above the oven's exit to collect the sodium atoms. The plan was to use an interferometric microscope to measure the thickness and distribution of the deposited sodium layer.

However, when the vacuum chamber was vented, the sodium atoms deposited on the glass reacted immediately with water vapor and this reaction changed the integrity of the sodium layer and prevented further measurements. As an alternative, we used a laser with its wavelength tuned to the D_1 line of the sodium atoms to visualize the distribution of the sodium beam. This approach allowed us to observe the fluorescence of the sodium atoms and qualitatively assess the beam's profile. While this method did not provide a direct measurement of the oven's output, it confirmed that the sodium beam was well collimated and closely matched the expected distribution predicted by our simulations.

Fig. 4.10 shows the experimental setup and results for measuring the sodium beam size. The laser beam used in this experiment has a diameter of approximately 12 mm, which allows us to visualize the cross sectional profile of the sodium beam. The fluorescence image confirms that the beam is well collimated, with a measured diameter of about

2 mm, which is in good agreement with the simulated predictions.

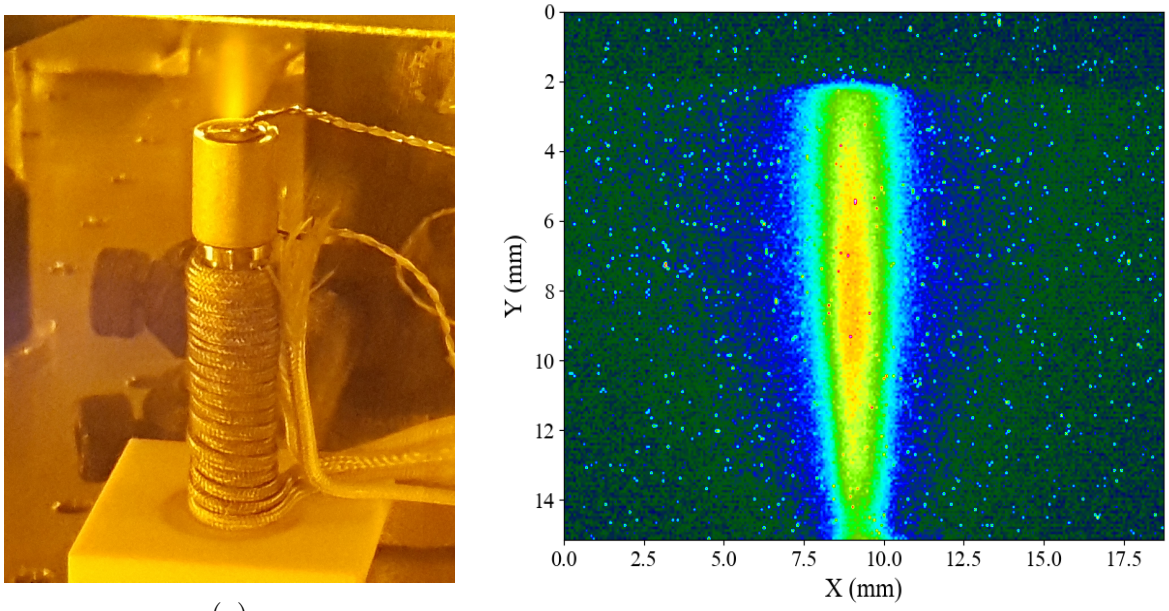

(a) (b)

Figure 4.10: a) A photograph of the oven with the sodium beam fluorescence. b) The processed contour plot of the sodium beam profile, illustrating the intensity distribution. This plot highlights the uniformity and collimation of the beam.

During the testing of the oven, we discovered that the electric current passing through both heaters of the oven generates a magnetic field of approximately 2 μT near the interaction region. This magnetic field could potentially affect the electron-sodium scattering process, leading to inaccuracies in our experimental results.

To avoid this effect, we took advantage of the temporal separation between the laser pulses. Our laser system operates at a repetition rate of 10 kHz, with a time interval of 100 μs between each pulse. Also, based on simulations the total time of flight of electrons from the cathode to the interaction region and then to the Mott detector is less than 500 ns. Therefore, to ensure that the magnetic field does not interfere with the experiment, we implemented an electronic circuit for the oven to switch off the current of the heaters 5 μs before and 5 μs after each laser pulse. This timing effectively eliminates any magnetic field influence during the critical period when the electrons are generated, scattered, and

detected, thereby preserving the integrity of the scattering measurements.

The designed circuit that modulates the DC current supplied to the oven's heaters is shown in Fig. 4.11a. The circuit is controlled by a TTL signal generated by a signal generator, which is synchronized with the laser pulses. This synchronization ensures that the heater currents are switched off at the precise moment. Fig. 4.11b shows the timing diagram captured from an oscilloscope, demonstrating the synchronization between the laser pulses and the heater current modulation. The diagram clearly illustrates the performance of the circuit in switching the heater current on and off at precise intervals, effectively preventing any interference from the oven current during the experiment.

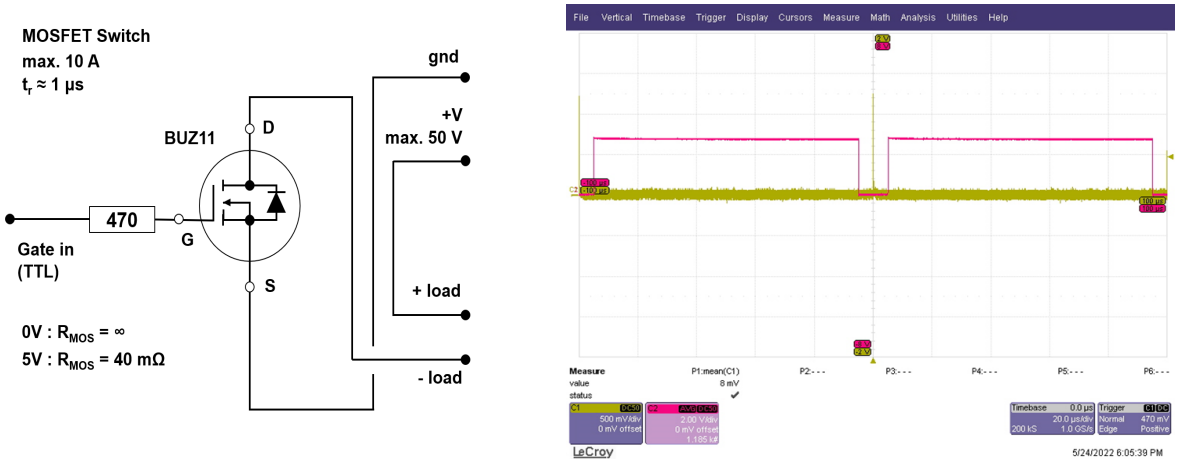

(a) (b)

Figure 4.11: a) The designed circuit for controlling the timing of the oven current to avoid magnetic interference during measurements. b) The measured timing diagram showing the synchronization between the laser pulse signal (yellow) and the output current of the circuit (red).

4.3 Scattering Process and Electron Transfer System

With generating a well-collimated sodium beam and an electron beam with an energy of 10 eV, the next step in the experiment is to investigate the scattering process. This involves analyzing how the electrons scatter off the sodium atoms and subsequently transferring the scattered electrons to the Mott detector, which is positioned 3 m away from the interaction

region.

Initially, the experimental setup was placed inside a vacuum chamber with sufficient space to accommodate the electron gun and a time-of-flight (TOF) detector, as illustrated in Fig. 4.12. To minimize the influence of external electric fields on the scattering process, an electric shield was positioned around the setup. This precaution was necessary because various wires and electrostatic lenses in close proximity could potentially interfere with the scattering results.

The TOF detector used in this setup consists of a microchannel plate (MCP) coupled with four electrostatic lenses. By measuring the time taken by the electrons to reach the detector, we can determine their initial energy. For elastic scattering events, the electron energy should remain equal to its initial value of 10 eV.

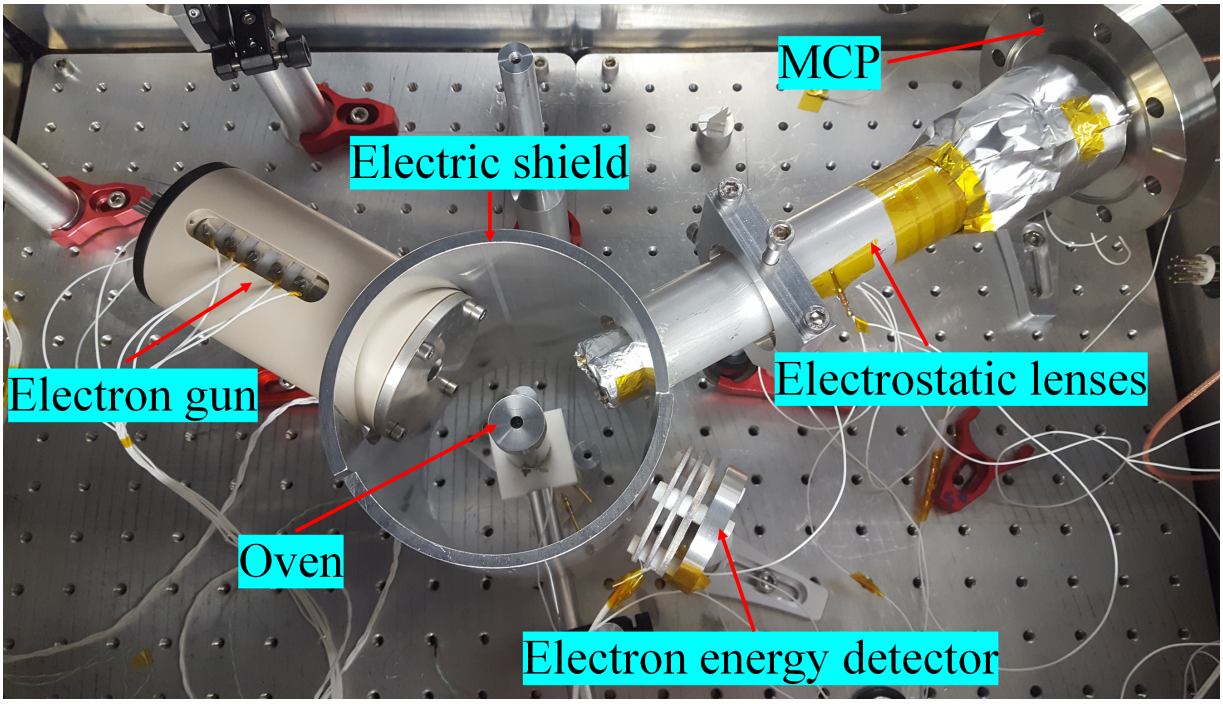

Figure 4.12: First setup for investigating the scattering process.

As an initial measurement, we recorded the number of electrons reaching the detector over various time intervals after the trigger and accumulated data for 20 seconds. A typical signal is shown in Fig. 4.13. From these measurements, we identified three distinct types

of electrons reaching the detector, which compromised the accuracy of our results. The first group consisted of electrons scattered from the sodium atoms, which are the primary focus of our investigation. These electrons are expected to exhibit specific energy and timing characteristics corresponding to elastic scattering, where they retain their initial energy of 10 eV.

The second group consists of electrons that do not interact with the sodium atoms but pass through the sodium atoms and collide with the walls of the electric shield. Some of these electrons manage to scatter off the shield walls and reach the detector. These electrons typically arrive later than the desired scattered electrons from sodium due to their longer path and lower energy. To reduce this interference, we replaced the electric shield located in front of the electron gun with a copper mesh. This modification allowed for greater control over stray electrons by reducing the number that could scatter toward the detector. Additionally, increasing the distance of the mesh from the electron gun increased the time separation between these unwanted electrons and the primary group, making it easier to distinguish between them in the measurements.

The third group consists of electrons that scattered off the top surface of the oven. These electrons are problematic because they reach the detector at nearly the same time as the electrons scattered from the sodium atoms, and it is not possible to distinguish them from the primary group. The presence of these electrons is particularly problematic due to low scattering cross section of sodium atoms, resulting in a small number of desired scattered electrons. Consequently, even a small number of additional electrons from the oven surface can significantly change the measurement results.

These oven-scattered electrons result from electrons that deviate from their ideal trajectory and strike the oven surface, even though the electron beam is primarily directed toward the interaction region. To avoid this issue, our initial solution was to decrease the height of the oven so that it would be further away from the interaction region. However, the drawback of this adjustment is that increasing the distance from the interaction region

reduces the intensity of the atomic beam, resulting in fewer scattered electrons.

To solve this problem while keeping the oven exit close to the interaction region, we placed an aperture between the electron gun and the oven. This aperture allows only well-collimated electrons to pass through and reach the interaction region, effectively blocking stray electrons from deviating toward the oven surface. We carefully optimized the aperture size to maximize the number of well-collimated electrons while minimizing stray electrons. We found that the optimal diameter for the aperture is approximately 7 mm, positioned 2.8 mm from the electron gun.

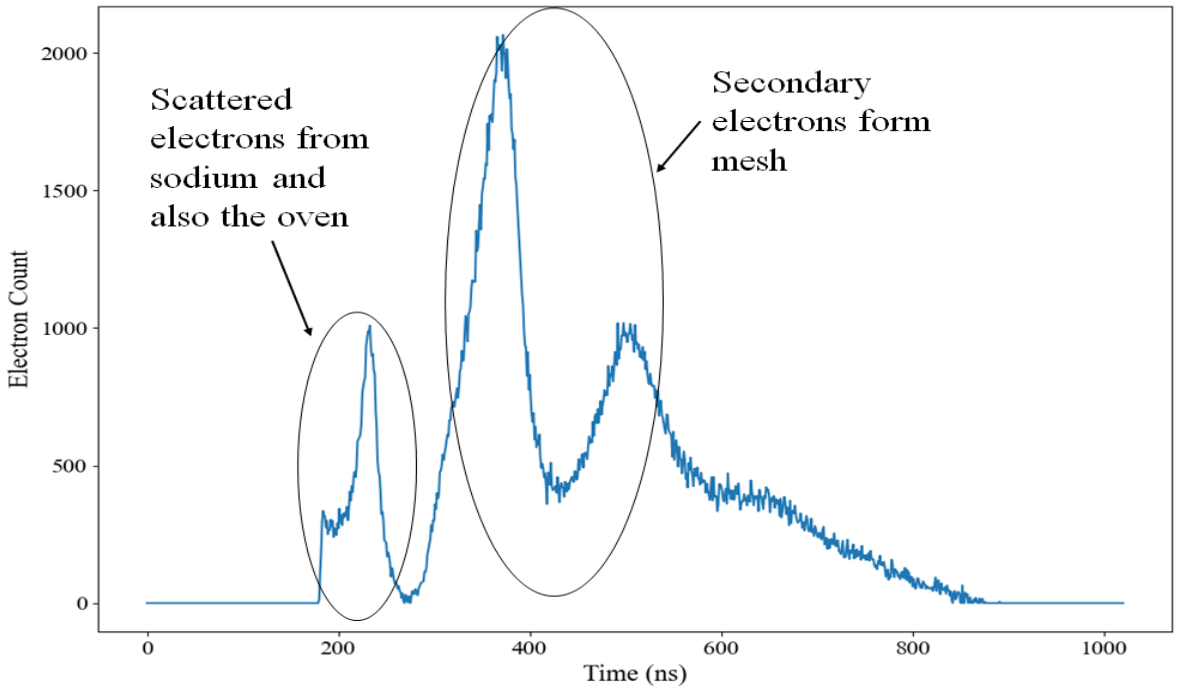

Figure 4.13: Time-resolved measurement of electron counts detected over a 20 s period, showing different electrons groups reached the detector. The first peak corresponds to electrons scattered from both the sodium atoms and the oven surface, while the second peak represents secondary electrons originating from the mesh.

After implementing the proposed solutions we repeated the experiment. The results showed a significant reduction in the number of unwanted electrons reaching the detector within the time window corresponding to our primary group of interest — the electrons scattered from the sodium atoms. This indicates that the majority of the unwanted

electrons were successfully eliminated or delayed outside of the desired time bin. Fig. 4.14 shows the improved signal detected by the detector, highlighting the effectiveness of these adjustments in isolating the electrons scattered from sodium atoms.

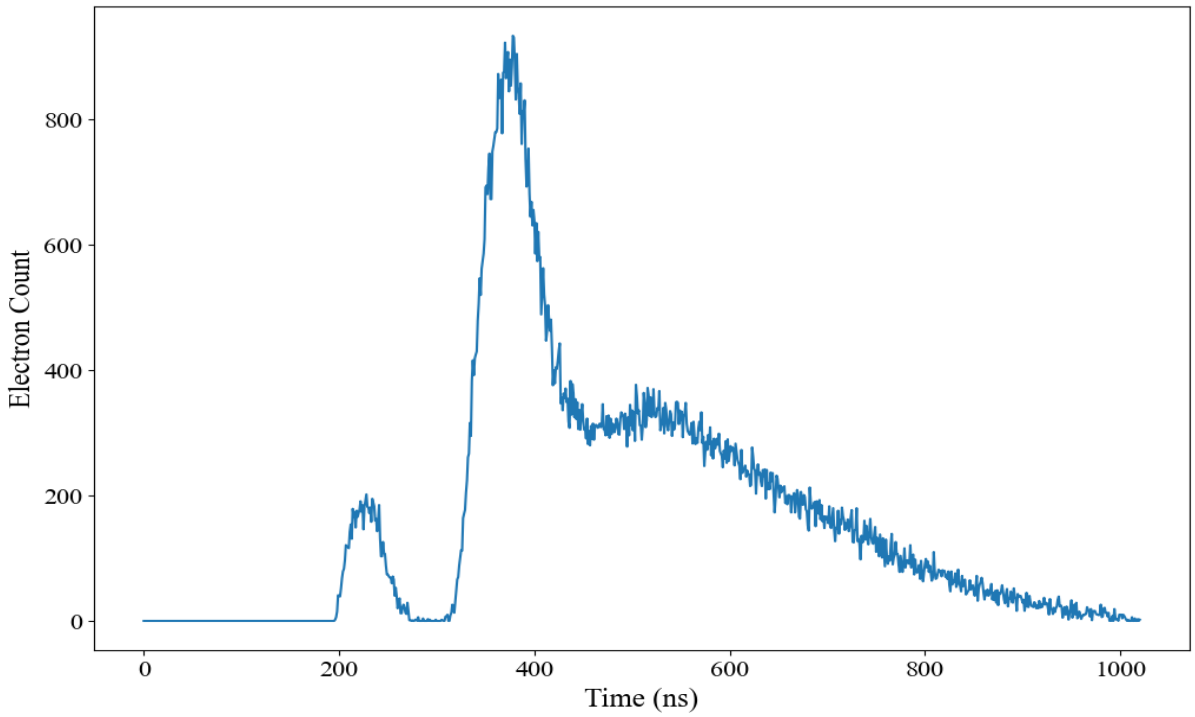

Figure 4.14: Improved signal detected by detector after implementing the proposed solutions.

Despite of the improvements in the experiment, we observed that the number of detected electrons was still higher than expected values in the calculations. Upon further investigation, we realized that the issue was due to the relatively high residual gas pressure in the vacuum chamber. The minimum achievable pressure in this chamber was approximately 1×10^{-6} mbar. At this pressure, a significant number of residual gas molecules, predominantly nitrogen and oxygen, remain in the chamber and since the scattering cross sections for nitrogen and oxygen atoms at the angles used in our experiment are approximately ten times larger than that for sodium, a substantial fraction of the detected electrons likely originated from scattering off these background gas molecules. To ensure that the dominant contribution to the scattered electrons came

from sodium atoms, we calculated that the chamber pressure needed to be reduced to at least 1×10^{-7} mbar. To achieve this, we moved the electron gun to the main chamber, which could be evacuated to a much lower pressures.

Fig. 4.15 illustrates both the schematic and the actual experimental setup designed for our experiment. As it is mentioned before, we noticed that the focus position of the electron beam is highly sensitive to the alignment of the UV light and its position on the cathode. To ensure that the electron beam remains precisely directed towards the interaction region, we implemented a small monitoring detector similar to the one used for profiling the electron beam (as shown in Fig. 4.7). The main modification was increasing the input aperture of the detector to 2 mm, which is match with the size of the electron in the interaction region. This monitoring detector is mounted on a movable stage, allowing us to verify the alignment and position of the electron beam by placing it directly at the interaction region before and during the experiment.

Additionally, Fig. 4.15 shows the meshes positioned around the interaction region, which serve as an electrostatic shield. These meshes are placed at a specific distance from the electron gun to optimize the separation between secondary electrons originating from these meshes and the primary electrons scattered off the sodium atoms. By optimizing their distance, we achieved a better temporal separation between the secondary and primary electron signals.

Also, to investigate the scattering process and optimize the electron transferring to the Mott detector, we first installed the first lens group of the electron transfer system in its designated position. By using only the first lens group initially, we were able to evaluate its performance in transporting the scattered electrons and this step-by-step approach allowed us to identify and address any issues in the electron transfer system before incorporating the subsequent two lens groups, thereby ensuring a reliable and efficient electron transport path to the Mott detector.

The "first lens" indicated in the figure represents the first lens of the first lens group,

with an input aperture diameter of 4 mm. This aperture size effectively defines the field of view for the system, allowing only electrons scattered from sodium atoms within a narrow angular range of $60° \pm 5°$ to enter the electron transfer system.

After setting up and aligning all components, we proceeded to measure the number of scattered electrons from the sodium atoms that reached the detector. To do this, we placed an MCP after the first lens group. The voltage of the front side of the MCP was set to the same voltage as the last lens to prevent any changes in the electrons' trajectories during measurements. We then conducted the experiment and recorded the number of scattered electrons over various time intervals, as shown in Fig. 4.16. For previous measurements, we recorded the electron count over a duration of 20 s. However, since we are now capturing only the electrons scattered from sodium atoms, which are relatively low in number, we increased the measurement duration to 50 s. All subsequent data presented are based on this 50 s measurement time.

As previously noted, we observed that at higher pressures within the chamber, additional electrons were detected that had scattered from the residual air in the chamber. Since the input aperture of the first lens only allows electrons scattered from the interaction region to enter the electron transfer system, we used this characteristic to our advantage. To avoid complications associated with handling sodium and to prevent contamination of the chamber, we increased the chamber pressure without turning on the oven. We then assessed the electrons scattered from the residual air, noting that these electrons exhibited similar trajectories and timings to those scattered from sodium. Fig. 4.17 shows the number of detected electrons over time for different vacuum pressures inside the chamber, which shows similar timing with the scattered electrons from sodium atoms.

The next step in the experiment was monitoring the spatial distribution and profile of the detected electrons at the end of the first lens group and comparing it with the simulations. For this measurement, since there was no UV light in the electron transfer system path, we were able to easily use the MCP-phosphor screen combination to directly

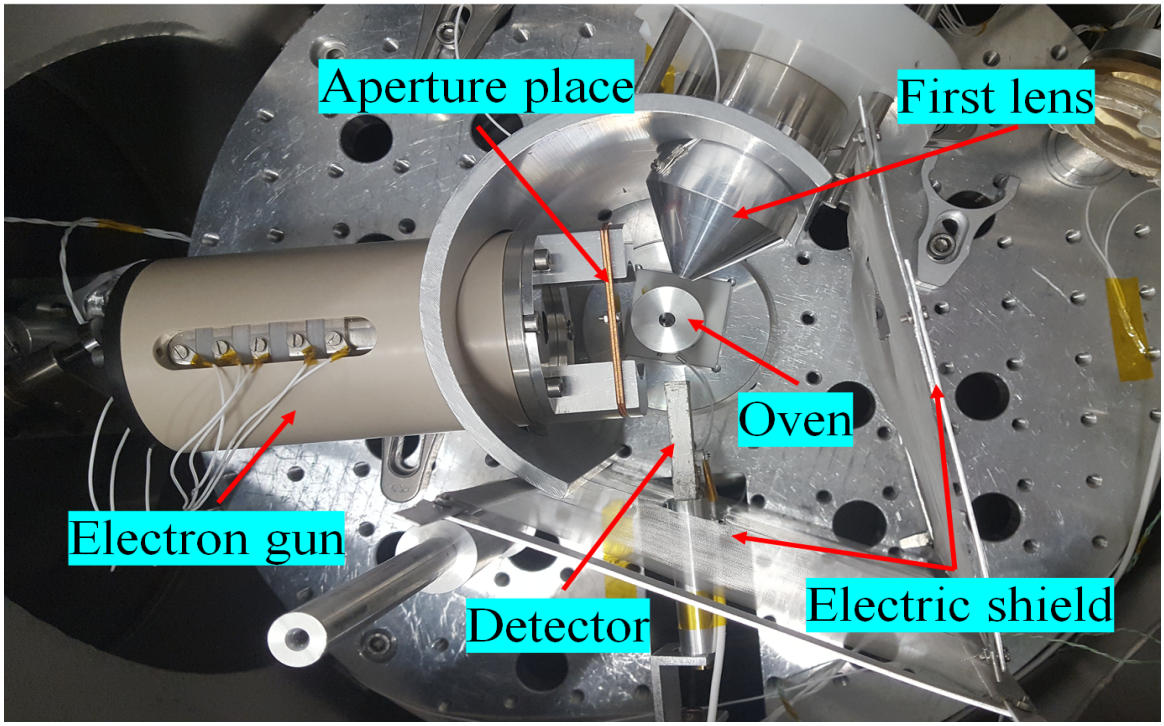

(a)

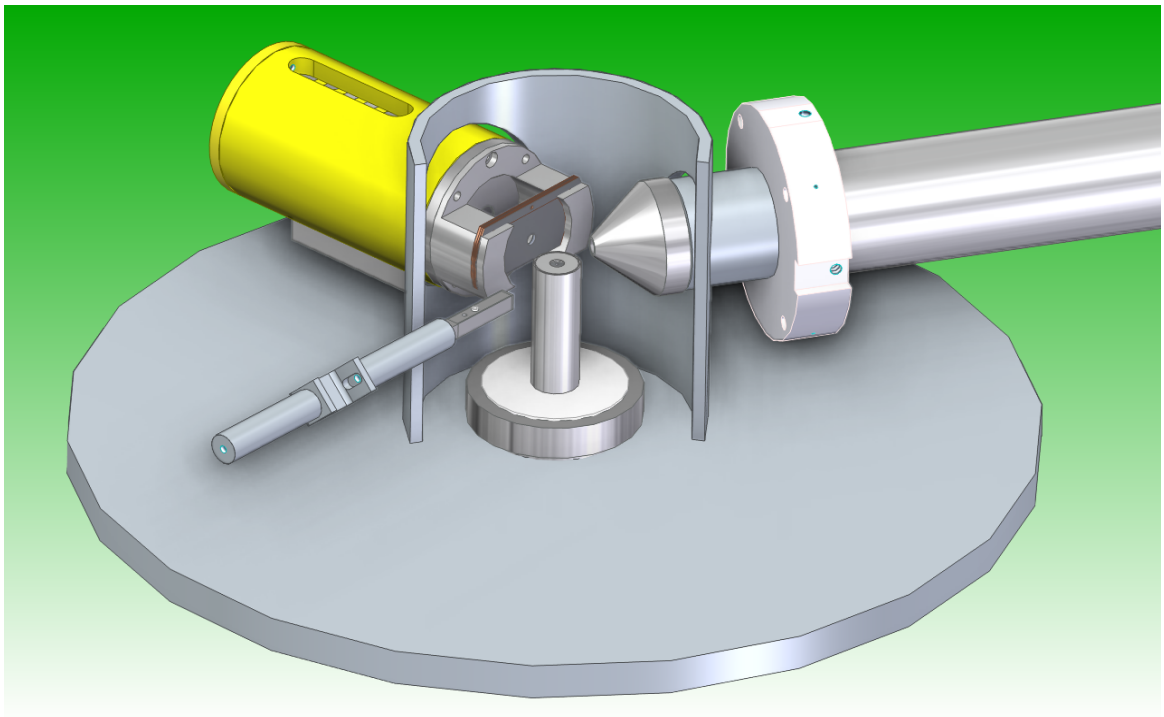

(b)

Figure 4.15: The experimental setup (a) and its CAD view b) with key components in final setup.

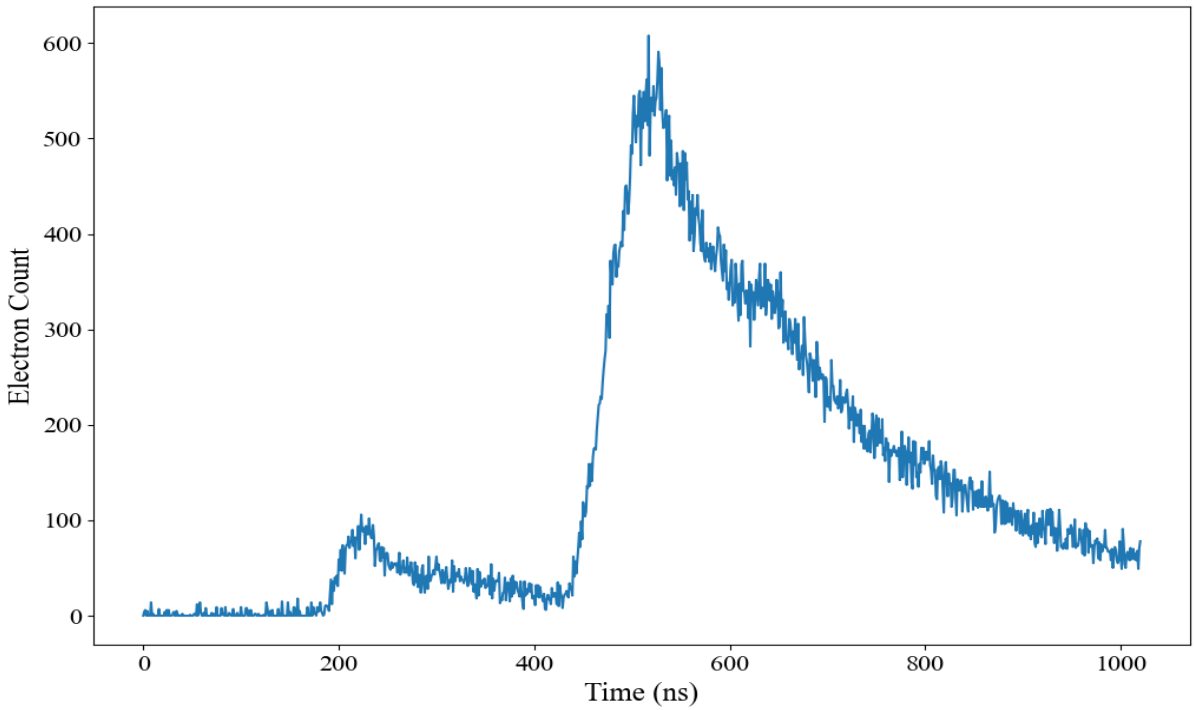

Figure 4.16: Time-resolved measurement of electron counts detected by the MCP over 50 s, with a base pressure of the chamber at 1.7×10^{-7} mbar.

visualize the electron beam distribution at the end of the first lens group. By using this method, an image of the electron beam profile was obtained, which is shown in Fig. 4.18a.

However, we suspected that the observed profile might be dominated by the profile of the second group of electrons, which arrive at the detector at different times and in larger delays than the primary scattered electrons. In this case the results could be misleading and the first group of electrons, which are scattered electrons form the atoms, have a different beam profile. Therefore, we needed to distinguish between these groups to ensure the accuracy of our measurements.

To achieve this experimentally, as shown in Fig. 4.19, we realized that applying a negative potential less than -10 V to the second lens in the electron transfer system could effectively retard and stop electrons from reaching the detector. Therefore, by using a pulsed voltage on the second lens—applying 0 V when the first group of electrons (scattered from sodium atoms or residual gases) arrives to this lens and switching to

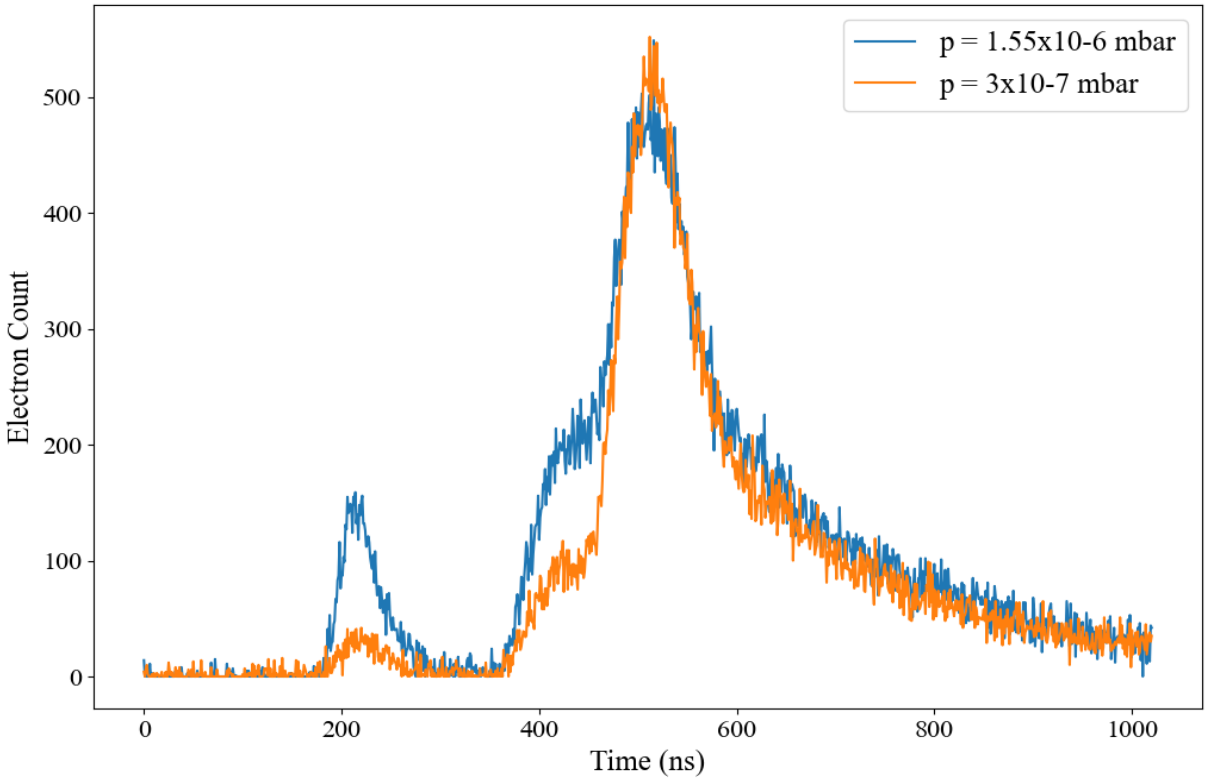

Figure 4.17: Time-resolved measurement of scattered electrons from residual air, detected at different base pressures of the vacuum chamber.

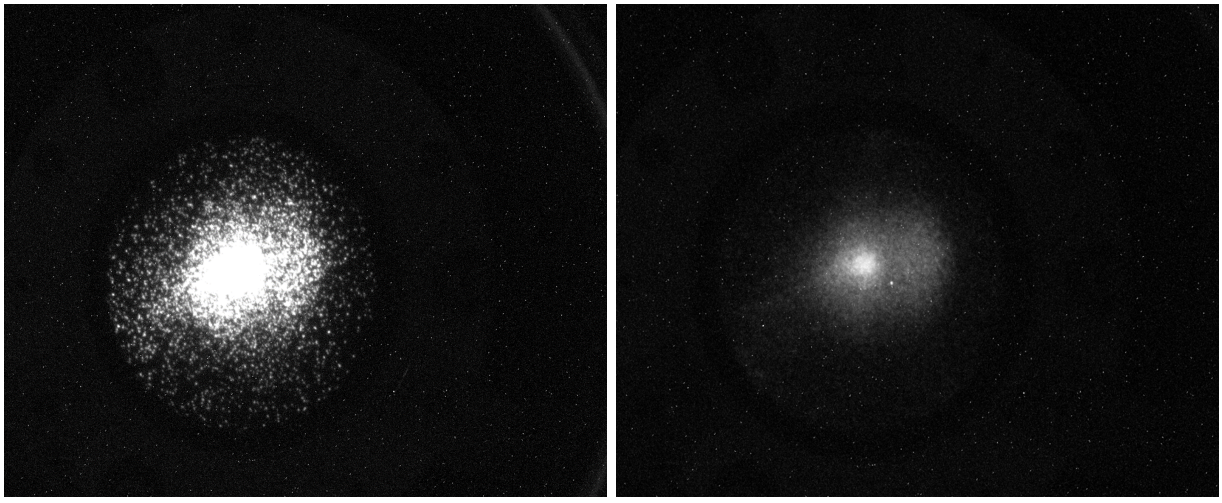

(a) (b)

Figure 4.18: The experimental results for monitoring the electron beam profile with an applied voltage of 0 V (a) and -12 V (b) on the second lens.

negative voltage when the second group of electrons arrives—we ensured that only the first group of electrons reached the detector. Therefore, this approach allowed us to

isolate the scattered electrons from sodium atoms and accurately visualize their spatial distribution and profile.

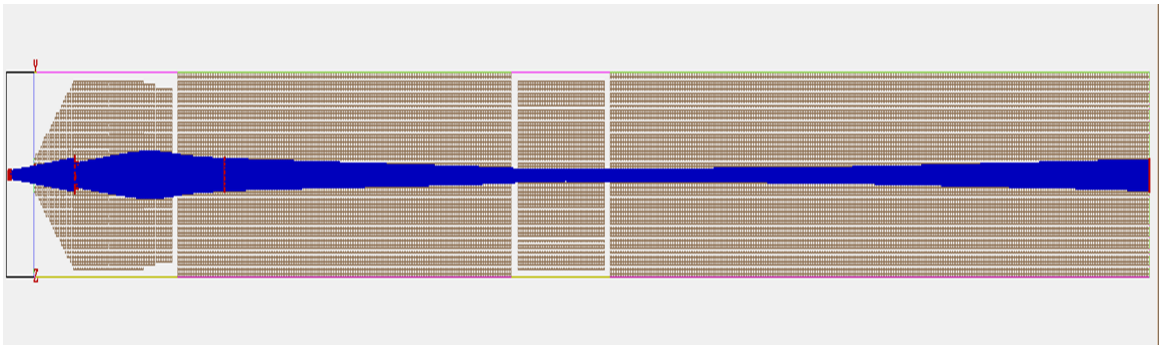

(a)

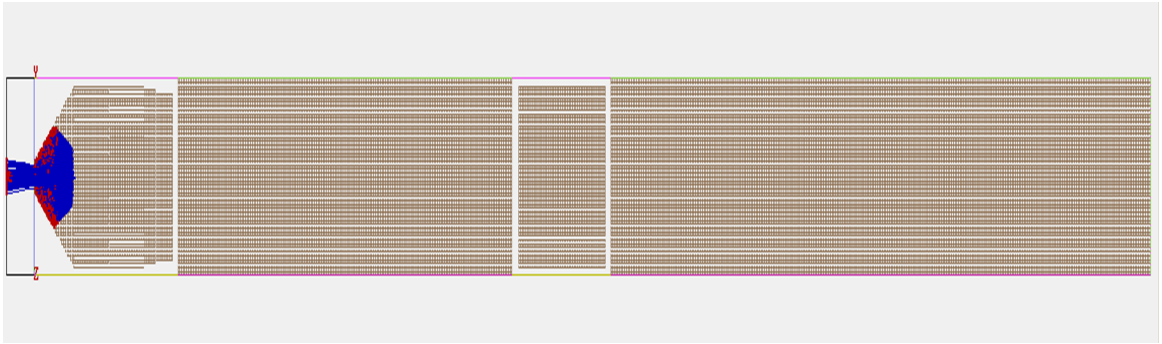

(b)

Figure 4.19: The simulation results using SIMION showing the electron trajectories with an applied voltage of 0 V (a) and −12 V (b) on the second lens.

After implementing this pulsed voltage technique, we were able to successfully visualize the electron beam profile of the first group of electrons at the end of the first lens group. The results, shown in Fig. 4.18b, confirmed that the position of the scattered electrons from sodium atoms matched the previously observed profile, but the size of the scattered electron beam from sodium atoms is smaller.

Next, we added the second lens group, which consists of two lenses and the length of each one is 1 m. We first installed the first lens of this group and measured the profile and time of flight of electrons and then added the second lens. Fig. 4.20 represents the time-resolved distribution of electrons reaching the detector after passing through the first lens group, the first lens of the second group, and the whole second group.

According to simulations, the time-of-flight difference between electrons scattered from sodium atoms after the first lens group and after the first lens of the second group should be approximately 75 ns. Additionally, the time difference between electrons after the first lens group and the second group should be around 127 ns. As shown in the figure, these time differences are consistent with the simulations, confirming that the electron transport is in good agreement with the expected results.

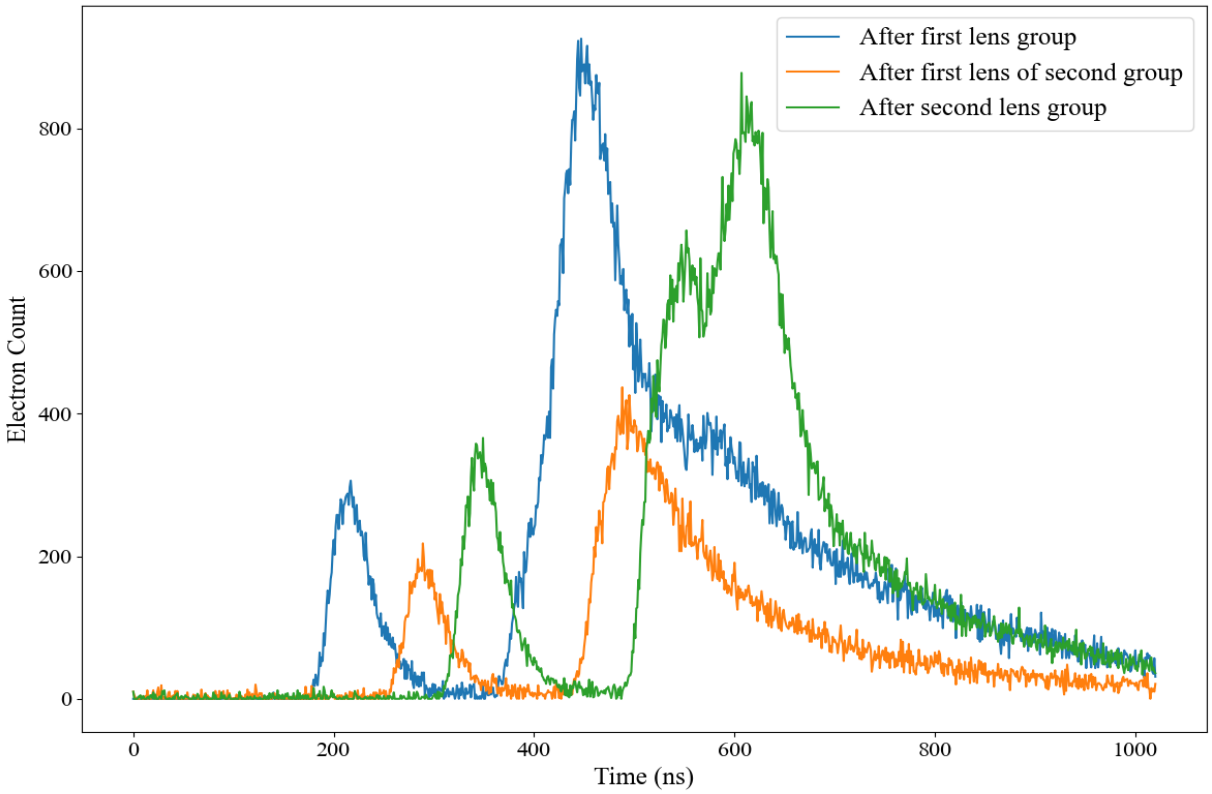

Figure 4.20: Comparison of the time-of-flight (TOF) of scattered electrons after the first lens group, the first lens of the second group, and the complete second group. The variations in the measured number of electrons are due to slight differences in chamber pressure and adjustments in the deflector voltage, which resulted in fluctuations in electron counts.

We also examined the electron beam profile after the second lens group, which is shown in Fig. 4.21. Similar to the previous setup, we applied the same procedure to retard the second electron group and visualize the main group of electrons which were scattered from atoms. The results confirmed that the electron beam profile after the second lens group

closely matched the simulations.

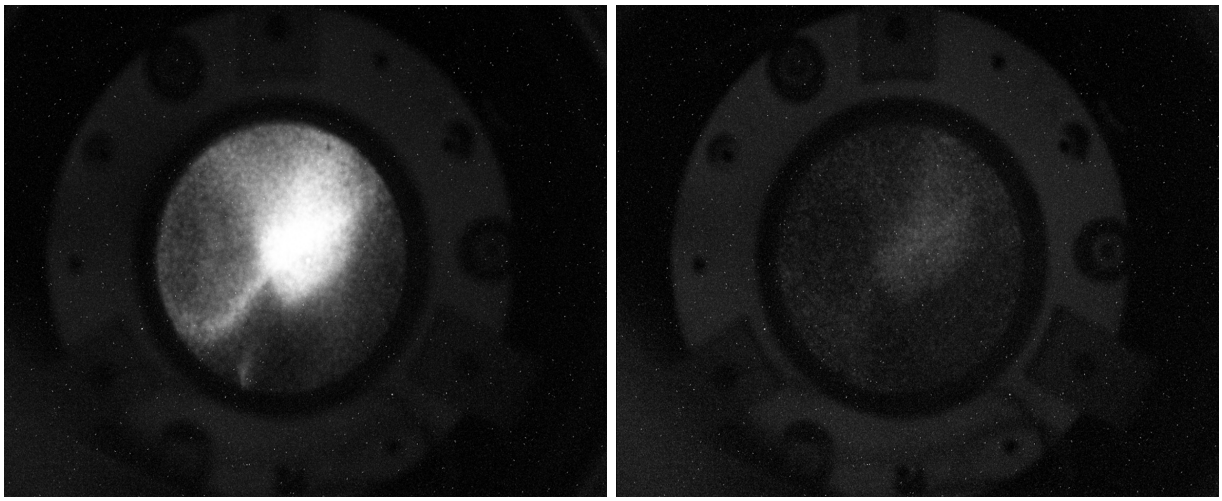

(a) (b)

Figure 4.21: The experimental results for monitoring the electron beam profile after second lens group with an applied voltage of 0 V (a) and −12 V (b) on the second lens.

During these measurements, we observed that the beam position was highly sensitive to the voltage applied to the first deflector, which, as mentioned earlier, is located in the first lens group. Even small changes of 2 or 3 V had a significant impact on the electron trajectories. Fig. 4.22 illustrates the effect of adjusting the deflector voltage on the number of electrons reaching the detector. This finding highlights the importance of fine-tuning the deflector voltage during the final measurements to ensure efficient transfer of all scattered electrons from sodium atoms to the Mott detector.

Finally, we added the last lens group to the setup and with this lens group the whole length from interaction region to the Mott detector is 3 m. The entire electron transfer system setup is shown in Fig. 4.23. As shown in the photo, we wrapped μ-metal around the entire system to shield the electron path from the Earth's magnetic field and minimize its influence on the trajectory of the electrons. The third lens group is connected to another vacuum chamber that houses the Mott detector. However, due to the large number of connectors and measuring devices attached to this chamber, it was impractical to use μ-metal shielding in that area. Also, during test measurements, we discovered that the

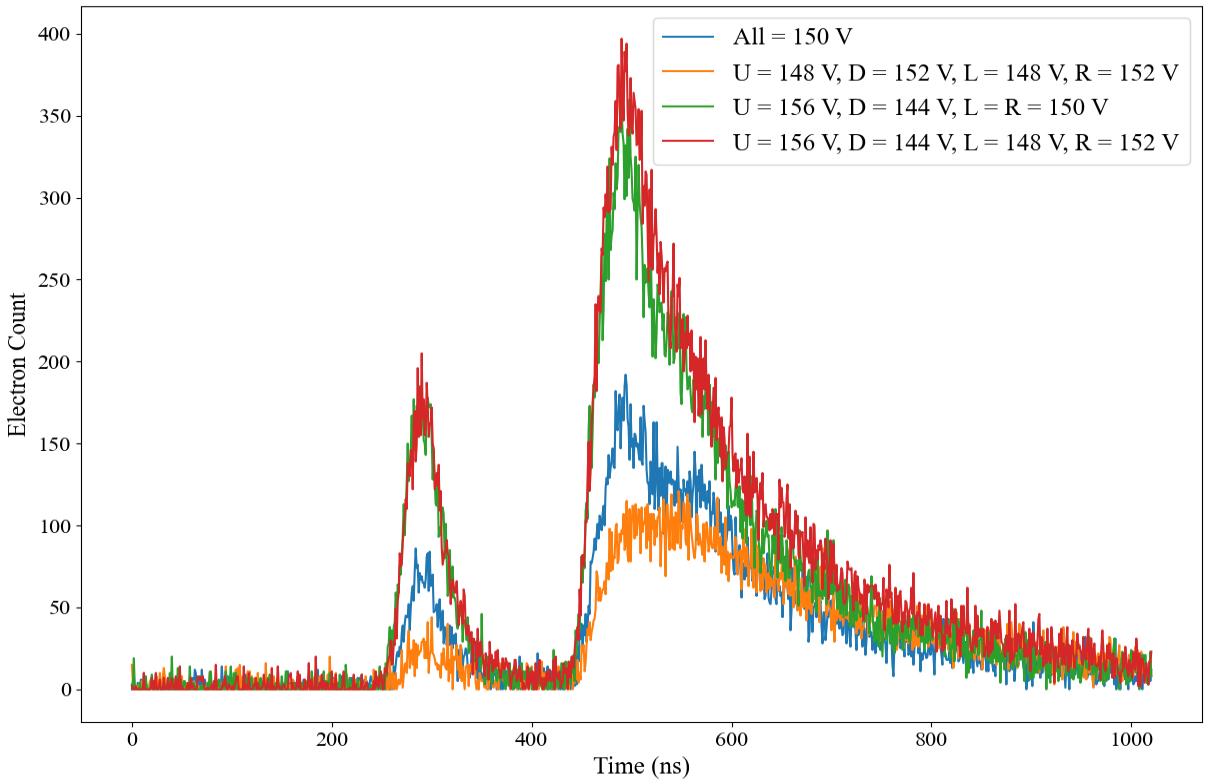

Figure 4.22: Effect of the deflector voltage settings on the number of detected electrons after the first lens of the second group. "U" refers to the upper side of the deflector, while "D," "L," and "R" correspond to the down, left, and right sides, respectively.

Earth's magnetic field still affected the trajectory of the electrons in this unshielded region. To solve this problem, we constructed additional TSH coils to compensate the Earth's magnetic field in this area.

The magnetic field inside of the electron transfer system, from the interaction region to the last lens, was measured, and Fig. 4.24 shows the magnetic field components in the x, y, and z directions. Here, the z and y components are perpendicular to the trajectory of the electrons, while the x component is parallel to it. As shown in this figure, the x and y components are well-compensated, but the z component still exhibits three small regions of non-zero magnetic field, particularly at the transitions between the μ-metal and the TSH coils. However, since these regions are small, they do not have a major effect on the trajectory of the electrons and can be further corrected using the deflectors, which are placed in the first and third lens groups.

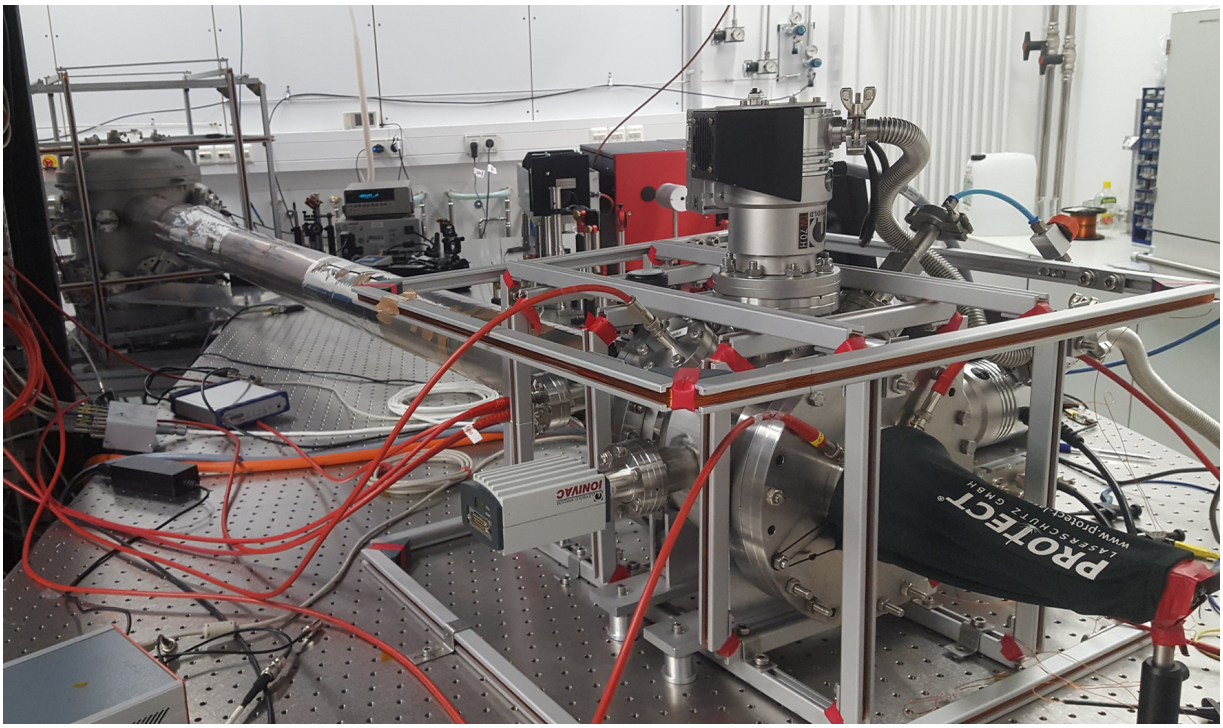

Figure 4.23: The full electron transfer system setup and its μ-metal shielding to minimize the influence of the Earth's magnetic field on the electron trajectories. Also, the vacuum chamber, which houses the Mott detector and its TSH coils are shown.

After implementing all the lenses, we measured the number of scattered electrons and their profile at the end of the third lens group using the same procedure for other lens groups. Fig. 4.25 shows the measured number of electrons at the end of the third lens group. The higher number of detected scattered electrons in this measurement is due to the higher pressure inside the chamber compared to previous measurements for the other lens groups. Additionally, the arrival time for the electrons at the detector was only about 5 ns later than the previous group, which is expected according to relatively short length of this lens group (approximately 32 cm). The electron beam profile is shown in Fig. 4.26 and confirms that the position and distribution of both electron groups are similar to previous measurements.

After the third lens group, two additional lenses are connected to the Mott detector, which highly focus the electron beam for spin polarization measurements. Since the total length of these lenses is 21 mm we can confidently conclude that the scattered electrons

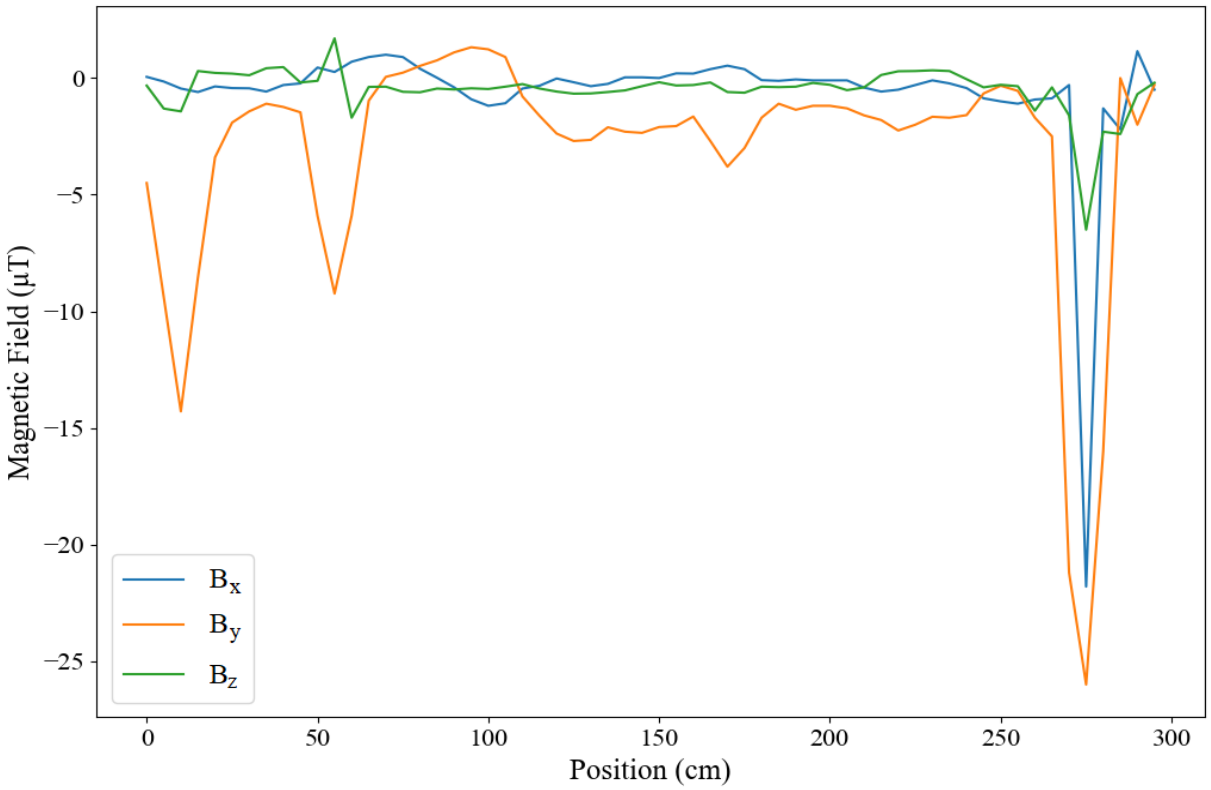

Figure 4.24: Measured magnetic field components (B_x, B_y, B_z) along the electron transfer system. The x component is aligned with the electron beam direction, while the y and z components are perpendicular. The magnetic field is well-compensated by the μ-metal shielding and TSH coils, with some residual magnetic field near the transitions between the shielding and coil systems.

were successfully transferred to the Mott detector for further analysis.

As mentioned before, all previous measurements were based on electron scattering from residual gases in the vacuum chamber and it is necessary to test whether we could obtain similar results for scattered electrons from sodium atoms. Furthermore, due to the low scattering cross section of sodium atoms and the low efficiency of the Mott detector (approximately 10^{-3}), simulations indicated that the system would need to operate for around 40 hours to collect enough data to reduce statistical error and improve the validity of the measurements. Therefore, it is important to assess the long-term stability and performance of the electron gun and the sodium oven.

To test the system's stability, we filled the oven with sodium and increased the

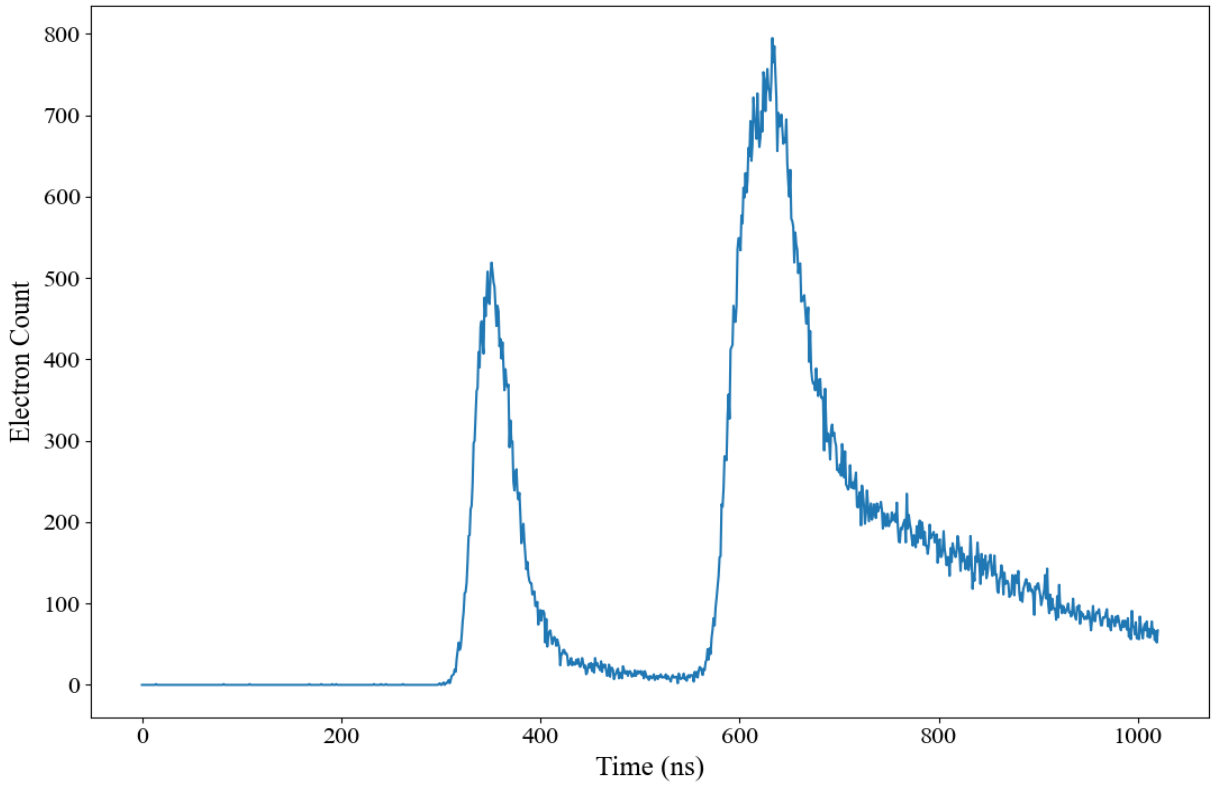

Figure 4.25: Time-resolved measurement of scattered electrons by residual air. The pressure was 3×10^{-6} mbar for this measurement.

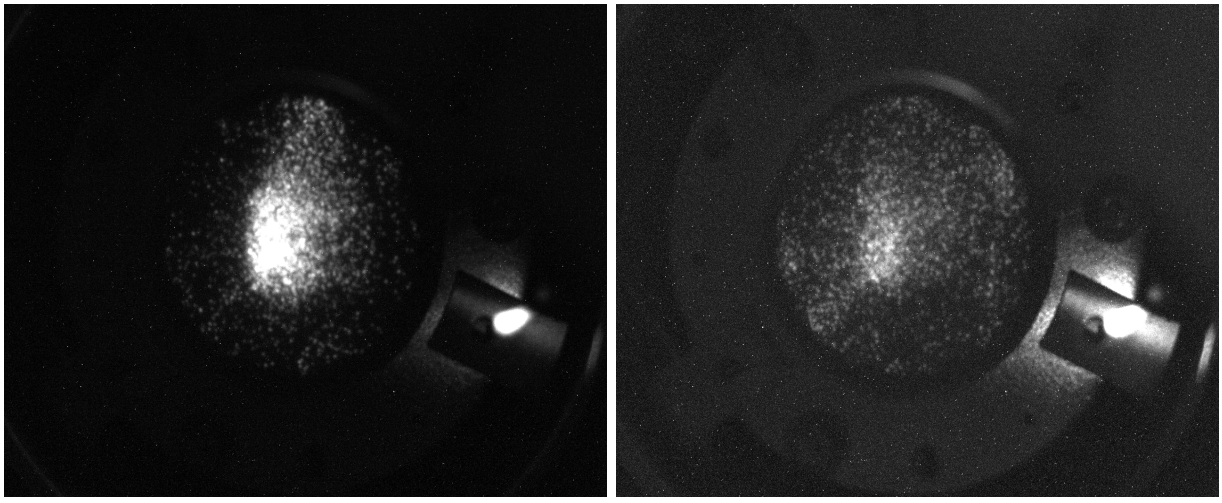

(a) (b)

Figure 4.26: The experimental results for monitoring the electron beam profile after the third lens group with an applied voltage of 0 V (a) and −12 V (b) on the second lens.

temperature to 300 °C. First measurements indicated that the arrival time distribution of electrons scattered from sodium atoms was similar to those scattered from residual

gases in the vacuum chamber. But, after approximately 2 hours, significant changes in the distribution were observed and we detected a large number of electrons scattered from various parts of the experimental setup, which distorted the timing measurement plots.

In order to investigate the issue, we measured the output current of the electron gun and found it much higher than the current at the start of the experiment. After examining the cathode surface, we observed that sodium atoms had deposited on its surface, likely reacting with the silver coating. This reaction appeared to change the quantum efficiency of the silver layer, leading to an excessive generation of electrons. The excessive electron generation created space charge effects, which changed the trajectory and energy of the output electrons from the electron gun and causing widespread scattering and disrupting the measurements. Fig. 4.27 shows the effect of sodium deposition on the cathode and its impact on both the number of detected electrons and their time distribution at the end of third lens group.

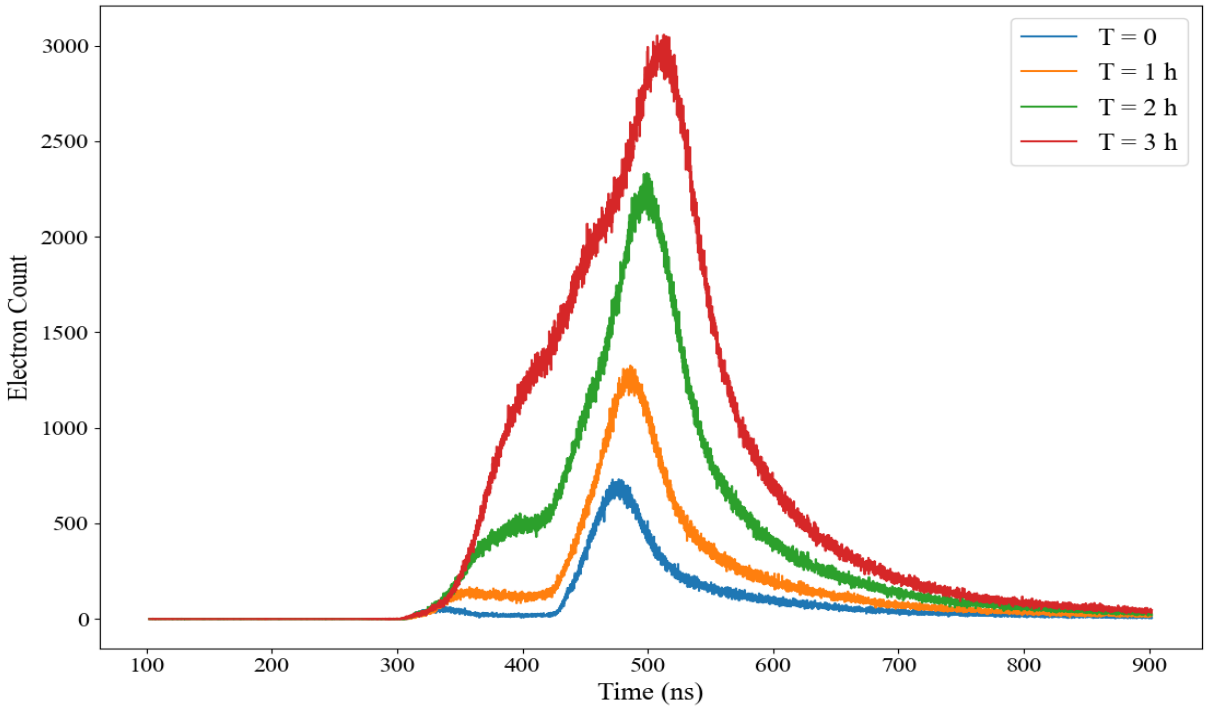

Figure 4.27: Effect of sodium atom deposition on the surface of the silver-coated cathode after 3 hours of oven operation. The temperature of the oven was 300 °C for these measurements.

Our first attempt to fix this issue was to reduce the UV light power to decrease the number of generated electrons. While this improved the situation, there were still too many electrons for reliable measurements.

As a next attempt, we explored alternative materials for coating of the cathode and found that copper was less reactive with sodium than silver. Therefore, we coated the cathode with copper and repeated the measurements. Although we observed that the deposition of sodium atoms on the cathode surface still increased electron generation but we were able to reduce the number of generated electrons by reducing the UV light power. This approach restored a clean electron profile, allowing us to continue with the experiment. Fig. 4.28 shows the results from the copper-coated cathode after 5 hours operating the system, which demonstrate its improved performance compared to the silver-coated cathode. As shown in this figure the arrival time range for scattered electrons reaching the end of the third lens group is between 320 ns to 380 ns, which is important for next step of our experiment.

4.4 Yellow Light Propagation

As outlined in Section 2.1.1, after distributing the sodium atoms to Alice and the electrons to Bob, in the next step Alice photo-excites her sodium atoms using circularly polarized photons and since the sodium atoms are entangled with the electrons, the circular polarization of the exciting photons is transferred directly to the spin polarization of the electrons. In this section, we will discuss about the laser source and the creation of the time delay, which is necessary for proper timing of the photo-excitation process.

The main challenge in this step is that the photo-excitation must occur at a precise moment—when the electrons are far from the sodium atoms and close to the Mott detector. To ensure proper timing, we measured the delay between the trigger signal and the yellow light emitted by the dye laser. Since all previous measurements used the photo-diode signal

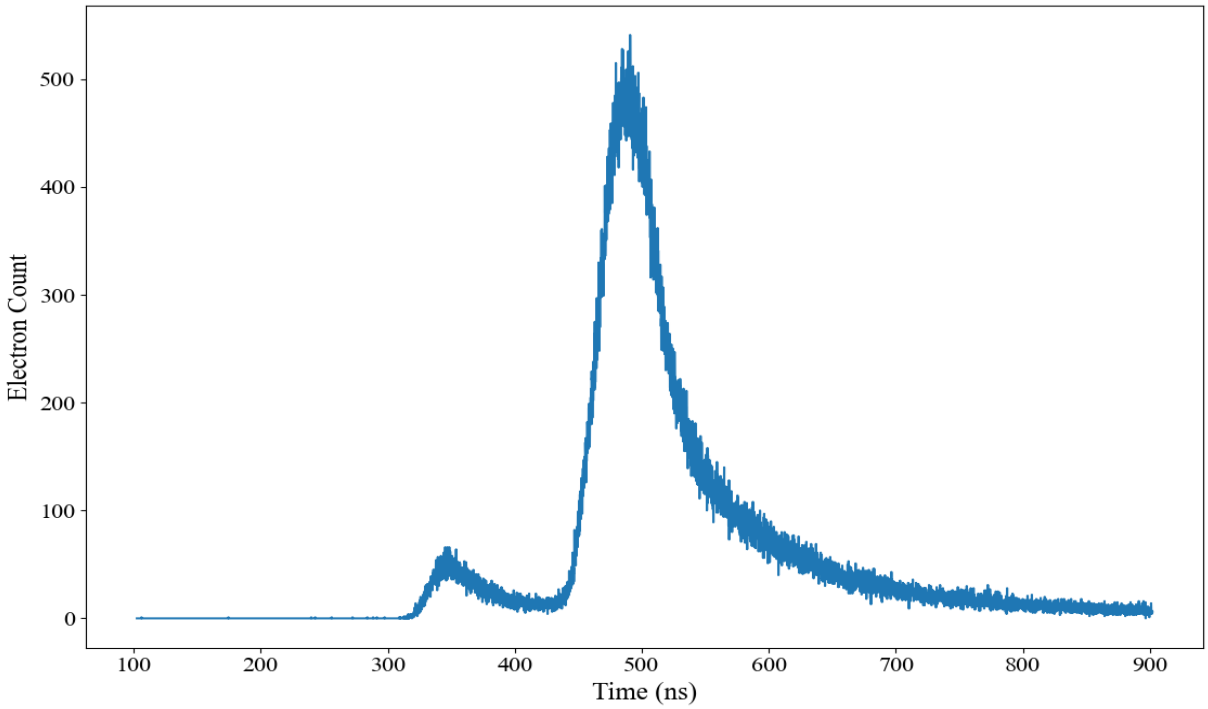

Figure 4.28: Time-resolved profile of scattered electrons from sodium atoms by using copper-coated cathode after running the system for 5 hours. The temperature of the oven was 310 °C for these measurements.

(as shown in Fig. 4.1), which is located after the harmonic separator mirror and detects the green light, we must compare the laser timing with the same trigger. The measured delay between the laser pulse and the trigger, as shown in Fig. 4.29, was approximately 7 ns. However, we need a total delay of about 330 ns between the trigger and the light reaching the interaction region, which must be implemented in the setup.

To achieve this delay, we initially decided to generate it in free space by using mirrors. Since an additional delay of 320 ns corresponds to approximately 97 m of light propagation in free space, we designed a system to extend the light's path accordingly.

At first, we implemented a laser stabilization system after the laser output. Stabilization was essential due to the long optical path, as even minor fluctuations in the laser beam could disrupt the alignment. Following this, we expanded the beam to a diameter of 10 mm using a pair of lenses to ensure proper collimation over the long distance.

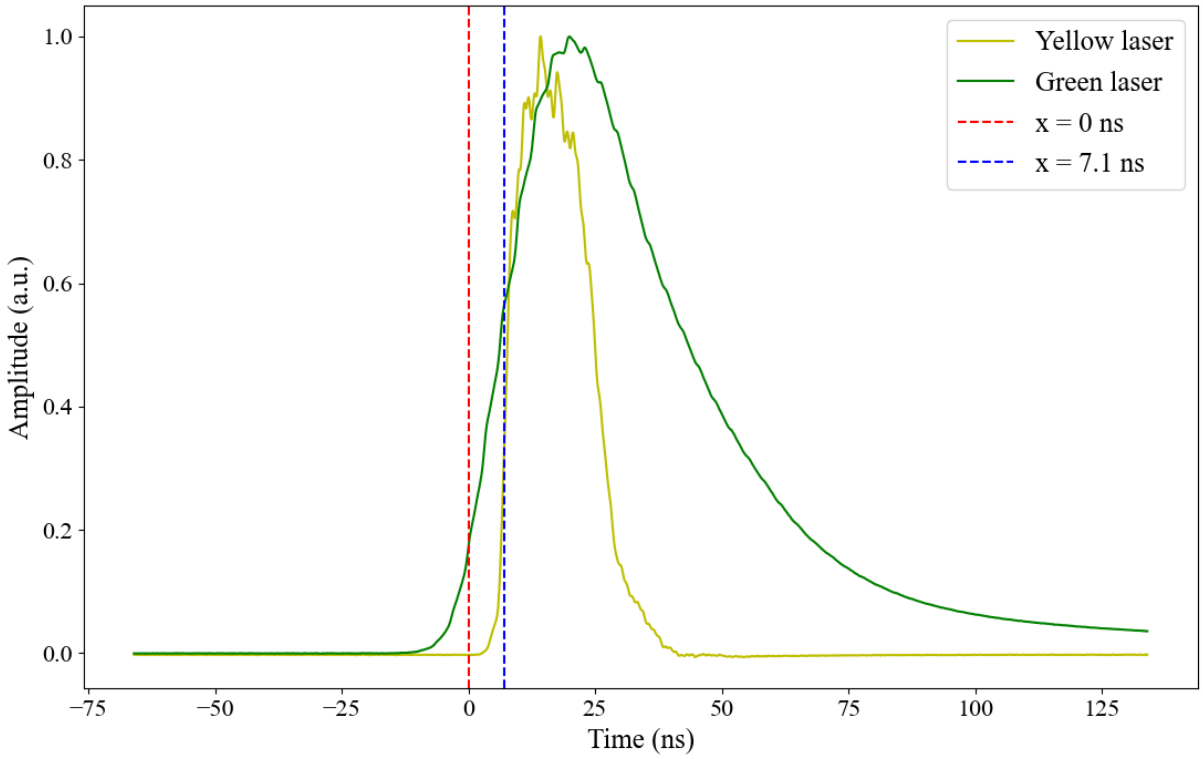

Figure 4.29: Timing comparison between the green light at the photodiode position and the yellow light at the dye laser output. The zero line represents the exact moment when the trigger is activated, serving as the reference point for the experiment.

Then, to avoid occupying too much space, the laser beam was reflected multiple times between closely spaced mirrors. As shown in Fig. 4.30, the input beam enters the system and is reflected three times by each mirror. After these reflections, the beam is directed to a periscope, which raises the beam height by approximately 3 cm. The beam is then reflected back along a parallel path through the same set of mirrors, now at a higher level, without any overlap or interference. The beam is then reflected by the final mirror, exiting the delay system. Finally, the beam passes through two additional lenses to reduce its size before entering the vacuum chamber.

The total length of optical path achieved through this configuration was approximately 97 m, corresponding to a delay of around 320 ns. However, long distance propagation made the system highly sensitive to even slight vibrations or air fluctuations, leading to beam misalignment. While the setup was stable for distances up to around 50 m (with stability

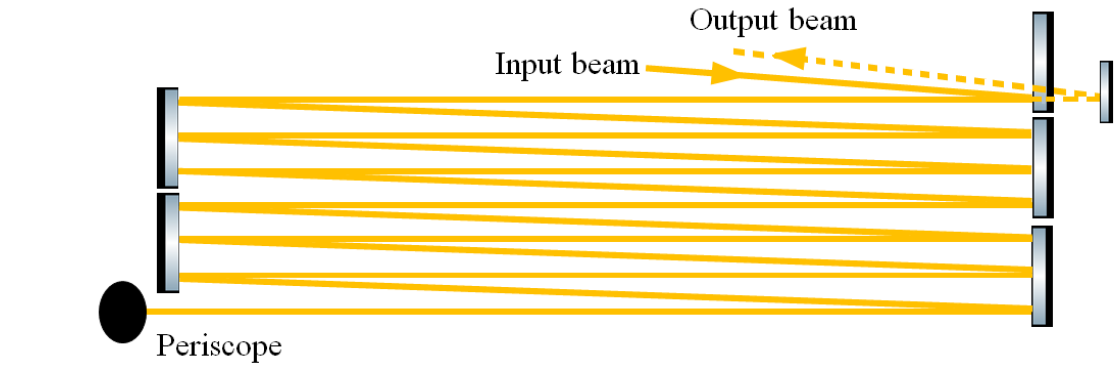

(a)

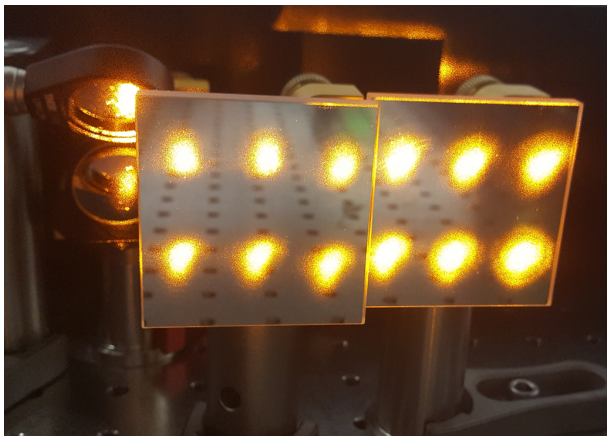

(b)

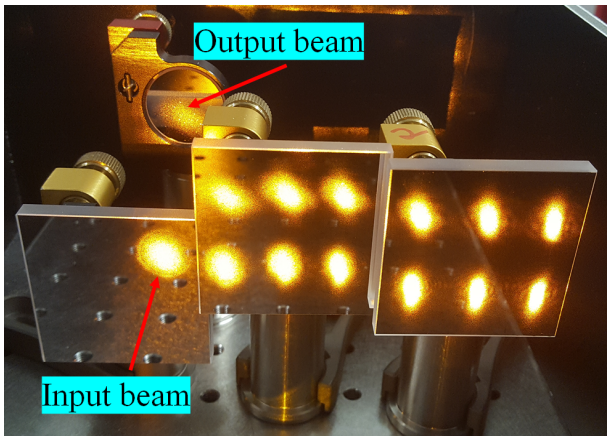

(c)

Figure 4.30: a) The schematic of the optical system for generating the time delay. The beam profile is shown for the left(b) and right (c) side mirrors. The space between the right side and left side mirrors is approximately 320 cm.

maintained for up to two days), for the whole 97 m the beam was completely misaligned after just 3-4 hours.

Despite this configuration successfully providing the required optical delay, the challenge of maintaining beam alignment over time prevented us from continuing with this setup, so we decided to use an optical fiber to create the required delay. The main concern with propagating light through optical fibers is the potential for nonlinear effects. However, given that the pulse width of our laser is around 20 ns and the peak power is only approximately 1.15 kW, nonlinear effects are not a significant risk in this case. To further mitigate any potential issues and to avoid focusing the light tightly and minimizing the likelihood of nonlinear effects, we used a multimode fiber with a large core diameter of

600 μm.

The choice of a large-core fiber provided additional advantages, which reduced sensitivity to beam oscillations, ensuring that minor fluctuations in the laser's position would not affect the coupling efficiency, particularly during a long-time measurement.

The only disadvantage of using a multimode fiber was that the output beam became unpolarized after propagation through the fiber. To solve this issue, we placed a polarizing beam splitter cube after the fiber output to separate the unpolarized beam into its linearly polarized components. We selected the transmitted linearly polarized beam for our experiment. Following this, we used a quarter-wave plate to convert the linearly polarized beam into circular polarization and by rotating the quarter-wave plate by 90 degrees, we could switch between right-handed and left-handed circular polarization, providing control over the desired polarization state. Fig. 4.31 shows the experimental setup for coupling the beam in and out of the fiber, as well as the use of the polarizing cube and quarter-wave plate for generating the desired optical delay and polarization. However, this approach resulted in a 50% loss of beam power due to the separation of the unpolarized components by the polarizing beam splitter. Fortunately, we had enough power, so this reduction did not create any problem for our measurements.

After transmitting the beam through the entire fiber setup, which had a transmission efficiency of approximately 90%, we obtained around 110 mW of power after the fiber. With the addition of the polarizing cube, quarter-wave plate, and a lens for beam collimation, we achieved a circularly polarized beam with a power of 45 mW, which based on simulations was sufficient for conducting the measurements. We then directed the beam into the vacuum chamber and measured the total optical delay, which was around 330 ns and is shown in Fig. 4.32.

With the successful generation of the required delay, all preparations for the final experiment were completed. The system was fully operational, and we proceeded to conduct the final measurements, as detailed in the next chapter.

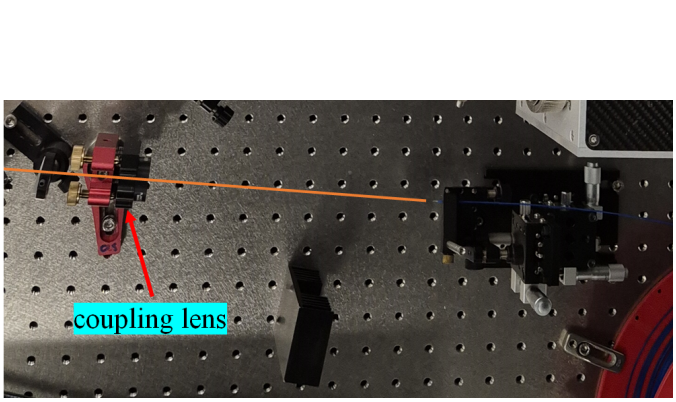

(a)

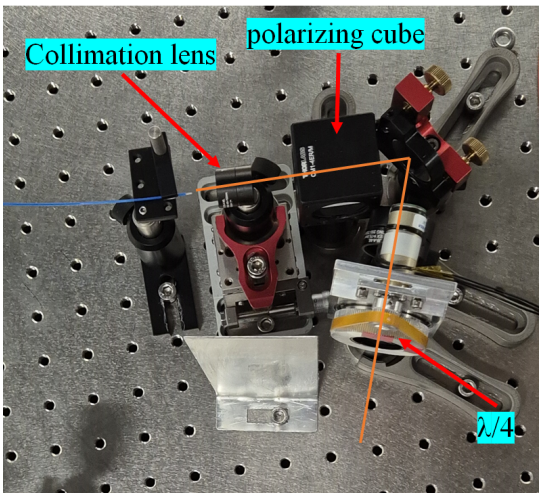

(b)

Figure 4.31: Coupling the beam in a) and out (b) of the fiber. The quarter wave plate is place on a motorized rotatory stage to switch between right and left circularly polarized beam.

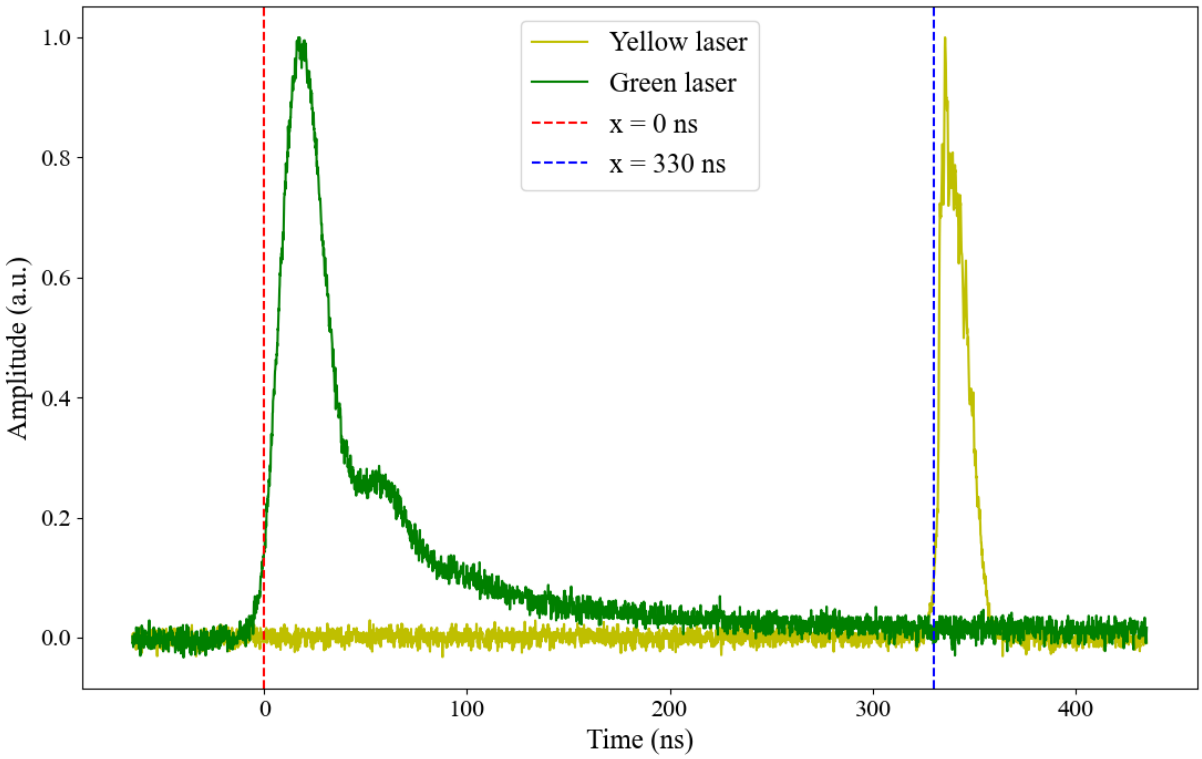

Figure 4.32: The measured optical delay between the trigger pulse (green laser) and the yellow light at the interaction region. The length of used fiber was 63 m.

5. Results and Discussion

5.1 Final Experimental Results

After testing and optimizing the individual components of the experiment, such as the electron gun, sodium oven, electron transfer system, and confirming that scattered electrons were successfully transmitted to the Mott detector, and creating the desired optical delay for the yellow light, we connected the Mott detector to the system, which allowed us to directly measure the spin polarization of electrons from the scattering experiment. Fig. 5.1 shows the complete electron transfer system with the Mott detector.

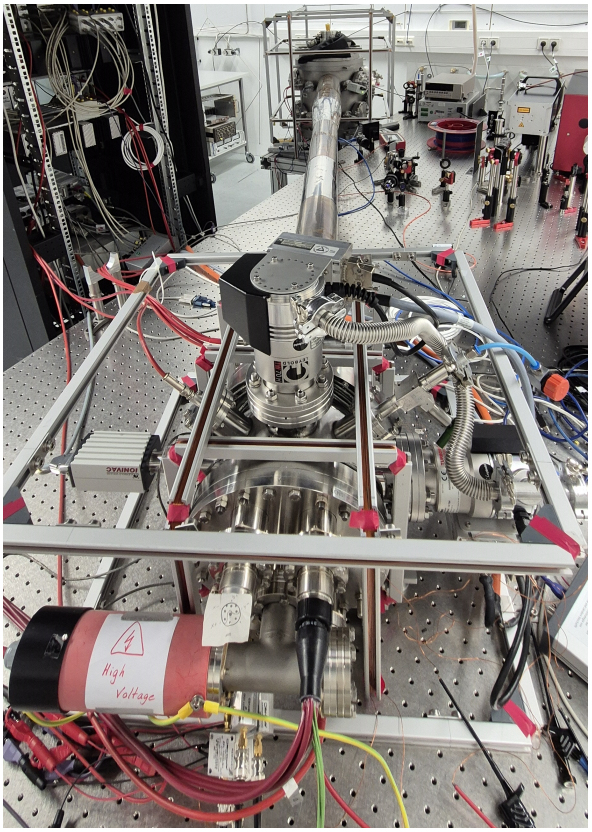

Figure 5.1: Adding the Mott detector to the setup for measuring the spin polarization of the scattered electrons form sodium atoms.

As mentioned earlier, since the experiment runs for around 40 hours, to ensure that we have consistent electron beam current and direction throughout the experiment, we installed a four-segment detector directly in front of the electron gun after the electric shield mesh. This detector, as shown in Fig. 5.2, has four separate segments that can measure the current reaching each part individually. By monitoring the current of each segment, we can track the center position of the beam and in cases when the beam position moves during the measurements, we can adjust it by changing the position of the UV light on the cathode to ensure that the experimental conditions are consistent during the measurement.

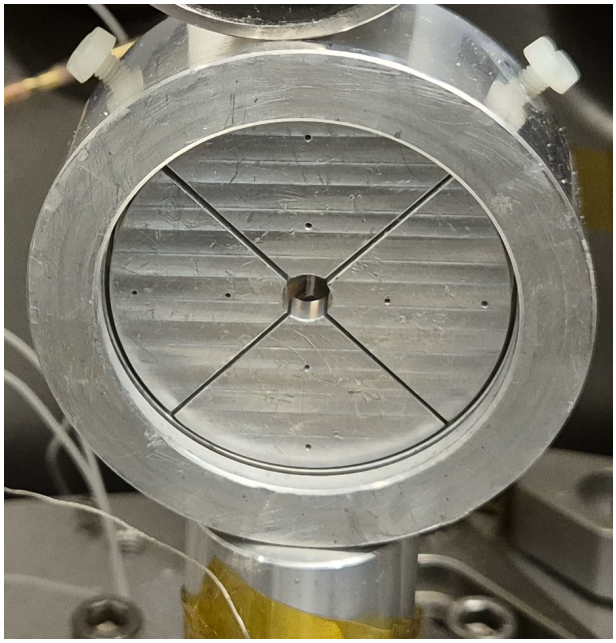

Figure 5.2: The four-segment detector four monitoring the center of the electron beam during the measurements.

Based on the theoretical considerations for photo-excitation of sodium atoms, it is important that the incoming yellow beam is perpendicular to the scattering path and as a result of this alignment, spin polarization of electrons is directed along the x-axis. However, in our experimental setup, the yellow light after passing the sodium atoms would hit the aperture plate placed in front of the electron gun, which is designed to filter out stray electrons. If the light scatters from the aperture plate, it could still photo-

excite the sodium atoms. Since this scattered light would be unpolarized and not aligned perpendicularly to the scattering path, it could have effect on the spin polarization of the detected electrons and compromising the accuracy of the measurements. To avoid this, we placed a small mirror near the aperture to deflect the yellow light away from the experimental region and into a beam dump. The schematic layout and an experimental photo of this configuration are shown in Fig. 5.3.

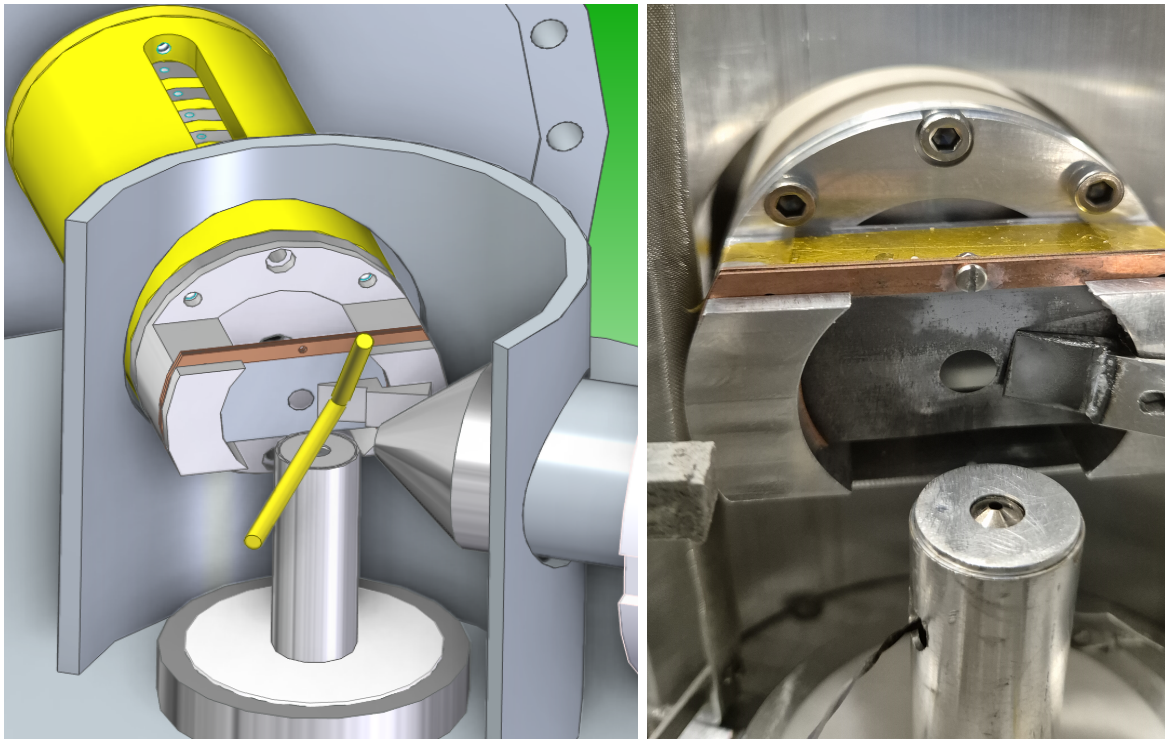

(a) (b)

Figure 5.3: a) Schematic layout, and b) experimental photo showing the use of a mirror to direct the light out of the interaction region.

After making all the necessary modifications and installing the Mott detector, the experimental setup was finally ready. The full setup inside the chamber is shown in Fig. 5.4. In this configuration, we installed two mirrors to guide the yellow light into the interaction region. Additionally, a beam dump was placed above the four-segment detector to absorb the reflected yellow light and prevent any unwanted scattering that could interfere with the experiment.

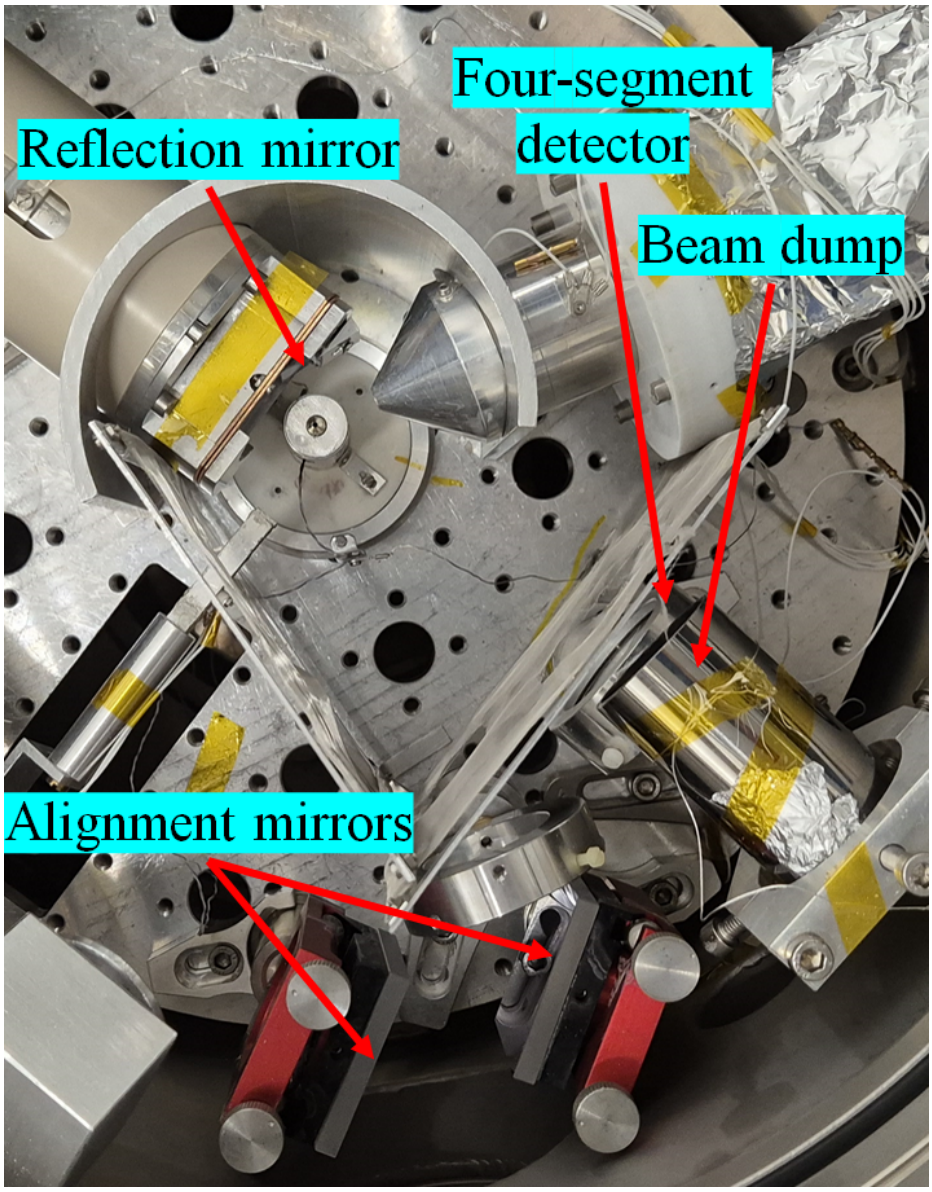

Figure 5.4: The final scattering setup for starting the experiment.

Our Mott detector can measure the spin polarization of electrons along both the x-axis and y-axis, which are perpendicular to the electron beam's path. It uses four MCPs: two positioned vertically to detect spin polarization along the x-axis, and two positioned horizontally to measure it along the y-axis. The measured asymmetry corresponding to spin polarization along the x-axis, detected by the vertical MCPs, is denoted as A_x, while the asymmetry for spin polarization along the y-axis, measured by the horizontal MCPs, is denoted as A_y. Based on our theoretical model, the spin polarization of electrons should

be aligned along the x-axis. This means we expect to see a nonzero asymmetry in the vertical detection plane ($A_x \neq 0$) and no asymmetry in the horizontal detection plane ($A_y = 0$).

To measure the asymmetry, as described by Eq. 2.31, we need to compare the number of electrons detected by each MCP for both right and left circularly polarized light. Since the total experimental run time is around 40 hours, instead of measuring for 20 hours with right circular polarization and another 20 hours with left circular polarization, we chose to change the polarization of the yellow beam every three minutes and afterward, we summed all the measurements for right circular polarization and did the same for left circular polarization. This helps to minimize the effects of gradual changes, like changes in the electron gun current or energy shifts caused by sodium deposition on the cathode over time. By switching polarization at shorter intervals, we can account for these small changes and keep the measurements accurate throughout the entire experiment. As mentioned, the quarter waveplate, placed after the delay fiber, is mounted on a motorized stage, and allow us to switch between right circular and left circular polarization by rotating the waveplate automatically.

Fig. 5.5 shows a sample measurement of the number of detected electrons for each MCP and compares the results for both right and left circular polarization of the yellow beam. The v+ and v- represent the measurements from the MCPs positioned vertically on the Mott detector, while the h+ and h- correspond to the MCPs positioned horizontally on the Mott detector.

As shown in this figure, we detected two temporally separated groups of electrons, which is consistent with previous measurements. The first group consists of scattered electrons from sodium atoms, while the second group refers to the secondary electrons. To measure the asymmetry, we need to focus on the electrons, which are scattered from sodium atoms. However, we must consider that the pulse width of the electron beam is around 80 ns, while the pulse width of the yellow light is only about 25 ns. As a result, not

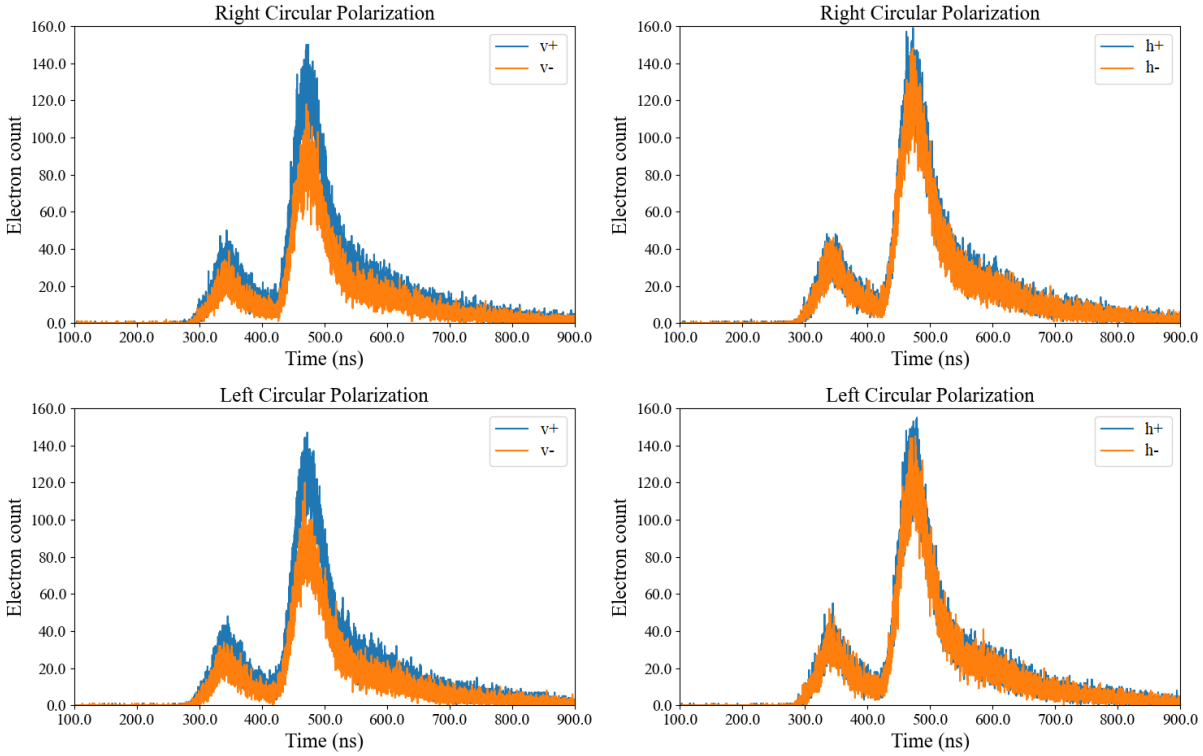

Figure 5.5: The total number of detected electrons at each time interval for both right and left circular polarization over the entire 40-hour measurement period.

all scattered electrons can be polarized, but only those electrons entangled with photo-excited sodium atoms. Also, the long electron pulse should not matter too much, because the shorter yellow pulse excites the atoms only after > 330 ns.

Since the delay line is approximately 330 ns, we focused our calculations to a small time window between 330 ns and 355 ns. In this way, we ensure that we are calculating the correct electrons. We expect to observe asymmetry exclusively within this region and we refer to this region as the photo-excitation region.

For the secondary electrons, which are not polarized, we expect no asymmetry in the measurements. But we can use this group as a reference to verify that the Mott detector is functioning correctly. We arbitrarily chose the time window between 440 ns and 520 ns for this check, but it is not critical and any region outside the photo-excitation region should yield zero asymmetry. We refer to this time window as the reference region for clarity. The selected time regions are highlighted in Fig. 5.6

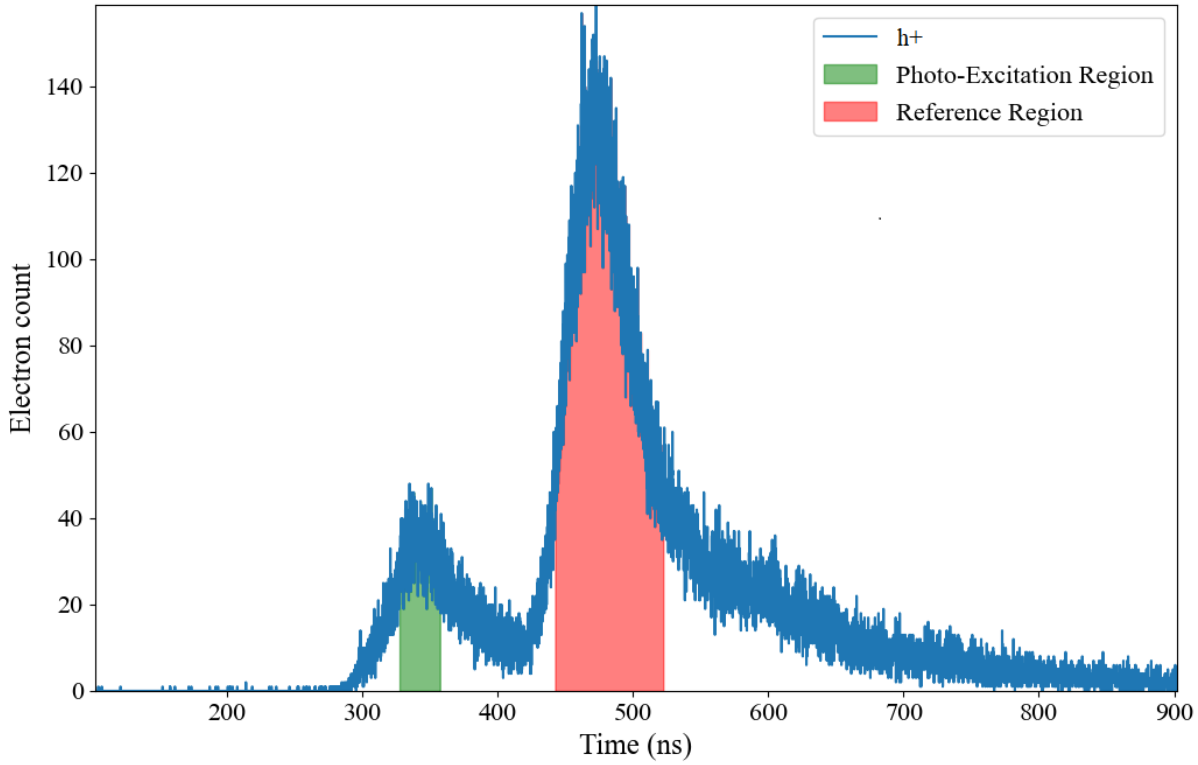

Figure 5.6: The total number of detected electrons at each time interval for the MCP located on the right side along the x-axis in 35 hours. The photo-excitation region and the reference region are indicated.

Finally, we summed the counted number of electrons for each MCP separately within the defined time intervals (photo-excitation and reference regions) and applied Eq. 2.31 to calculate the asymmetry separately for each region and we observed that after a continuous data acquisition period of 40 hours, the total calculated asymmetry along both the x- and y-axes was close to zero for both regions. But according to the theoretical considerations, since the Sherman function of our Mott detector is around $S = 0.17$ and maximum photo-excitation efficiency is 65% for sodium atoms and considering that not all electrons from the electron gun possess the optimal energy of 10 eV, we anticipated an asymmetry of approximately $A_x = 6 - 8\%$ along the x-axis under ideal conditions for photo-excitation region.

To investigate this discrepancy, we subdivided the data into 5-hour intervals and we observed differences between the asymmetry of electrons scattered from sodium atoms and

the reference electrons. The reference electron measurements demonstrated remarkable stability, maintaining consistently near-zero values throughout the entire measurement period. However, the asymmetry of the electrons scattered from sodium atoms exhibited dramatic fluctuations in the x-axis, ranging from approximately -10% to +10%.

Fig. 5.7 shows the evolution of both asymmetry components during the 40-hour measurement period. To validate these results and assess reproducibility, we repeated the experiment under identical conditions, and all of them exhibited similar fluctuations in A_x. A discussion on how the indicated error bars were derived through error propagation is provided in Appendix A.

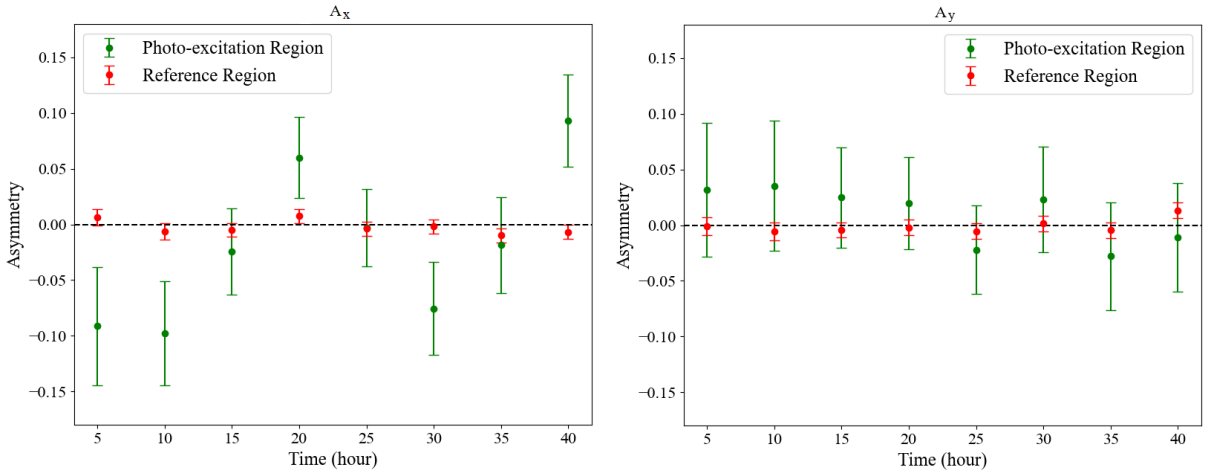

Figure 5.7: The measured asymmetry for electrons in the reference region (red) and the photo-excitation region (green) along the x- and y-axes over a 40-hour period. The oven temperature during these measurements was approximately 310 °C.

To determine whether the observed fluctuations were intrinsic to the experimental setup or specifically related to the spin of the detected electrons, we repeated the experiment without the yellow light, thereby preventing the excitation of sodium atoms. Under this condition, we expected the detected asymmetry to consistently remain at zero due to the absence of spin polarization. As anticipated, the observed asymmetry was zero, with fluctuations remaining within the error bars and much smaller than those observed during photo-excitation. Fig. 5.8 shows the measured asymmetry along both the x- and y-axes, showing that in the absence of sodium atom excitation, no asymmetry was detected.

This measurement strongly indicates that the previously observed fluctuations are indeed related to the spin polarization of the electrons, which results from the photo-excitation of sodium atoms. This excitation polarizes the electron beam, leading to some asymmetry in the vertical detectors. However, some unknown factor is affecting the experiment's consistency and introducing variations in the results, leading to a vanishing spin polarization after averaging over an extended period of time.

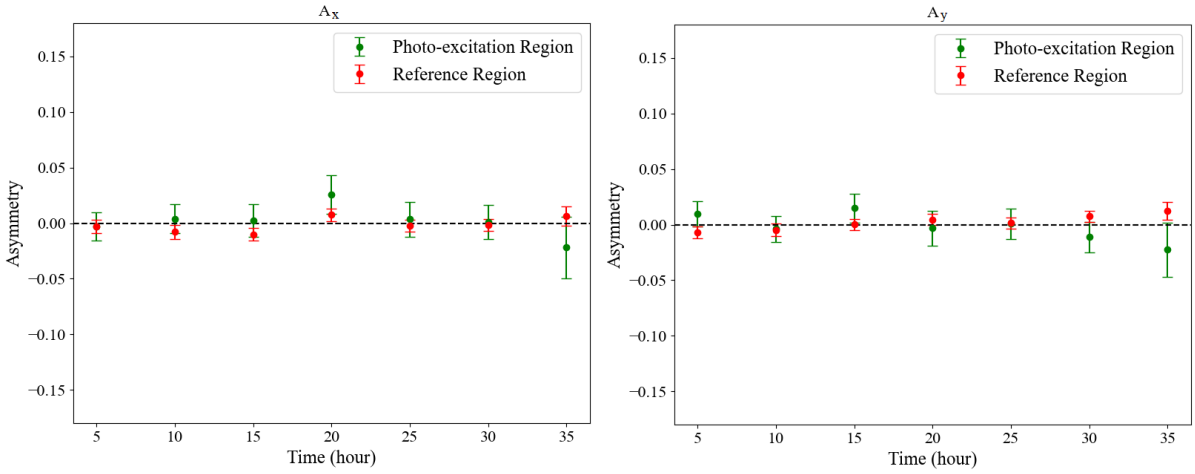

Figure 5.8: The measured asymmetry without the yellow light, preventing the excitation of sodium atoms. For this measurement, the electron gun current was slightly increased, and the oven temperature was raised to generate more scattered electrons and reduce measurement error.

The first idea regarding these fluctuations was that sodium deposition on the cathode surface might change the energy of the output electron beam and this deposition might change the energy distribution of the emitted electron beam, potentially affecting the efficiency of electron-sodium atom entanglement and consequently influencing the measured values, as discussed in Section 2.1.1. However, the observation of fluctuations ranging from negative to positive values does not fully support this idea, as such a mechanism would more likely result in magnitude changes rather than sign inversions. Nonetheless, we tested this by varying the electron beam energy between 10 and 12 eV, but no clear correlation between the fluctuations and beam energy was observed.

An alternative considered explanation is a potentially changing magnetic field within

the vacuum chamber. To investigate this possibility, we placed a magnetic field sensor close to (10 cm) the interaction region. This sensor monitored all components of the magnetic field throughout the measurement period. The measurements revealed remarkably stable conditions, with mean values of $B_x = 3.66\,\mu\text{T}$, $B_y = -0.45\,\mu\text{T}$, and $B_z = -0.86\,\mu\text{T}$. The stability of these fields was further confirmed by their small RMS deviations of 0.14 µT, 0.11 µT, and 0.05 µT for the x, y, and z components, respectively. Despite our thorough analysis, we found no correlation between these minor magnetic field fluctuations and the observed asymmetry variations, indicating that the magnetic field was not a contributing factor to the fluctuations.

In a further investigation, we examined whether the timing between electron generation and sodium atom excitation could be responsible for the observed fluctuations. We modified the experimental setup by reducing the optical path length for the yellow light. Specifically, we shortened the optical fiber by 2 m, which decreased the delay time by 10 ns. However, as shown in Fig. 5.9, the asymmetry fluctuations persisted with characteristics similar to our previous measurements, suggesting that a timing offset of this order was not the primary source of the observed instabilities.

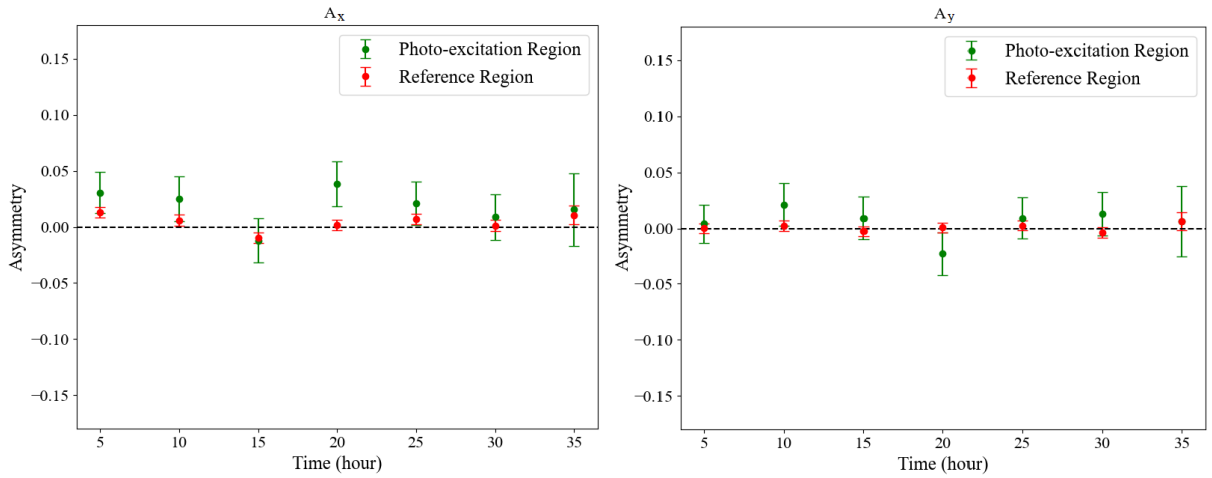

Figure 5.9: Measured asymmetry components as a function of time with modified optical delay. Results were obtained after reducing the optical fiber length by 2 m, corresponding to a 10 ns decrease in the delay time between electron generation and sodium atom photo-excitation.

To further confirm that the observed asymmetry fluctuations were caused by electron polarization due to photo-excitation of sodium atoms, we measured the asymmetry at different atomic transitions of sodium atoms. We tuned the yellow laser to the sodium D_2 absorption line instead of the D_1 line, where theoretical calculations predict only 50% of electrons will be polarized in this transition line [27]. If the observed asymmetry fluctuations indeed result from electron polarization, we expected to observe reduced fluctuation amplitudes compared to D_1 line transition. The experimental results, shown in Fig. 5.10, confirmed this, showing noticeably reduced fluctuations. This behavior was consistently observed in repeated experiments, suggesting that the asymmetry fluctuations are closely tied to the polarization of scattered electron beam.

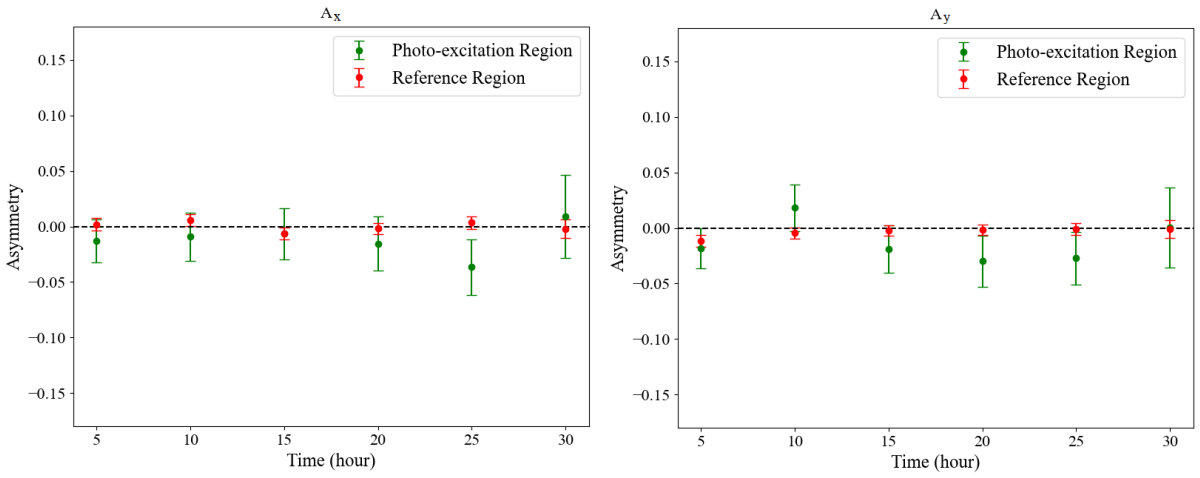

Figure 5.10: Measured asymmetry components as a function of time for photo-excitation of D_2 line of sodium atom.

Another possible explanation could be the incompleteness of the theoretical model. In the current theoretical calculations, the nuclear spin is not considered. Since the sodium has a nuclear spin of $I = 3/2$, nuclear spin can couple to the electron-atom system after the elastic scattering process. This coupling may disturb the previous electron-atom entanglement, potentially leading to a reduction in the transferred spin polarization.

Taking the nuclear spin coupling to the outer valence electron of the sodium atom as a perturbation, which is validated based on various experimental studies, particularly for

measuring the asymmetry of elastically scattered polarized electrons from alkali atoms, e.g. see the work by McClelland et al. [18] or Baum et al. [25]. As has been shown by Blum and Lohmann [6] electron-atom entanglement can be directly related to the asymmetry parameter. And, as has been shown by the asymmetry [18, 25] we are able to consider the coupling of the nuclear spin as a distortion. Hence, we are able to adapt methods of angular momentum perturbation theory discussed in detail in the book by Blum [9].

With the spin of the ground state Na atom, we have $J = 1/2$ and, hence, the vector coupling $\mathbf{J} + \mathbf{I} = \mathbf{F}$ occurs. From the nuclear-atom angular momentum coupling rules, we obtain for the total angular momentum, $1 \leq F \leq 2$. Taking the perturbation coefficients of Blum [9], and inserting $J = 1/2$ and $I = 3/2$, we obtain

$$G(J = \frac{1}{2}; t)_K = \frac{1}{4} \sum_{FF'} (2F+1)(2F'+1) \times \begin{Bmatrix} \frac{1}{2} & F' & \frac{3}{2} \\ F & \frac{1}{2} & K \end{Bmatrix}^2 \cos\left[\frac{(E_{F'} - E_F)t}{\hbar}\right]. \tag{5.1}$$

It is convenient to represent the coefficients $G(J = 1/2; t)_K$ in the form

$$\begin{aligned} G(J = \frac{1}{2}; t)_K = \overline{G(J = \frac{1}{2})_K} + \frac{1}{4} \sum_{F \neq F'} (2F+1)(2F'+1) \\ \times \begin{Bmatrix} \frac{1}{2} & F' & \frac{3}{2} \\ F & \frac{1}{2} & K \end{Bmatrix}^2 \cos\left[\frac{(E_{F'} - E_F)t}{\hbar}\right], \end{aligned} \tag{5.2}$$

where the terms with $J = J'$ and terms with $J \neq J'$ have been separated. Thus, the time-independent coefficient is defined by

$$\overline{G(J = 1/2)_K} = \frac{1}{4} \sum_{F} (2F+1)^2 \times \begin{Bmatrix} \frac{1}{2} & F & \frac{3}{2} \\ F & \frac{1}{2} & K \end{Bmatrix}^2 . \tag{5.3}$$

As we are investigating spin effects of the scattered electrons, the rank K of the perturbation coefficients must be restricted to $K = 1$, only. Inserting the relevant quantum

numbers in Eq. 5.3, we obtain

$$\overline{G(J=1/2)_1} = \frac{3}{8}\,, \tag{5.4}$$

for the constant part and, with the time-dependent part, we get from Eq. 5.2

$$G(J=1/2;t)_1 = \frac{1}{8}\left\{3+\frac{5}{2}\cos\left[\frac{(E_2-E_1)t}{\hbar}\right]\right\}. \tag{5.5}$$

Thus, we find the spin polarization perturbation coefficient as always positive and, as the cosine is restricted to the interval $[-1,1]$, we are able to get upper and lower bounds of the G_1 parameter as

$$\frac{1}{16} \leq G(J=1/2;t)_1 \leq \frac{11}{16}\,. \tag{5.6}$$

This results in the fact that the perturbation always remains as a positive quantity, irrespective of its oscillations in time. Thus, any perturbation effect whatsoever is not able to explain a change of sign, even in the slightest way, in the degree of the measured spin polarization.

On the other hand, as the experimental results seems to show a slight variation between positive and negative values around zero, such perturbation effect, due to the coupling of the nuclear spin, may cause a general reduction of the electronic spin polarization, however, it does not explain a change of sign of the measured spin polarization.

5.2 Discussions and Future Works

Our investigations suggest the potential of subsequently polarizing electrons via non-local quantum (teleportation) effects, although the observed instabilities prevent definitive confirmation. By comparing the photo-excitation of sodium atoms at the D_1 and D_2 transition lines and tests without any photo-excitation, we can conclude that electron polarization through quantum teleportation is achievable. The results particularly indicate that the asymmetry fluctuations observed for both D_1 and D_2 transitions are linked to

the non-zero spin polarization of electrons. However, despite thorough examination of various potential sources of instability—such as variations in electron energy, magnetic field effects, and adjustments in the timing of sodium atom photo-excitation—the precise cause of the fluctuations remains undetermined.

Unfortunately, due to time constraints, we were unable to conduct additional investigations to identify the precise source of these fluctuations. Nevertheless, our analysis has identified several critical areas for future investigation:

1. **Monitoring the stability of laser wavelength**: One potential source of the observed fluctuations could be instability in the yellow laser's wavelength during the measurements. The challenge in investigating this idea lies in the laser's spectral width of approximately 2 GHz, which exceeds the resolution of conventional spectrometers. Therefore, implementing high-precision wavelength monitoring systems capable of resolving sub-GHz frequency shifts over extended measurement periods would be essential for future investigations of this effect.

2. **Reducing measurement time**: The extended 40-hour measurement period makes the experiment vulnerable to environmental fluctuations that may not be immediately apparent. To improve experimental reliability, we need to reduce the measurement duration by increasing the number of scattered electrons. This can be achieved either by raising the density of sodium atoms in the interaction region or by generating more electrons.

   One approach to increasing the sodium atom density is using an oven equipped with multichannel collimators instead of a single tube, which would enhance the atomic beam density. However, this method is more complex and costly in terms of fabrication. Alternatively, to increase the number of generated electrons, we could increase the number of electrons per pulse. However, as previously discussed, this requires careful attention to space charge effects, which can change the energy and

trajectory of the electron beam. A more practical solution would be to increase the laser repetition rate, potentially up to 200 kHz.

Since our complete measurement cycle – from electron generation to detection at the Mott detector – requires less than 1 μs, this higher repetition rate is technically feasible. The main technical consideration is thermal management of the sodium oven, particularly since the current of its heating coils must be zero during measurements to avoid generating magnetic fields. By operating the laser at 200 kHz, we can implement a precise timing sequence where the heating coils are switched off for just 1 μs before and after each pulse, while the coils are on during the intermediate 3 μs period. This optimization would reduce our total measurement time from 40 hours to approximately 2 hours, which would be a game-changer for avoiding all those environmental factors that can happen during long time measurement.

3. **Monitoring the energy of the electron beam**: During the measurements, sodium atom deposition on the cathode surface can potentially change the electron beam energy and reduce the reliability of the data. To avoid it, we suggest to implement a real-time system to monitor the electron beam energy and adjust the cathode voltage as needed. This feedback mechanism would ensure that the beam energy stays consistent by automatically compensating for any changes caused by the sodium deposition on the surface of the cathode. This approach would not only improve the accuracy of our measurements but also provide useful insights into the cathode's condition throughout the experiment.

4. **Optimization of the electron gun design**: As mentioned before, the current electron gun configuration is sensitive to the UV beam position on the cathode, which can change the trajectory of generated electron beam specially during extended measurement periods. Therefore, it is necessary to modify the electron gun design

to reduce its sensitivity to UV beam positioning variations which would enhance the system's robustness against minor mechanical and thermal variations and ultimately improve experimental reproducibility and reliability.

5. **Reducing pulse duration of the laser**: For the performed measurements, the electron beam had a pulse duration of approximately 80 ns, while the yellow light used for photo-excitation had a pulse duration of around 25 ns. This mismatch prevents the full polarization of the entire electron beam by the sodium atoms during photo-excitation. To solve this, we can either increase the pulse duration of the yellow light or reduce the pulse duration of the electron beam, which is determined by the pulse duration of the UV light.

   Reducing the UV pulse duration would be the better approach for several reasons. With fewer electrons generated in a shorter pulse, we can minimize space charge effects, which can change the energy and the trajectory of the electron beam. Additionally, reducing the detection range also reduces background noise and unwanted electron detection and improves the accuracy of the measurements. In this way, we can be sure that the entire electron beam is polarized and this method not only improves the precision of the experiment but also reduces potential sources of error, leading to more reliable results.

As mentioned before, due to time constraints, we were unable to implement these modifications or conduct additional measurements to fully understand the source of the observed fluctuations. However, the proposed adjustments present promising opportunities for enhancing measurement stability and reliability in future experiments. While our current results demonstrate the feasibility of electron polarization through non-local quantum (teleportation) effects, but further experimental work is necessary to achieve the stability and reliability required for practical applications. The insights gained from this investigation provide a clear roadmap for future improvements that could establish this

technique as a viable method for demonstrating the possibility of quantum teleportation for fermions.

In this research, I measured and investigated the transfer of circular photon polarization into electron spin polarization via non-local quantum (teleportation) effects for the first time. After providing background on the field in chapter 2, I briefly review the underlying theory, while the experimental design and simulations are discussed in chapter 3. In chapter 4, I give a detailed description of the experimental set-up, and its various new developed technical elements, necessary for experimental analysis. In chapter 5, the experimental results are presented and a thorough discussion of the obtained data is given.

Possible tasks for future research are outlined and various suggestions for improvements are made, finalized by a short conclusion. It is hoped that, although the effect is small, the non-zero photon-to-electron polarization transfer results caused by non-local quantum effects will stimulate and initiate further research in the field of non-local interactions between bosonic and fermionic systems.

Bibliography

[1] A. Einstein, B. Podolsky, and N. Rosen. Can quantum-mechanical description of physical reality be considered complete? *Phys. Rev.*, 47:777–780, May 1935. doi: 10.1103/PhysRev.47.777. URL https://link.aps.org/doi/10.1103/PhysRev.47.777.

[2] Alain Aspect, Philippe Grangier, and Gérard Roger. Experimental tests of realistic local theories via bell's theorem. *Phys. Rev. Lett.*, 47:460–463, Aug 1981. doi: 10.1103/PhysRevLett.47.460. URL https://link.aps.org/doi/10.1103/PhysRevLett.47.460.

[3] Alain Aspect, Jean Dalibard, and Gérard Roger. Experimental test of bell's inequalities using time-varying analyzers. *Phys. Rev. Lett.*, 49:1804–1807, Dec 1982. doi: 10.1103/PhysRevLett.49.1804. URL https://link.aps.org/doi/10.1103/PhysRevLett.49.1804.

[4] Anton Zeilinger. Quantum teleportation, onwards and upwards. *Nature Physics*, 14: 3–4, Jan 2018. doi: 10.1038/nphys4339. URL https://www.nature.com/articles/nphys4339.

[5] Juan Yin and et al. Satellite-based entanglement distribution over 1200 kilometers. *Science*, 365:1140–1144, Jun 2017. doi: 10.1126/science.aan3211. URL https://www.science.org/doi/10.1126/science.aan3211.

[6] K. Blum and B. Lohmann. Entanglement and bell correlation in electron-exchange collisions. *Phys. Rev. Lett.*, 116:033201, Jan 2016. doi: 10.1103/PhysRevLett.116.033201. URL https://link.aps.org/doi/10.1103/PhysRevLett.116.033201.

[7] B. Lohmann, K. Blum, and B. Langer. Tunable entanglement resource in elastic electron-exchange collisions out of chaotic spin systems. *PHYSICAL REVIEW A*, 94:032331, Sep 2016. doi: 10.1103/PhysRevA.94.032331. URL https://link.aps.org/doi/10.1103/PhysRevA.94.032331.

[8] B. Lohmann and K. Blum. Pauli-based fermionic teleportation with free massive particles by electron-exchange collisions. *New J. Phys.*, 21:033025, March 2019. doi: 10.1088/1367-2630/ab045b. URL https://iopscience.iop.org/article/10.1088/1367-2630/ab045b#back-to-top-target.

[9] Karl Blum. *Density Matrix Theory and Applications*. Springer Berlin, Heidelberg, https://link.springer.com/book/10.1007/978-3-642-20561-3, third edition edition, 2012.

[10] Asher Peres. Separability criterion for density matrices. *Phys. Rev. Lett.*, 77:1413–1415, Aug 1996. doi: 10.1103/PhysRevLett.77.1413. URL https://link.aps.org/doi/10.1103/PhysRevLett.77.1413.

[11] Michał Horodecki, Paweł Horodecki, and Ryszard Horodecki. Separability of mixed states: necessary and sufficient conditions. *Physics Letters A*, 223(1):1–8, 1996. ISSN 0375-9601. doi: https://doi.org/10.1016/S0375-9601(96)00706-2. URL https://www.sciencedirect.com/science/article/pii/S0375960196007062.

[12] S. R. Lorentz, R. E. Scholten, J. J. McClelland, M. H. Kelley, and R. J. Celotta. Spin-resolved elastic scattering of electrons from sodium below the inelastic threshold. *Phys. Rev. Lett.*, 67:3761–3763, Dec 1991. doi: 10.1103/PhysRevLett.67.3761. URL https://link.aps.org/doi/10.1103/PhysRevLett.67.3761.

[13] G. D. Fletcher, M. J. Alguard, T. J. Gay, V. W. Hughes, C. W. Tu, P. F. Wainwright, M. S. Lubell, W. Raith, and F. C. Tang. Measurement of spin-exchange effects in electron-hydrogen collisions: 90° elastic scattering from 4 to 30 ev. *Phys. Rev. Lett.*, 48:1671–1674, Jun 1982. doi: 10.1103/PhysRevLett.48.1671. URL https://link.aps.org/doi/10.1103/PhysRevLett.48.1671.

[14] G. D. Fletcher, M. J. Alguard, T. J. Gay, V. W. Hughes, P. F. Wainwright, M. S. Lubell, and W. Raith. Experimental study of spin-exchange effects in elastic and ionizing collisions of polarized electrons with polarized hydrogen atoms. *Phys. Rev. A*, 31:2854–2884, May 1985. doi: 10.1103/PhysRevA.31.2854. URL https://link.aps.org/doi/10.1103/PhysRevA.31.2854.

[15] Dipak H. Oza and Joseph Callaway. Spin asymmetry in elastic scattering of electrons by hydrogen atoms. *Phys. Rev. A*, 32:2534–2536, Oct 1985. doi: 10.1103/PhysRevA.32.2534. URL https://link.aps.org/doi/10.1103/PhysRevA.32.2534.

[16] W L van Wyngaarden and H R J Walters. Elastic scattering and excitation of the 1s to 2s and 1s2p transitions in atomic hydrogen by electrons to medium to high energies. *Journal of Physics B: Atomic and Molecular Physics*, 19:929, Oct 1986. doi: 10.1088/0022-3700/19/6/014. URL https://iopscience.iop.org/article/10.1088/0022-3700/19/6/014.

[17] Ian E. McCarthy and Bo Shang. Spin asymmetry in resonant electron-hydrogen elastic scattering. *Phys. Rev. A*, 48:1699–1700, Aug 1993. doi: 10.1103/PhysRevA.48.1699. URL https://link.aps.org/doi/10.1103/PhysRevA.48.1699.

[18] J. J. McClelland, M. H. Kelley, and R. J. Celotta. Superelastic scattering of spin-polarized electrons from sodium. *Phys. Rev. A*, 40:2321–2329, Sep 1989. doi: 10.1103/PhysRevA.40.2321. URL https://link.aps.org/doi/10.1103/PhysRevA.40.2321.

[19] R E Scholten, S R Lorentz, J J McClelland, M H Kelley, and R J Celotta. Spin-resolved scattering from sodium at 10 and 40 ev. *Journal of Physics B: Atomic, Molecular and Optical Physics*, 24(24):L653, dec 1991. doi: 10.1088/0953-4075/24/24/003. URL https://dx.doi.org/10.1088/0953-4075/24/24/003.

[20] J. J. McClelland, S. R. Lorentz, R. E. Scholten, M. H. Kelley, and R. J. Celotta. Determination of complex scattering amplitudes in low-energy elastic electron-sodium scattering. *Phys. Rev. A*, 46:6079–6082, Nov 1992. doi: 10.1103/PhysRevA.46.6079. URL https://link.aps.org/doi/10.1103/PhysRevA.46.6079.

[21] P.J.O. Teubner and E. Weigold. *Correlations and Polarization in Electronic and Atomic Collisions and (e,2e) Reactions, Satellite Meeting of the XVII ICPEAC*. Conference series. Taylor & Francis, 1992. ISBN 9780854984121. URL https://books.google.de/books?id=_875zgEACAAJ.

[22] D L Moores and D W Norcross. The scattering of electrons by sodium atoms. *Journal of Physics B: Atomic and Molecular Physics*, 5(8):1482, aug 1972. doi: 10.1088/0022-3700/5/8/015. URL https://dx.doi.org/10.1088/0022-3700/5/8/015.

[23] Igor Bray. Convergent close-coupling calculation of electron-sodium scattering. *Phys. Rev. A*, 49:R1–R4, Jan 1994. doi: 10.1103/PhysRevA.49.R1. URL https://link.aps.org/doi/10.1103/PhysRevA.49.R1.

[24] Igor Bray. Convergent close-coupling method for the calculation of electron scattering on hydrogenlike targets. *Phys. Rev. A*, 49:1066–1082, Feb 1994. doi: 10.1103/PhysRevA.49.1066. URL https://link.aps.org/doi/10.1103/PhysRevA.49.1066.

[25] G. Baum, M. Moede, W. Raith, and U. Sillmen. Measurement of spin dependence in low-energy elastic scattering of electrons from lithium atoms. *Phys. Rev. Lett.*, 57:

1855–1858, Oct 1986. doi: 10.1103/PhysRevLett.57.1855. URL https://link.aps.org/doi/10.1103/PhysRevLett.57.1855.

[26] Igor Bray, Dmitry V. Fursa, and Ian E. McCarthy. Calculation of electron-lithium scattering using the coupled-channel optical method. *Phys. Rev. A*, 47:1101–1110, Feb 1993. doi: 10.1103/PhysRevA.47.1101. URL https://link.aps.org/doi/10.1103/PhysRevA.47.1101.

[27] B. Lohmann, A. Azima, B. Langer, K. Bartschat, K. Blum, and M. Dreschere. Time-governed non-local photon-to-electron signalling via electron-exchange collisions. Technical report, Universität Hamburg, 2018. Draft version, unpublished.

[28] Joachim Kessler. *Polarized Electrons*. Springer-Verlag Berlin Heidelberg GmbH, https://link.springer.com/book/10.1007/978-3-662-02434-8, second edition edition, 1985.

[29] Nevill Francis Mott. The scattering of fast electrons by atomic nuclei. *Proc. R. Soc A*, 124:425–442, Feb 1929. doi: 10.1098/rspa.1929.0127. URL https://royalsocietypublishing.org/doi/10.1098/rspa.1929.0127.

[30] T. J. Gay and F. B. Dunning. Mott electron polarimetry. *Rev. Sci. Instrum*, 63:1635, Jan 1992. doi: 10.1063/1.1143371. URL https://pubs.aip.org/aip/rsi/article/63/2/1635/328628/Mott-electron-polarimetry.

[31] Vitali Mildenberger. Inbetriebnahme und charakterisierung einer mott-detektoreinheit zur messung der elektronen-spinpolarisation. mathesis, University of Hamburg, 2019.

[32] C.B. Lucas. *Atomic and Molecular Beams: Production and Collimation*. CRC Press, https://books.google.de/books?id=e1PSBQAAQBAJ, 1st edition edition, 2013.

[33] Giacinto Scoles. *Atomic and Molecular Beam Methods*. Oxford University Press, 1st edition edition, 1988.

[34] Daniel A. Steck. Sodium d line data. https://steck.us/alkalidata/, September 2023.

[35] T. Srinivasan-Rao, J. Fischer, and T. Tsang. Photoemission studies on metals using picosecond ultraviolet laser pulses. *J. Appl. Phys.*, 69:3291–3296, March 1991. doi: 10.1063/1.348550. URL https://pubs.aip.org/aip/jap/article/

69/5/3291/20639/Photoemission-studies-on-metals-using-picosecond?pdfCoverIconEvent=cite.

[36] A Janzen, B Krenzer, O Heinz, P Zhou, D Thien, A Hanisch, F-J Meyer Zu Heringdorf, D von der Linde, and M Horn von Hoegen. A pulsed electron gun for ultrafast electron diffraction at surfaces. *The Review of scientific instruments*, 78: 013906, Jan 2007. doi: 10.1063/1.2431088. URL https://pubmed.ncbi.nlm.nih.gov/17503932/.

[37] Andras Kolenbrander. Development and characterization of a pulsed e-gun for slow electrons. diplomathesis, University of Hamburg, 2019.

[38] Marc-Christopher Muckelberg. Design and setup of a beamline for the long-range transport of spin-polarized electrons. mathesis, University of Hamburg, 2020.

[39] Earl D. Babcock. Spin-exchange optical pumping with alkali-metal vapors. phdthesis, University of Wisconsin–Madison, 2005.

[40] U. Volz, M. Majerus, H. Liebel, A. Schmitt, and H. Schmoranzer. Precision lifetime measurements on NaI$3p^2P_{1/2}$ and $3p^2p_{3/2}$ by beam-gas-laser spectroscopy. *Phys. Rev. Lett.*, 76:2862–2865, Apr 1996. doi: 10.1103/PhysRevLett.76.2862. URL https://link.aps.org/doi/10.1103/PhysRevLett.76.2862.

[41] Robert C. Hilborn. Einstein coefficients, cross sections, f values, dipole moments, and all that. *arXiv:physics*, Feb 202. doi: 10.48550/arXiv.physics/0202029. URL https://arxiv.org/abs/physics/0202029v1.

[42] Martin Misakian. Equations for the magnetic field produced by one or more rectangular loops of wire in the same plane. *J Res Natl Inst Stand Technol*, 105: 557–64, Jul-Aug 2000. doi: 10.6028/jres.105.045. URL https://www.ncbi.nlm.nih.gov/pmc/articles/PMC4877158/.

[43] Andras Kolenbrander. Commissioning of an electrostatic lens system for the transport of slow electrons over long distances. mathesis, University of Hamburg, 2022.

Appendix A
Error Calculation

In this appendix, we present a detailed analysis of the uncertainties in our experimental measurements for the calculated asymmetry. Since our final results depend on electron count rates in different detection channels, careful consideration of error propagation is essential for accurate uncertainty estimation.

To simplify notation, we define the following substitutions: $U_\uparrow = a$, $U_\downarrow = b$, $D_\uparrow = c$, and $D_\downarrow = d$. Using these substitutions, the asymmetry f is expressed as

$$f = \frac{\sqrt{ad} - \sqrt{bc}}{\sqrt{ad} + \sqrt{bc}}. \tag{A.1}$$

The uncertainty in function f, denoted as σ_f, can be determined through error propagation analysis. For a function of multiple independent variables, the propagation of uncertainty is given by

$$\sigma_f = \sqrt{\left(\frac{\partial f}{\partial a}\sigma_a\right)^2 + \left(\frac{\partial f}{\partial b}\sigma_b\right)^2 + \left(\frac{\partial f}{\partial c}\sigma_c\right)^2 + \left(\frac{\partial f}{\partial d}\sigma_d\right)^2}, \tag{A.2}$$

where σ_a, σ_b, σ_c, and σ_d represent the standard deviations of the respective variables and $\frac{\partial f}{\partial x}$ is the partial derivative of f with respect to x.

By calculating the partial derivatives of f with respect to a, b, c, and d we can show

$$\begin{aligned} \frac{\partial f}{\partial a} &= \frac{\sqrt{abcd}}{a\left(\sqrt{ad} + \sqrt{bc}\right)^2}, & \frac{\partial f}{\partial b} &= -\frac{\sqrt{abcd}}{b\left(\sqrt{ad} + \sqrt{bc}\right)^2}, \\ \frac{\partial f}{\partial c} &= -\frac{\sqrt{abcd}}{c\left(\sqrt{ad} + \sqrt{bc}\right)^2}, & \frac{\partial f}{\partial d} &= \frac{\sqrt{abcd}}{d\left(\sqrt{ad} + \sqrt{bc}\right)^2}. \end{aligned} \tag{A.3}$$

Additionally, since a, b, c, and d correspond to electron counts, their uncertainties follow Poisson statistics, where the standard deviation is equal to the square root of the count

$$\sigma_x = \sqrt{x} \qquad for \quad x = a,\, b,\, c,\, d. \tag{A.4}$$

By substituting the expressions for the partial derivatives and the uncertainties into the

error propagation formula, we can determine the overall uncertainty in f, which is

$$\sigma_f = \frac{\sqrt{abcd}}{\left(\sqrt{ad}+\sqrt{bc}\right)^2}\sqrt{\frac{1}{a}+\frac{1}{b}+\frac{1}{c}+\frac{1}{d}}. \tag{A.5}$$

This methodology ensures a precise estimation of measurement errors, which is crucial for the reliability of the experimental results.

Acknowledgments

I would like to express my heartfelt appreciation to everyone who has been a part of my academic journey and has contributed to the completion of this dissertation. Your support and assistance have been invaluable.

First and foremost, I am deeply grateful to Prof. Dr. Markus Drescher, who gave me the opportunity to work on this topic and for his guidance throughout my doctoral work and Dr. Phillipp Wessel-Staarmann, my second supervisor, who was always open to providing assistance and guidance during the course of this research.

Also, I would like to express my deepest gratitude to Dr. Bernd Lohmann for his invaluable support and guidance on the theoretical aspects of my research. His insights and expertise played a crucial role in shaping the foundation of this work. I am also grateful to Dr. Armin Azima for his contributions to the theoretical framework that laid the groundwork for my experiment.

I would also like to extend my sincere thanks to Dr. Marek Wieland, whose invaluable contributions, discussions, and insights greatly enhanced the quality of this work. My sincere gratitude also goes to Dr. Mark Prandolini for his support in the lab and editing this dissertation—his guidance and technical assistance were instrumental in this project.

I extend my gratitude to Mr. Oliver Becker for fabrication of numerous essential components for this project. His dedication to providing assistance and his exceptional technical proficiency were indispensable to this project.

I would also like to extend my thanks to Andras Kouhenberg, a dedicated master's student, who played a pivotal role in the electron transfer system, making significant contributions to our research.

I would also like to acknowledge the support and understanding of my family and friends specially my wife throughout this academic journey. Your encouragement and patience have been a constant source of motivation.

This dissertation would not have been possible without the collective effort and encouragement of all those mentioned above and many others who have supported me along the way. Thank you all for being a part of this incredible journey.

Declaration

I hereby declare and affirm that this doctoral dissertation is my own work and that I have not used any aids and sources other than those indicated.

If electronic resources based on generative artificial intelligence (gAI) were used in the course of writing this dissertation, I confirm that my own work was the main and value-adding contribution and that complete documentation of all resources used is available in accordance with good scientific practice. I am responsible for any erroneous or distorted content, incorrect references, violations of data protection and copyright law or plagiarism that may have been generated by the gAI.

Date: September 25, 2025 Signature: M.kheyrollahi